

STEREOTAXIC 1000 MeV PROTON THERAPY AT THE PNPI SYNCHROCYCLOTRON

N.K. Abrossimov, Yu.A. Gavrikov, V.Ya. Gersenstein¹, E.M. Ivanov, N.N. Jalinitch¹, D.L. Karlin¹, V.I. Lasarev, V.V. Lysenko, Yu.A. Malov, T.V. Pushkareva¹, G.A. Riabov, D.M. Seliverstov, R.A. Shalek¹, V.M. Vinogradov¹, A.A. Vorobyev, O.M. Zhidkova¹, M.V. Zhidkov¹

¹Russian Scientific Center of Radiology and Surgical Technology – RSCRST

1. Introduction

At present the hadron (proton and light ions like ¹²C) therapy is used successfully for the treatment different types of oncological tumors. Since the beginning of radiological bloodless surgery in 1961 till today more than 50000 patients were treated at 40 medical centers over the world. Figure 1 illustrates the progress in putting into operation medical centers with a number of treated patients more than 1000. On histogram the start year of center's operation is given. The PNPI-RSCRST medical complex as one of the first proton facilities has a long-term experience in the radiotherapy of brain diseases. All acting irradiation centers use in the irradiation treatment so called method of "Bragg peak" required proton energy of 200–250 MeV. PNPI uses in stereotaxic therapy protons with $E_p = 1000$ MeV, that is the unique method over the world. The advantage of the high energy proton beam is a low scattering of protons in the tissue.

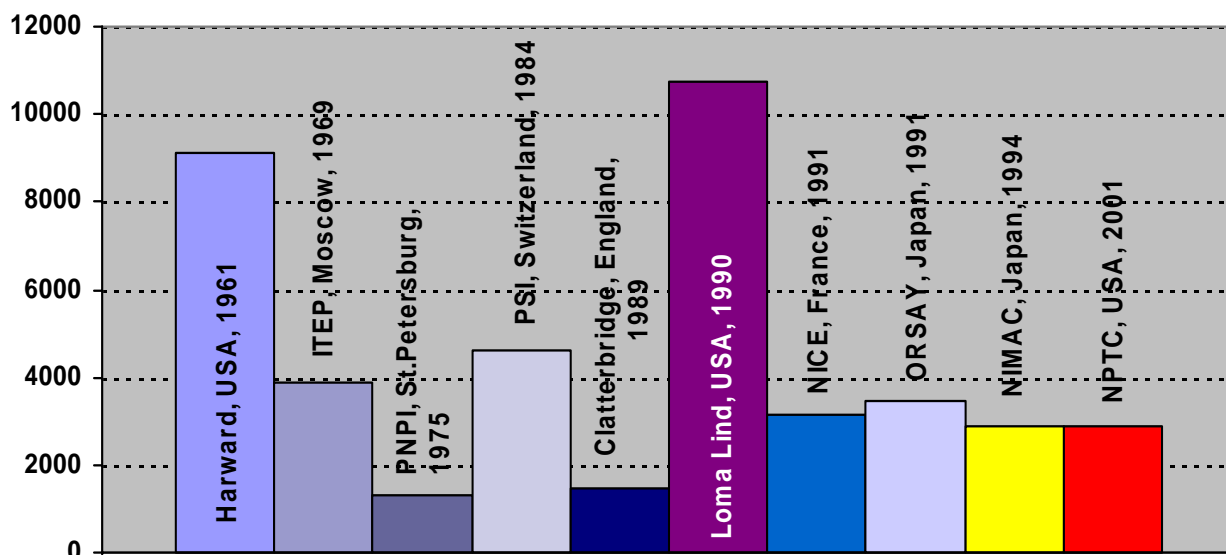


Fig. 1. Medical centers over the world with a number of patients more than 1000 treated by hadron therapy

Protons of this energy easily penetrate through an irradiated object producing a uniform ionization along their tracks. Due to low scattering of protons in the tissue, a narrow beam with sharp edges can be shaped at the entrance of the irradiated zone inside the object. Such irradiation method combined with two ways rotation technique allows to provide a very high ratio of the dose in the irradiated zone to the dose at the object's surface. Dose fields with high edge gradient obtained by such method are especially important in the cases when the irradiation is used for selective damage of the volumes placed in immediate proximity to the life-critical organs. Our method gives the most effective results at proton treatment of pituitary adenomas and arterio-venous malformations as well as the hormone-dependent forms of mammary gland and prostate cancer, *etc.* Detailed publication of PNPI method of proton therapy and obtained results during 1975–1996 are given in Refs. [1, 2]. In this paper we present the results of 1000 MeV proton stereotaxic therapy different head brain diseases performed during 2002–2006 and the description of a medical beam upgrade which has been done in 2003–2004.

2. Technical features of proton therapy facility

The PNPI proton therapy facility is based on the synchrocyclotron with fixed energy of proton beam ($E_p = 1000$ MeV), which was built for the purpose of research on the nuclear and particle physics at intermediate energies. Artistic view of synchrocyclotron is shown in Fig. 2. The current inside the vacuum chamber of the accelerator is $3 \mu\text{A}$. The intensity of the extracted beam in the accelerator hall is $1 \mu\text{A}$. The accelerator has three beam lines for the transportation of proton beams into the experimental hall with fixed energy of 1000 MeV with regulated intensities in the range 10^7 – 10^{11} proton/sec.

Extracted from the accelerator medical proton beam (Fig. 2) is produced by beam shaping collimator placed just at the entrance of the beam channel. It regulates the size of beam spot and consequently the intensity of the beam. Then the beam is deflected by bending magnet and focused by quadrupole lenses onto the irradiation hall (Fig. 3). The total length of the beam line is 70 m. The antihalo collimator is installed in the experimental hall. Such simple beam optics scheme allows to obtain in the irradiation zone a narrow beam of 6 mm in diameter with sharp edges. The beam is transported in a vacuum pipe to prevent the multiple scattering and inelastic interactions of protons in the air. The irradiation hall is separated from the experimental hall by two shielding walls made from iron and concrete provided the radiation background in the hall at quite low level. The beam position in the accelerator and experimental halls as well as in the irradiation hall and the beam intensity are under a permanent control from the accelerator and medical control

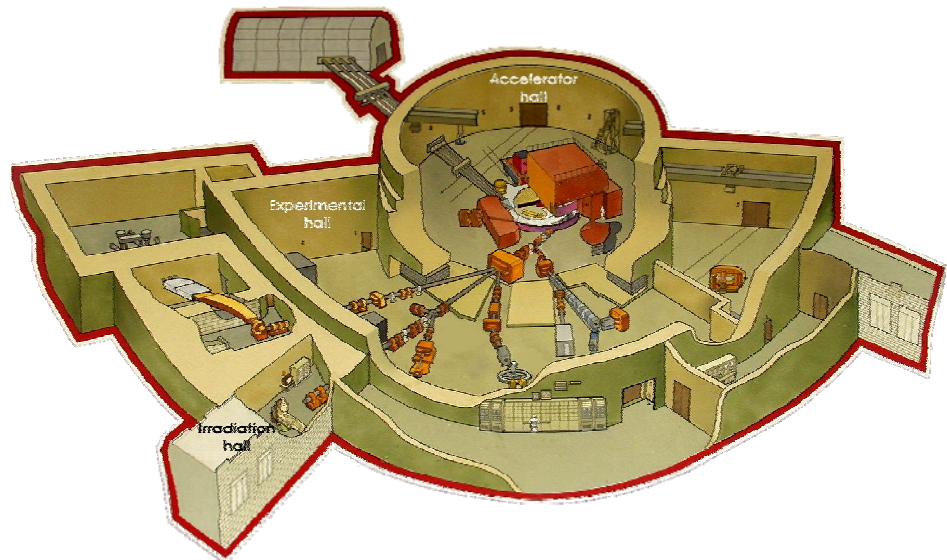


Fig. 2. Artistic view of synchrocyclotron and experimental halls

The irradiation zone a narrow beam of 6 mm in diameter with sharp edges. The beam is transported in a vacuum pipe to prevent the multiple scattering and inelastic interactions of protons in the air.

The irradiation hall is separated from the experimental hall by two shielding walls made from iron and concrete provided the radiation background in the hall at quite low level. The beam position in the accelerator and experimental halls as well as in the irradiation hall and the beam intensity are under a permanent control from the accelerator and medical control

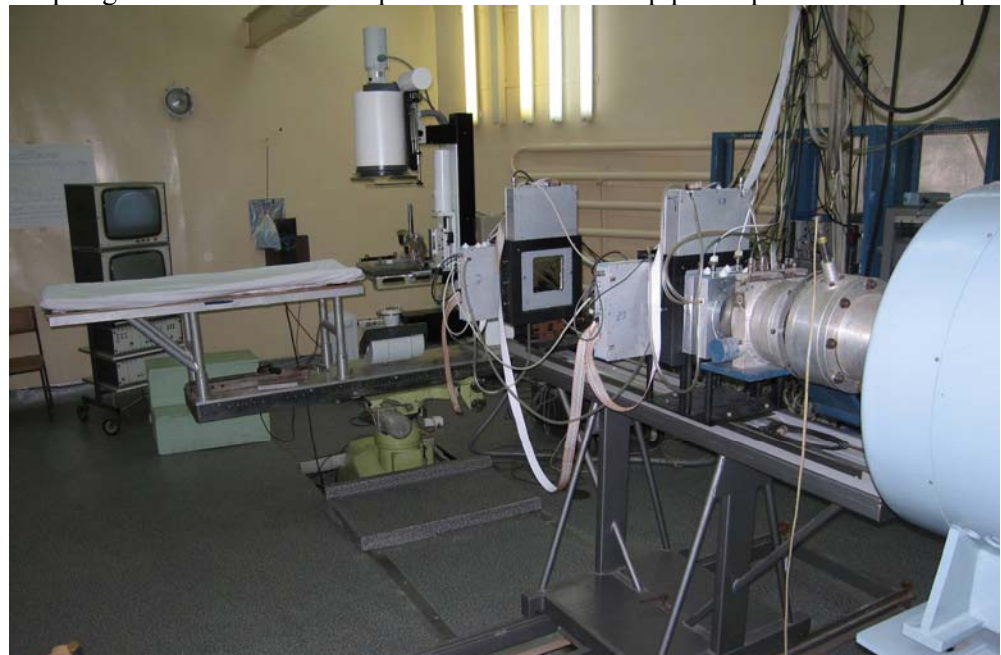


Fig. 3. Irradiation hall

rooms. Any deviation of the beam parameters beyond the reset limits stops immediately the acceleration process in the synchrocyclotron thus excluding completely any danger for irradiated patients. In 2002–2004 the upgrade of proton medical beam-line has been done including the construction of new collimators and special profilemeters of proton beam in accelerator and experimental halls.

In this paper we present the upgrade of proton beam-line only in the irradiation hall. Profiles in the irradiation hall are measured by two multiwire proportional chambers (XOZ plane) with a gold-tungsten anode wire of $20\ \mu\text{m}$ diameter and stainless steel cathode wires of $50\ \mu\text{m}$ diameter. The wire spacing is 1 mm, the surface of entrance window is $128 \times 128\ \text{mm}^2$.

The final proton distribution at the position of patient head on the rotation table is measured by the silicon detector precisely moving along the X-axis by step of $153\ \mu\text{m}$ and along the Z-axis by $9\ \mu\text{m}$. The range of such scanning is $25 \times 25\ \text{mm}^2$. Profiles of proton intensity at the isodose center of irradiated target is shown in Fig. 4. The intensity of proton beam in the irradiation hall is measured by MWPC in current regime and then transformed into dose distributions, which are periodically calibrated by diamond detectors.

The constancy of a planning dose for each patient irradiation is controlled from accelerator and medical control rooms. The dose distribution during the patient irradiation is shown in Fig. 5. All elements of proton medical beam-line were upgraded by the installation of new mechanical systems and the change of electronics of all detectors to the contemporary base ones. The movable patient's table seen in Fig. 3 provides pendulum-like oscillations in the horizontal plane around the Z-axis within $\pm 40^\circ$.

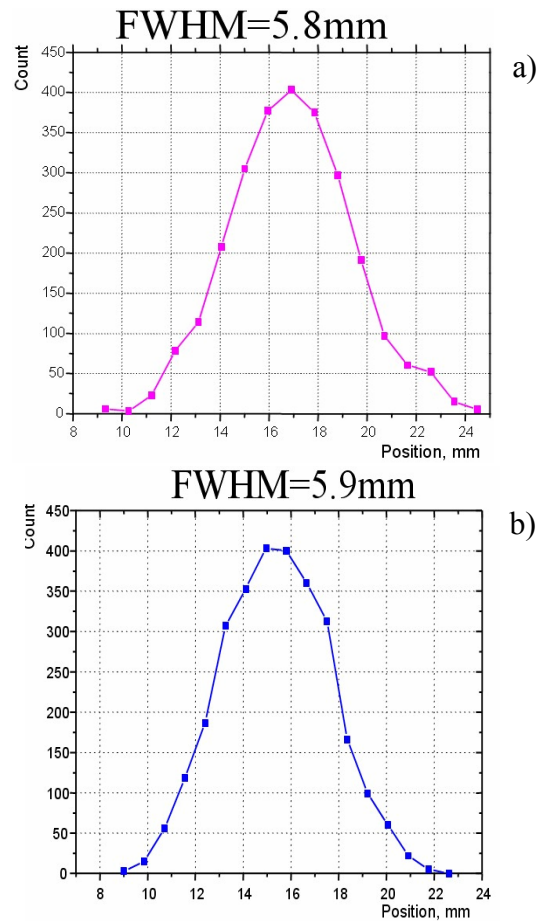


Fig. 4. Vertical (a) and horizontal (b) profiles of proton beam at the isodose center of irradiated target

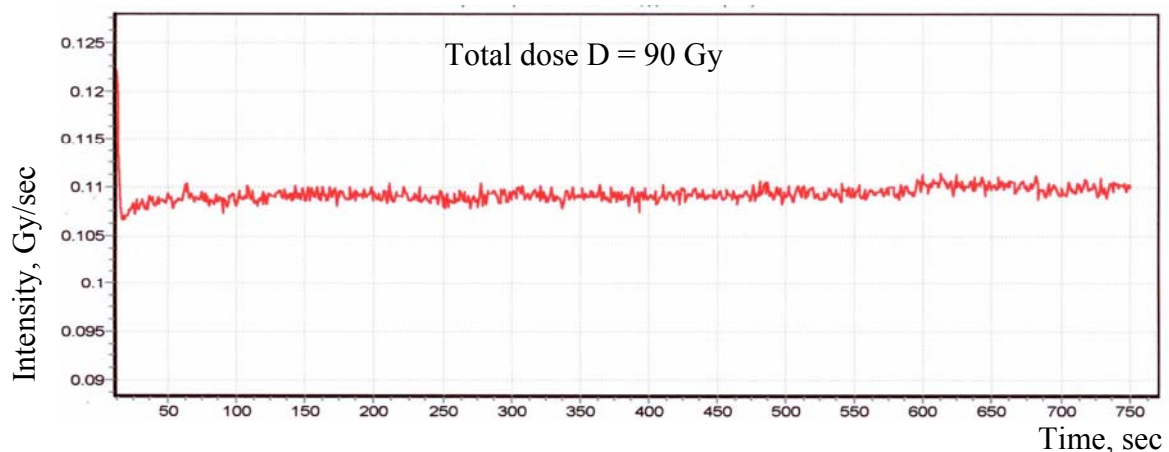


Fig. 5. Distribution of proton beam intensity during the patient irradiation

The anterior part of the table represents a head fixation device performing an independent pendulum-like oscillation about the X-axis within $\pm 36^\circ$. The crossover of the X- and Z-axes is the center of rotation (isocenter). The adjustment system allows to locate the isocenter precisely in the beam axis. Then the patient's position on the table is regulated in such a way that the zone selected for irradiation would be exactly in the center. This zone is determined in the hospital by computer tomography, and its coordinates are put in the protocol. The installation procedure in the irradiation hall

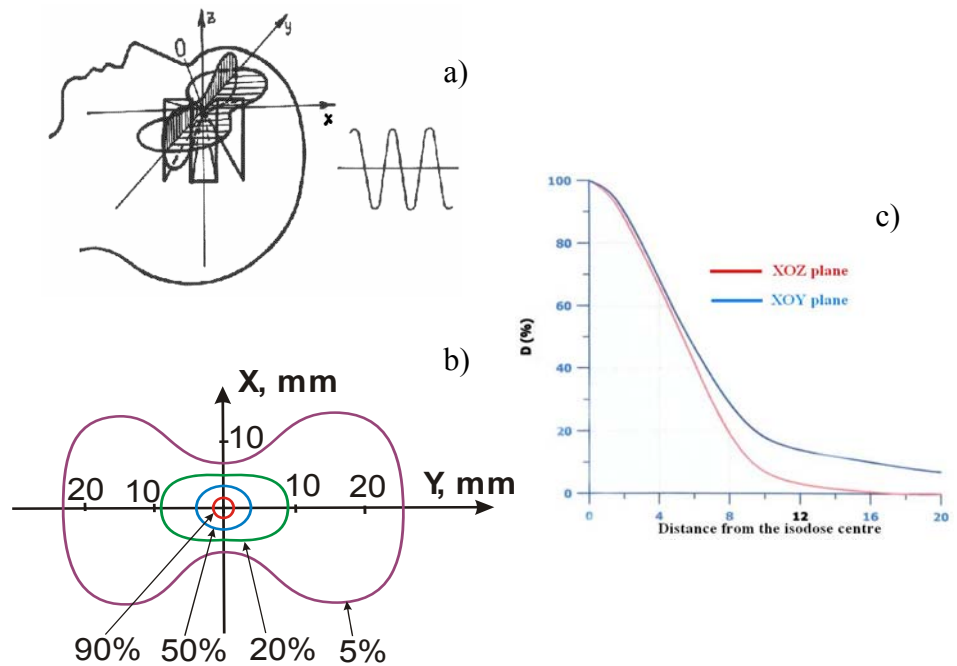


Fig. 6. Scheme of the patient's head rotation around Z- and X-axes. The proton beam is directed along Y-axis. a) The beam trajectories over the patient's head surface at simultaneous rotation of patient's table and head fixation device. b) Spatial distribution of the radiation dose for beam size $X = Z = 6$ mm. Isodoses: 1 – 90%, 2 – 50%, 3 – 20%, 4 – 5%. c) Profiles of dose distribution in planes X0Z and X0Y (distance in mm)

is performed by means of a special head mask under the control of a high sensitive X-rays setup, which has fixed positions – along the Z-axis and along the beam Y-axis. The final precision in such installation is better than 1 mm. Figure 6a shows the scheme of simultaneous rotation of the patients table and head fixation device and also beam trajectories on the patient's head. Figures 6b-c show the dose distributions in X0Z and X0Y planes, which characterized very sharp decreasing in both directions.

3. Patient's treatment procedure and results of the therapy

The procedure of patient's treatment is the same as it was described in Ref. [1]. This work included the localization of the zone for irradiation relative to the reference points on the head surface and the preparation of the special head mask used to fix firmly the patient's head on the table for irradiation. The time necessary for positioning of the patient on the table for the irradiation is 15–20 min, and the irradiation time ranges from 8 to 20 min. The oscillation movements of the patient's head proceed quite slowly, so the patients practically do not notice it. The proton therapy is painless, and it is carried out without anesthesia. During the irradiation process the doctors perform continuous control of the patient's state (pulse, breath rate, ECG). There is also a television control and audio communication with the patient from the control room. Statistics of proton therapy at the PNPI synchrocyclotron is presented in Fig. 7.

The dynamics of patient's treatment in 2002–2006 is shown in Fig. 8. Unfortunately, it has a negative tendency and the number of patients treated for this period is less than the corresponding number during 1985–1989 by a factor of two. In some cases such tendency can be explained by the increased competition between neurosurgical and radiological methods of patient's treatment. We observed in the case of pituitary adenomas increased number of patients undergoing a prior surgical operation but not always successful.

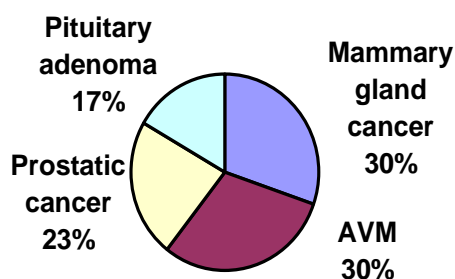


Fig. 7. Number of patients treated at the PNPI-RSCRST medical center during 2002–2006. Pituitary adenoma – 17%, AVM – 30%, mammary gland cancer – 30%, prostatic cancer – 23%. In total 132 patients

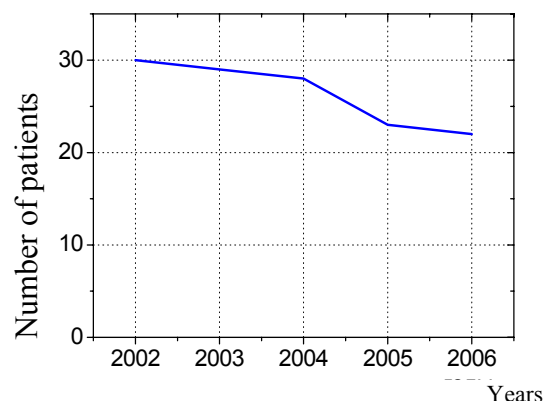


Fig. 8. Dynamics of treated patients

Other possible reason of patient's number reduction can be the total decreasing of inhabitants in Russia, especially in the North-West region of former USSR.

3.1. Proton therapy of pituitary adenomas

Pituitary adenomas comprise about 10–12% of all intracranial tumors¹. They can be classified as benign histologically but can cause morbidity and occur through hormonal imbalances and functional deficits. Various radiation techniques such as gamma knife and linear accelerator-based stereotaxic radiosurgery² as well as charged-particle therapy^{3,4} are used for the treatment of such diseases. The application of narrow 1000 MeV proton beam for the irradiation of intracranial tumors (Gatchina transmission method [1]) is very effective, especially in the treatment of different pituitary adenomas. In the case of the somatotropinomas in total 201 patients were treated during 1975–2006. The clinical remission observed during from 1 to 10 years was achieved for 83% patients with macroadenomas. The remission was manifested by the disappearance of tumor growth, the regress of the acromegaloid syndrome, the normalization of carbohydrate exchange and the restoration of working capability. In Fig. 9 the distribution of growth hormone (GH) concentration in blood of patients before and after proton therapy at the dose of $D = 80$ CGE observed during 5 years is shown. The number of patients analyzed during five years is 85.

It is seen in Fig. 9 that after 5 years the GH concentration is within the limits of physiological normal value 2.8 ± 0.3 ng/ml. The stabilization of symptoms is observed for 4% of patients, while there is no effect in 13% cases mainly when initial symptoms of the tumor arte spread out of borders of the turkish saddle. In the treatment of the prolactinomas (115 patients, 4 of them in 2002–2006) the clinical remission was stated in 80% cases of patients with microprolactinomas. It was accompanied by the disappearance of the galactorrhea, the restoration of the ovarian menstrual cycle, the decrease of prolactin concentration and the stop of tumor's growth. In Fig. 10 the change of prolactin concentration in blood of treated patients after proton irradiation is shown. After 5 years such level is close to the normal one, corresponding in average more than 50% its reduction. Thirty women had a pregnancy ended in a live birth. The stabilization was observed in 17% cases, in which the decrease of prolactin concentration was less than 50%. The treatment of corticotropinoma adenomas (Icenko-Cushing's syndrome) is the most successful kind of pituitary adenoma proton therapy. From 205 (10 in 2002–2006) treated patients the clinical remission was observed in 96% cases, the stabilization – in 1%, and only in 3% cases there was the progress in the growth of a tumor.

¹ B.B. Ronson *et al.*, *Inter. J. Radiation Oncology, Biol. Phys.* **64**, 425 (2006).

² M. Shin *et al.*, *Biomed. Pharmacother* **56**, 178 (2002).

³ B. Konnov, L. Melnikov *et al.*, in *Proceedings of the International Workshop on Proton and Narrow Photon Beam Therapy*. Oulu, Finland, 1989. p. 48

⁴ Y.I. Minakova, L.Y. Eirpattovskaya *et al.*, *Med. Radiology* **28**, 7 (1983).

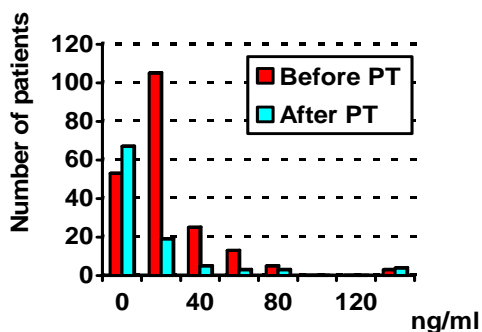


Fig. 9. Distribution of GH (growth hormone) concentration of patients before and after proton therapy (PT) for 5 years observation. Somatotrophic pituitary adenoma. Total number of patients before PT is 201

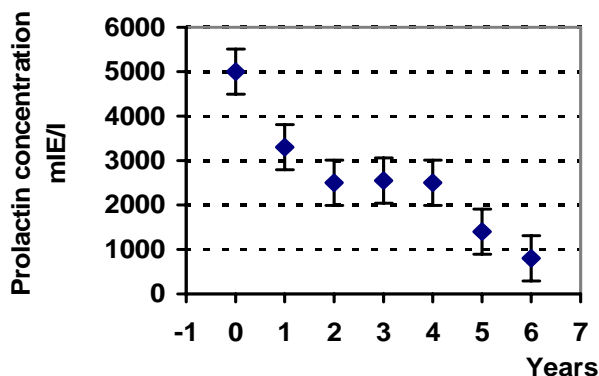


Fig. 10. Dependence of prolactin concentration as a function of time observation patients after proton therapy

In the case of the clinical remission the Icenko-Cushing syndrome was stopped already after 3 months of the irradiation. One can observe the decrease of ACTG and the cortisol secretion as well as the restoration of daily secretion rhythm. Women undergoing proton irradiation further had normal pregnancy and gave birth to child without the indication of endocrin pathology. Photo of patient K. (woman since 19 years suffered from Icenko-Cushing's syndrome) before (2003) and after (2005) proton irradiation at $D = 80$ CGE with normal child is shown in Fig. 11. One can note that usual neurosurgical operations do not give women the possibility to have pregnancy and to give birth to a child.



Fig. 11. Photos of patient K. with Icenko-Cushing syndrome before and after proton therapy

3.2. Proton therapy of cerebral arteriovenous malformations (AVM)

Surgical practice shows that only about 50% of AVM is medicable in clinics, especially in cases when AVM is placed in critical or inaccessible zones of head brain. Proton therapy of AVM with rather small volume – not more than 8 cm^3 – gives the positive result in 74% cases without any influence on neighboring life-important parts of the brain at doses of 40–80 CGE. The complete elimination of the AVM from the blood circulation is observed in 65% cases. This process continued for a year after the irradiation. For AVM's volume appreciably more than 8 cm^3 only in 27% cases one can have the positive result. After the proton therapy the majority of patients revealed a complete or partial regress of the neurologic symptoms, discontinuation or decrease of the rate and degree of epileptic attacks. The total number of patients treated in 1975–2006 is 491, in 2002–2006 – 40, from them 144 patients were treated secondly. To improve results of AVM's large volume treatment it is necessary to develop new methods of proton stereotaxic therapy or to use beams of more dimensions.

3.3. Proton therapy of mammary glands and prostatic cancer

In 2002–2006 the treatment of 40 patients with mammary gland cancer and 30 patients with prostatic cancer have been performed. The total number for 30 years is 184 and 117, correspondingly. In such treatment the irradiation of special zones of pituitary gland was used.

4. Proposal for 200 MeV proton therapy at PNPI-RSCRST medical center

As it was written above, the number of patients treated in last years at 1000 MeV proton beam is decreasing due to some reasons, main of which is the small number of patients with intracranial diseases of head brain in St.-Petersburg and even over the North-West region of Russia. According to estimates of different experts, the number of patients with pituitary adenomas, AVM and some others are approximately 2–3% of total patient's number with oncological tumors. For example, in St.-Petersburg there are about 100000 citizens suffered by cancer and every year this quantity is increasing by 20000 new patients. The PNPI method of stereotaxic 1000 MeV proton therapy is unique over the world; this method shows better results in pituitary adenoma treatment than widely used Bragg peak method and it needs to continue its performance with some upgrade of diagnostic tools. Taking into account very sharp necessity of St.-Petersburg in radiotherapy, which is satisfied only on 6–7%, the PNPI-RSCRST Medical Center suggests to use for the treatment of wide spectrum of cancer's diseases a new proton beam of 200–250 MeV providing the irradiation of patient's tumor by the Bragg peak method. Such proton beam is obtained by lowering the initial proton energy (1000 MeV) in a degrader, placed just at the exit of accelerator, up to required energy (see Fig. 2). Then 200 MeV proton beam is transported into the irradiation hall. The PNPI Accelerator Division has already the experience in obtaining 900–200 MeV proton beams for physical experiments [3]. Parameters of a new special medical beam line were calculated using GEANT 3, MESON and OPTIMUM codes. In Figs. 12–13 results of Monte Carlo simulations of horizontal and vertical proton beam profiles as well as the proton momentum distribution at the target position in the irradiation hall are shown. The intensity of the beam is equal to 8×10^8 p/sec, that corresponds to the accumulated dose of 12 Gy/min.

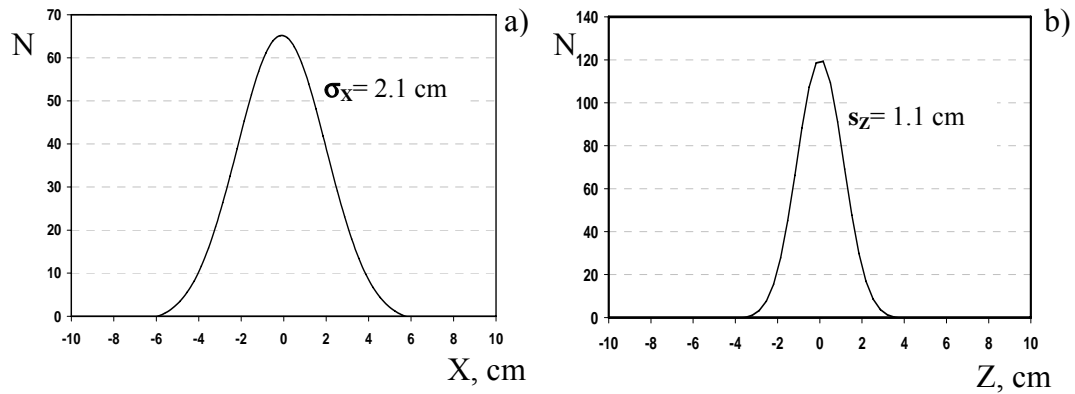


Fig. 12. Horizontal (a) and vertical (b) profiles of 200 MeV proton beam at the place of irradiated target in the irradiation hall. The distance from the exit of 1000 MeV proton beam in accelerator hall to irradiated target is 53 m

Such dose rate is enough for the multifractional irradiation of tumors by area of 15–20 cm² and even more using special device for conformal therapy. In the absence of special medical accelerators in Russia the upgrade of existing machines proposed for physics research (as, for example, Dubna synchrocyclotron⁵) to perform hadron radiotherapy is at present a real way in the improvement of total situation in cancer treatment.

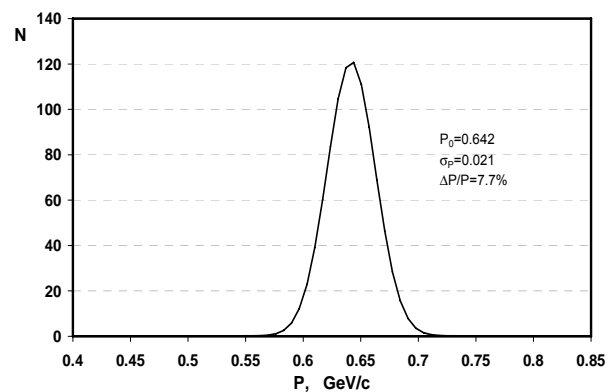


Fig. 13. Momentum distribution of 200 MeV proton beam in the place of the target in irradiation hall

5. Conclusion

The use of the 1000 MeV proton beam for stereotaxic therapy at the PNPI-RSCRST Medical Center has demonstrated the high efficiency of this method. The combination of the rotation irradiation technique and narrow proton beam with sharp edges allowed to deliver large radiation doses to small targets selected for the irradiation without damaging of neighbor volumes in the proximity to the life-critical zones of head brain. The treatment of 132 patients in 2002–2006 and of total 1320 patients for 30 years showed a high reliability and safety of the method, none of the patients had any complications related with the quality of irradiation process. As before 1000 MeV proton therapy can be applied for the treatment of wide spectrum of head brain diseases, in particular, pituitary adenomas. Upgrade of PNPI Medical Facility and the construction of a new 200 MeV beam-line will allow to satisfy in the most extent the need of the North-West region of Russia in bloodless radiosurgery.

References

1. N.K. Abrossimov *et al.*, in *PNPI XXV, High Energy Physics Division. Main Scientific Activities 1971–1996*, Gatchina, 1998, p. 295.
2. N.K. Abrossimov *et al.*, *Journal of Physics: Conference Series* **41**, 424 (2006).
3. N.K. Abrossimov *et al.*, Preprint PNPI-2525, Gatchina, 2003. 31 p.

⁵ A.V. Agapov *et al.*, *Particles and Nuclei Lett.* **2**, № 6 [129], 80 (2005).

DEVELOPMENT AND ON-LINE TESTS OF DIFFERENT TARGET-ION SOURCE UNITS FOR PRODUCTION OF NUCLIDES FAR FROM STABILITY

V.N. Panteleev, A.E. Barzakh, D.V. Fedorov, A.M. Ionan, V.S. Ivanov, K.A. Mezilev, P.L. Molkanov, F.V. Moroz, S.Yu. Orlov, Yu.M. Volkov

1. Introduction

The work carried out has as a general goal the development of a massive (up to 1 kg) uranium carbide target prototype for the third generation ISOL facilities, where two-step reactions will be used to produce intense neutron-rich nuclear beams.

For more than thirty years UC_x targets have been explored for the production of a large set of neutron-rich and neutron-deficient heavy nuclei. The main line of uranium carbide target development was the creation of the target material with a high dispersivity and porosity in order to decrease the release time of the species produced by different reactions in the target material, which is mainly determined by the diffusion and effusion processes. On the other hand, for a more efficient use of a neutron beam after the primary beam converter the density of the target material containing uranium should be as high as possible. Additionally, the target material with a higher density has a higher thermal conductivity that would allow dissipating a higher power introduced into the target by the primary beam, when the target is used for exotic nuclei production in the direct reaction. Hence, for more effective production of short-lived isotopes of the element chosen for the investigation, a special selection of a metal carbide target material is required – concerning not only the target material structure but also its density. At the IRIS (Investigation of Radioactive Isotopes at Synchrocyclotron) facility in Gatchina uranium carbide target materials of different structure and density have been tested.

The first general goal of the work is to find out whether the high density uranium carbide can be competitive with presently used low density UC_x targets in the production of short-lived nuclei far from stability. The yields and release characteristics are reported here to compare properties of tested target materials. The second goal is the development and tests of an effective, high-temperature target unit for the on-line production of short-lived rare nuclides. The peculiarity of the developed target unit is the absence of the ion source [1]. The ionization process happens in the target volume itself, so it can help to avoid an additional delay time due to the effusion inside the transfer tube and the ion source. The combined target-ion source (CTIS) unit could be especially useful for the production of isotopes of hard volatile elements with long sticking time, such as rare-earth elements Gd and Lu, and of many other nuclides with boiling points higher than 3000°C. The use of tungsten container [2] instead of a traditional tantalum one allowed to rise the target working temperature up to 2500°C, thereby decreasing the delay time for nuclides produced in the target and hence increasing the yield of short-lived isotopes. At the same time, a high work function of tungsten ensures a high efficiency of a surface ionization of the species with the ionization potentials lower than 6 eV produced in the target material.

2. Target materials tested on-line

A schematic view of the typical target unit used for different uranium carbide target material tests is shown in Fig. 1. As a first step in that comparison, the isotopes of alkali elements Rb, Cs and Fr have been selected for the yield and release efficiency measurements. The main reason of such a choice was their high ionization efficiency (theoretically up to 100%) on the hot inner surface of the target-ion source unit, that allows to obtain short-lived nuclei far from stability. This is very important for the target material comparison.

The second important point in the selection of alkalis is that the target construction can be very simple, including only the tungsten target cavity (ionizing target) [3], as the ionization process happens inside the target container itself. It allows to avoid some uncertainties concerning possible temperature difference of the tested units, as in that case only one parameter (the target container temperature) should be controlled in the course of the experiment.

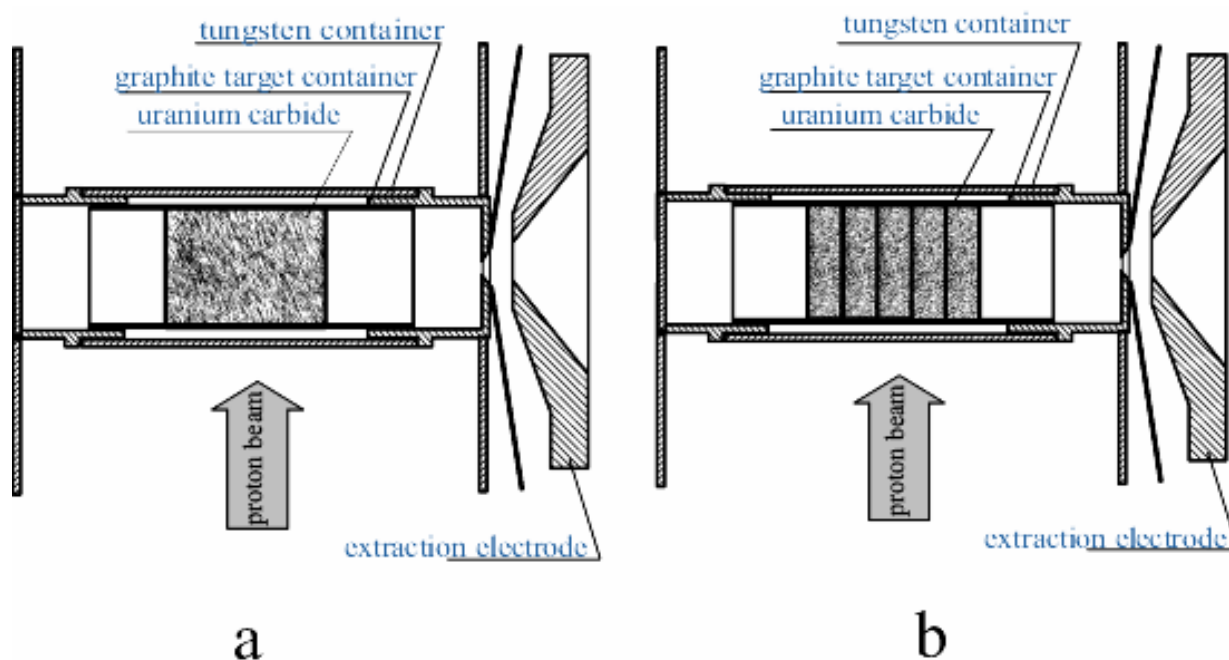


Fig. 1. Schematic drawings of a) high density rod (HDR) uranium carbide target; b) high and low density pellet uranium carbide target

Three kinds of the target materials were studied: a high density UC rod; a low density UC_x target prepared by the ISOLDE method at the IRIS facility (as few pellets placed transversely to the axis of the target); a high density UC powder target material prepared by the method of the powder metallurgy. The high density rod (HDR) target had the following characteristics: uranium rod density 11 g/cm³, target thickness 6.7 g/cm², about 6 mm length and 11 mm in diameter. The grain size was about 200 μm. The low density target (LDT) had: uranium density 2.3 g/cm³, target thickness 2.8 g/cm², about 12 mm length and 11 mm in diameter; 8 pellets, each of 1.2–1.6 mm thickness with the grain size about 20 μm. This target material has been prepared by the Orsay–PNPI collaboration at the IRIS facility, using the ISOLDE technology, a similar graphite powder brought by Orsay group and uranium dioxide from Russian producers. This target is also referred later as ISOLDE like or PARRNe-IRIS. The high density powder (HDP) target had: uranium density 12 g/cm³, target thickness 6.3 g/cm², length 5.25 mm, diameter 11.2 mm; 3 pellets, each of 1.6–1.9 mm thickness, grain size about 20 μm. Targets were operated in the temperature range of 1900–2200°C. The investigated target materials were maintained in the target containers of the same dimensions and geometry. More detailed description of used target construction can be found in Refs. [4, 5]. The uranium fission reaction was produced by 1 GeV proton beam with the intensity of 50–70 nA. Mass-separated isotope beams were collected on a tape station and were either transported to γ , β , α -counting stations or directly counted by α -detector to be identified by the characteristic lines. Detailed description of γ -rays measurement and yield determination can be found in Ref. [4]. The yields of Cs isotopes were determined by means of β -counter as well as of γ -detector. Fr isotopes were produced in the same targets by the spallation reaction. The Fr isotope yields were measured using γ -rays and α -particles. To get consistent yield data obtained by α - and γ -measurements, the α -yield data were normalized to the yields obtained by γ -measurement (as the efficiency of the Ge detector is well known), taking as normalizing coefficient the yield ratio for isotopes measured by both methods.

2.1. Yield comparison

For the investigated target materials the Cs and Fr yields under similar temperature conditions ($T = 2100^\circ\text{C}$) have been determined. All presented yield values were normalized to a target thickness of 1 g/cm^2 and $0.1 \mu\text{A}$ proton beam current. The error of the temperature measurement for different targets can reach 50°C . The experimental errors of the obtained yield values are within the limits of 30% for isotopes not far from stability and of 80% for short-lived neutron-rich isotopes. Cs yields from the investigated targets are plotted together with the ISOLDE yields obtained for standard target at the PS-Booster and for graphite cloth target at the synchrocyclotron. As one can see in Fig. 2, there is a good agreement of yields from similar target materials of ISOLDE and PARRNe-IRIS. The yields of short-lived Cs isotopes from a HDR target are 1.5–2 times lower. This fact demonstrates its lower release efficiency than the ISOLDE or PARRNe-IRIS

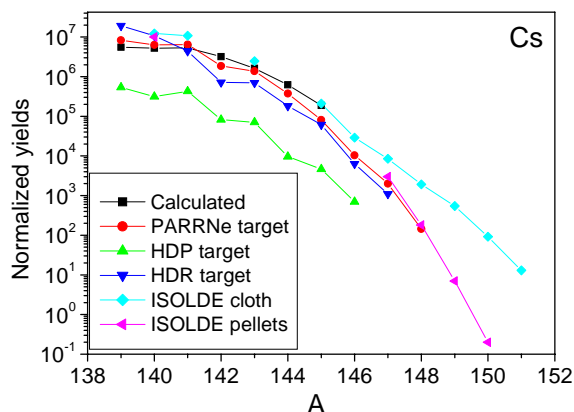


Fig. 2. The yields of Cs isotopes released from a high density rod, high density and low density pellet targets at 2100°C . The yields from ISOLDE UC_x pellet target are presented. The yields calculated on the basis of measured cross section are shown as well

target production rate of the investigated isotopes. The enhancement of the yield of ^{139}Cs from the HDR target respectively to the calculated one can be explained by the decay of the mother ^{139}Xe nucleus that has the production cross section comparable to the Cs daughter nucleus. It is worth stressing that the yield excess in respect to the calculated yield values was measured only for Cs isotopes produced from the HDR target. It can indicate that in the HDR target the Xe precursors may have longer release times, therefore allowing a large probability of decay in the target as an additional production mode. That assumption requires a special verification.

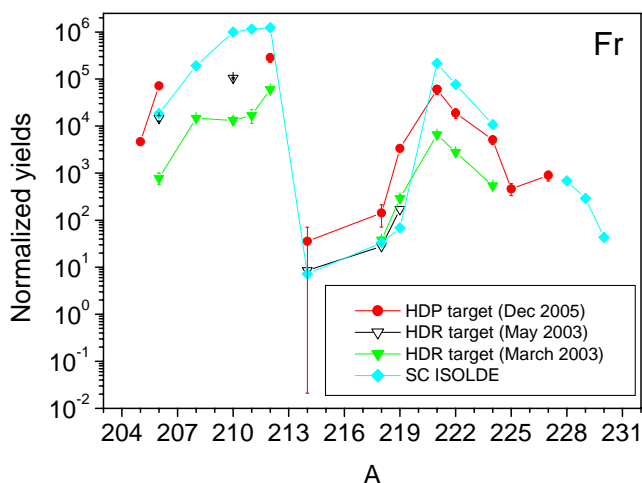


Fig. 3. The yields of Fr isotopes from the HDR, HDP and ISOLDE graphite-cloth targets

target. It is an expected result, as the grain size of the HDR target is 10 times larger. Therefore the diffusion process should be much slower. The yields measured for Rb isotopes, which are not presented here, confirm the results obtained for Cs. The Cs yield trend from the lately developed HDP pellet target is similar to the fast PARRNe-IRIS target, but the efficiency is about 20 times less. It can be explained by a strong carbonization of the inner surface of the target container that leads to the ionization efficiency decrease, as the HDP target had been outgassed much longer time than other targets. The calculated yields based on the experimental cross sections are also presented to show the in-

target production rate of the investigated isotopes. The enhancement of the yield of ^{139}Cs from the HDR target respectively to the calculated one can be explained by the decay of the mother ^{139}Xe nucleus that has the production cross section comparable to the Cs daughter nucleus. It is worth stressing that the yield excess in respect to the calculated yield values was measured only for Cs isotopes produced from the HDR target. It can indicate that in the HDR target the Xe precursors may have longer release times, therefore allowing a large probability of decay in the target as an additional production mode. That assumption requires a special verification.

It should be specially pointed out the extraordinary high yields of short-lived Rb and Cs obtained from the ISOLDE graphite cloth UC_x target at the SC. Unfortunately, these high yield data were not reproduced at the PS-Booster, where presently the ISOLDE standard powder-pellet UC_x target is used. In Fig. 3 the yields of Fr isotopes from the HDR and HDP targets are presented. Fr isotopes have not been measured from PARRNe-IRIS target. The yields of short-lived ^{214}Fr ($T_{1/2} = 5 \text{ ms}$), ^{218}Fr ($T_{1/2} = 1 \text{ ms}$) and ^{219}Fr ($T_{1/2} = 21 \text{ ms}$) were measured by detection their characteristic α -decays. The yields of isotopes with longer half-

lives were determined using both α -particles and γ -rays. The Fr isotope yields obtained at the ISOLDE from the UC_x graphite-cloth target are also shown in the graph. The normalized yields of long-lived Fr isotopes from the ISOLDE graphite-cloth target are higher than from the HDR and HDP targets. The lower HDR and HDP target efficiency, which is the product of the ionization and release efficiencies, may be explained by lower value of the ionization efficiency of the ionizing targets used for experiments, where the ionization process takes place on the strongly carbonized inner surface of the target container. But, at the same time, the normalized yields of short-lived ²¹⁴Fr, ²¹⁸Fr, ²¹⁹Fr are equal or even higher than the yields of these short-lived isotopes from the ISOLDE target. As there was only one measurement of the Fr yields from a newly developed HDP target, we give here the obtained yield values from that target as preliminary ones.

2.2. Comparison of the target release properties

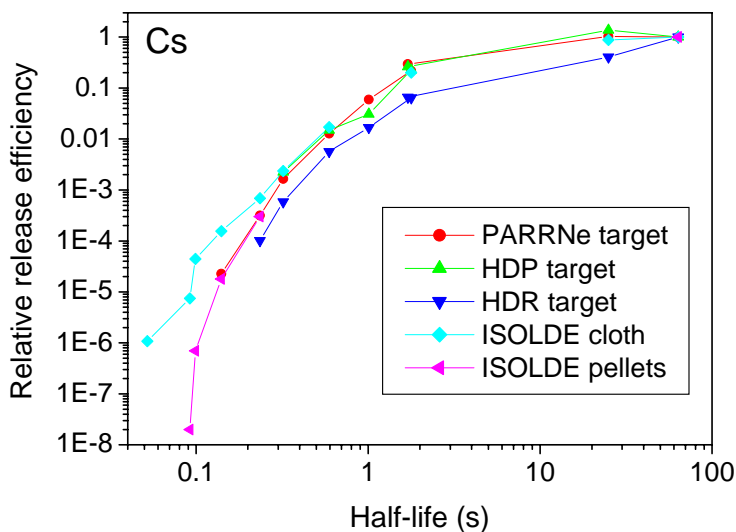


Fig. 4. Comparison of the Cs yield trends from HDR, HDP, LDP PARRNe IRIS and ISOLDE targets. The yields are normalized at the yield point of ¹⁴⁰Cs with the half-life $T_{1/2} = 63.7$ s

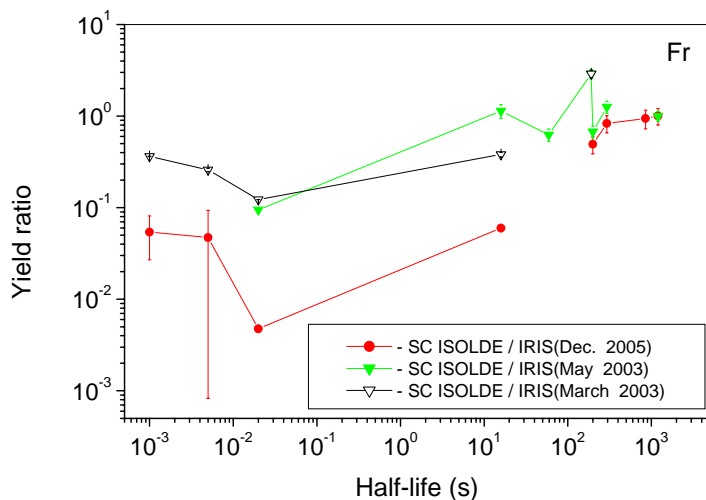


Fig. 5. Ratio of the yields of Fr isotopes from ISOLDE graphite-cloth target to the yields of the same isotopes from HDR (triangles) and HDP (circles) targets, plotted as a function of the half-lives. The obtained ratios are normalized at the point ²¹²Fr with the half-life $T_{1/2} = 20$ min

The comparison of the relative release efficiencies of different targets for produced isotopes has been derived by normalizing the obtained yield values to the yield of a long-lived isotope ¹⁴⁰Cs ($T_{1/2} = 63.7$ s) which is produced with the efficiency close to unity. In Fig. 4 the relative release efficiencies of Cs isotopes are presented as functions of their half-lives. The trend of the normalized yield values demonstrates that the ISOLDE and PARRNe-IRIS targets in general are slightly faster than the HDR target. A rather promising result is that the trend of the relative efficiency curve for the newly developed HDP target coincides with one of the ISOLDE target.

For comparison of the Fr release efficiencies, the yields from the ISOLDE cloth target were divided by the measured yields of the same isotopes from the HDR and HDP targets and normalized to the yield ratio of ²¹²Fr. The obtained ratio values are shown in Fig. 5 as functions of the half-lives; as the Fr isotopes were not studied with the PARRNe target, only the ratios for the HDR and HDP targets are presented. The result for the HDP target is preliminary. As one can see, the HDR and HDP targets has considerably higher release efficiency for short lived-isotopes of ²¹⁴Fr ($T_{1/2} = 5$ ms), ²¹⁸Fr ($T_{1/2} = 1$ ms) and ²¹⁹Fr ($T_{1/2} = 21$ ms). This can be explained by the fact that the sticking and flight time of species produced in the IRIS tested target prototypes is about six time less than in the ISOLDE target due to the ratio of the volumes of the target containers. To confirm or to reject the

assumption of a much shorter effusion time some additional on-line tests on the short-lived Fr isotope production from a HDP target will be carried out at the IRIS facility.

3. Ionizing targets for production of nuclides with high ionization potentials

For the production of nuclides with high ionization potentials three types of combined targets have been developed and on-line tested:

1. The ionizing foil target of the surface ionization for the Li and rare-earth isotope production.
2. The laser foil target for the production and resonance laser spectroscopy investigation of neutron-deficient rare-earth isotopes.
3. The combined target-ion source unit of the electron beam ionization with uranium carbide as a target material for the production of neutron-rich isotopes of the elements with the ionization potentials higher than 6 eV.

3.1. Off-line measurements of the ionization efficiencies for Li, Sm, Eu, Tm, and Yb

The schematic diagram shows the high-temperature ionizing target [6] used for on-line tests (Fig. 6). The only difference in the construction of the ionizing target (IT) used for off-line ionization efficiency measurements was the presence of a separately heated oven which was connected to the IT for a slow evaporation of the sample consisting of a known amount of atoms of the element being investigated.

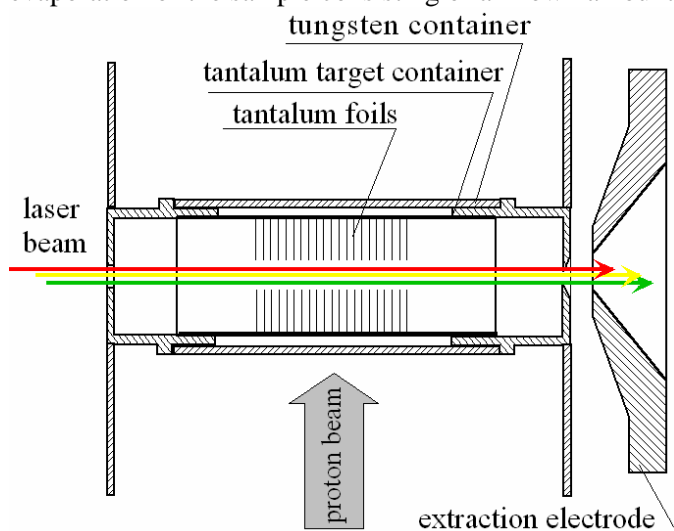


Fig. 6. Scheme of the combined target-ion source unit for Li, rare-earth isotope production and laser spectroscopy experiments

Off-line measurements of the surface ionization efficiencies for Li and rare-earth elements was carried out by using samples of LiF and oxides of pointed out rare-earth elements weighting from 10 to 20 μg placed into the oven connected with the IT volume. The current of each evaporated sample was measured by a Faraday cup placed in the focal plane of the mass-separator magnet and connected with the current integrator. The process of the laser ionization efficiency measurement of Eu and Gd atoms inside the target volume was carried out simultaneously with the surface ionization measurement. For that purpose three laser beams tuned in resonance with appropriate transitions in

Eu and Gd were introduced into the CTIS. We indicate this method as the laser target (LT) [7], in order to emphasize that it differs from the method employing the resonance ionization in the laser ion source (LIS) [8].

In Table 1 the efficiencies of surface and laser ionization measured off-line for some alkalis and rare-earth elements are presented. The error of the ionization efficiency measurements was 20% for Rb and Cs and up to 40% for other elements.

The efficiencies of ionization measured off-line with IT and LT

Table 1

Element	Temperature, °C	Surface ionization efficiency, %	Laser ionization efficiency, %
Li	2000	6	
Rb	2000	40	
Cs	2000	55	
Sm	2200	7	
Eu	2200	10	7
Gd	2500	2	1
Tm	2200	3	
Yb	2200	5	

3.2. On-line measurements of the yield of neutron-deficient rare-earth isotopes

A 1 GeV proton beam induced spallation reactions in the target material (tantalum foils, target thickness 3 g/cm²) producing nuclides of neutron-deficient isotopes of rare-earth elements. After surface or laser ionization and extraction from the target, the ions were separated by a mass-separator and implanted into a moving tape installed at one of the three beam-lines of the IRIS facility. An identification of the radioactive implanted specimens and yield determination were performed by means of appropriate γ -line measurements by a coaxial high-purity germanium detector. The proton beam intensity was 0.05 μ A. In Table 2 the yields of the neutron-deficient rare-earth isotopes produced on-line, the yields calculated by the EPAX code and the values of the efficiency of the ionizing target are presented.

Table 2

On-line yields and production efficiencies of the IT at 2500°C

Nuclide	$T_{1/2}$	Yields measured, s ⁻¹	Yields EPAX, s ⁻¹	Production efficiency by surface ionization, %	Production efficiency by laser ionization, %
¹³⁸ Eu	12.1 s	2.4×10^3	9.5×10^4		
¹³⁹ Eu	17.9 s	1.6×10^4	4.9×10^5		
¹⁴¹ Eu	41.4 s	4.0×10^5	5.6×10^6		
¹⁴² Eu	1.22 min	4.1×10^5	1.2×10^7		
¹⁴³ Eu	2.57 min	2.0×10^6	2.1×10^7	9	
¹³⁹ Sm	2.57 min	2.8×10^5	8.4×10^6		
¹⁴³ Sm	66 s	4.4×10^5	2.3×10^7		
¹³⁹ Pm	4.15 min	3.1×10^5	2.6×10^7		
¹⁶⁰ Tm	9.4 min	5.0×10^5	3.5×10^6		
¹⁶⁴ Tm	5.1 min	9.6×10^4	1.6×10^7		
¹⁶⁰ Yb	4.8 min	1.0×10^6	1.6×10^7	6	
¹⁶⁰ Lu	40 s	2.2×10^4	1.5×10^7		
¹⁶⁸ Lu	6.7 min	1.3×10^6	4.1×10^6		
¹⁴³ Gd	39 s	6.7×10^4	3.5×10^6		
^{143m} Gd	1.87 min				
¹⁴⁵ Gd	23.0 min	6.7×10^5	1.7×10^7	4	2
^{145m} Gd	85.2 s				

For ¹⁴³Gd and ¹⁴⁵Gd the total values of the yields summarizing the measured isomeric and ground states are given. The efficiency of the laser target for ¹⁴⁵Gd production is pointed out as well. The combined target-ion source unit efficiency, which is a product of the release and ionization efficiency, was obtained as the ratio of the measured yields to the yields calculated on the base of cross sections supplying by the EPAX code. That efficiency estimation was obtained only for isotopes with respectively long half-lives and which production cross sections are close to the maximum of the cross section curve (¹⁴³Eu, ¹⁴⁵Gd and ¹⁶⁰Yb). As one can see in Table 2, the on-line production efficiencies for pointed out long-lived isotopes are in a good agreement with the off-line measured values (Table 1).

3.3. The CTIS use for on-line laser spectroscopy experiment

The developed combined target-ion source unit has been used for a laser resonance spectroscopy investigation of neutron-deficient Gd isotopes [7]. The scheme of the CTIS used for the laser spectroscopy experiments is shown in Fig. 6.

For the comparison of two methods (LIS and LT), the ratio R of the photo-ion current to the thermal ionization background has been measured for two types of the target system: the first one was a traditional construction (target connected to the ion source) [8] and the second one was the laser target. In Table 3 the

beam intensities of ^{145m}Gd and ^{145g}Gd from both tested target systems at the equal temperature conditions are presented. During the tests the targets having an identical material thickness were used, which were irradiated in both experiments by the same proton beam intensity. Also we were trying to keep the same temperature conditions for the tested targets and the ion source. The temperature was $(2500 \pm 50)^\circ\text{C}$ that ensured a rather fast escape of Gd radioactive atoms for which the effusion is considered to be the main delay dominating process. In spite of similar conditions of radioactive Gd production for both targets, we have obtained the ratio of ^{145m}Gd ($T_{1/2}=1.87$ min) to ^{145g}Gd ($T_{1/2}=23$ min) almost 7 times higher from the laser target than from the usual target-ion source unit (see Table 3 “laser off”). The enhancement of ^{145m}Gd having a considerably shorter half-life than a long-lived ^{145g}Gd demonstrates that the integrated target-ion source is faster than the usual target-ion source unit.

Table 3

Beam intensities of ^{145m}Gd and ^{145g}Gd produced by different target-ion source units at a temperature of 2500°C

Type of target-source unit used	^{145m}Gd beam intensity, s^{-1}		^{145g}Gd beam intensity, s^{-1}		Ratio $^{145m}\text{Gd}/^{145g}\text{Gd}$	
	Target with ion source	Laser target	Target with ion source	Laser target	Target with ion source	Laser target
Laser at resonance	$1.64(8)\times 10^5$	$3.21(11)\times 10^5$				
Laser off	$1.55(6)\times 10^5$	$2.30(8)\times 10^5$	$2.02(20)\times 10^6$	$4.40(16)\times 10^5$	$7.7(1.1)\times 10^{-2}$	$5.20(37)\times 10^{-1}$
R	0.06(6)	0.40(6)				

3.4. The uranium carbide CTIS for the production of neutron-rich isotopes

A schematic drawing of the CTIS for the production of nuclides with high ionization potentials is shown in Fig. 7. The electron beam was introduced into the target volume by a cathode shaped for that purpose and placed to the side of the extraction electrode. So the electron beam ionization took place inside the target container [3]. The yields of neutron-rich Ag and Sn isotopes are shown in Fig. 8. The production efficiency values obtained as a ratio of measured and calculated yields are, correspondingly, 4% and 2% for long-lived Ag and Sn. With a high value of probability it is equal to the ionization efficiency of that species, as the release times of these elements are shorter than their lifetimes.

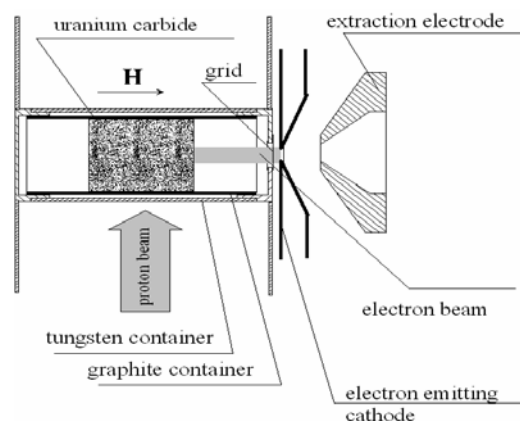


Fig. 7. Scheme of the electron beam ionizing UC target for production of neutron-rich isotopes

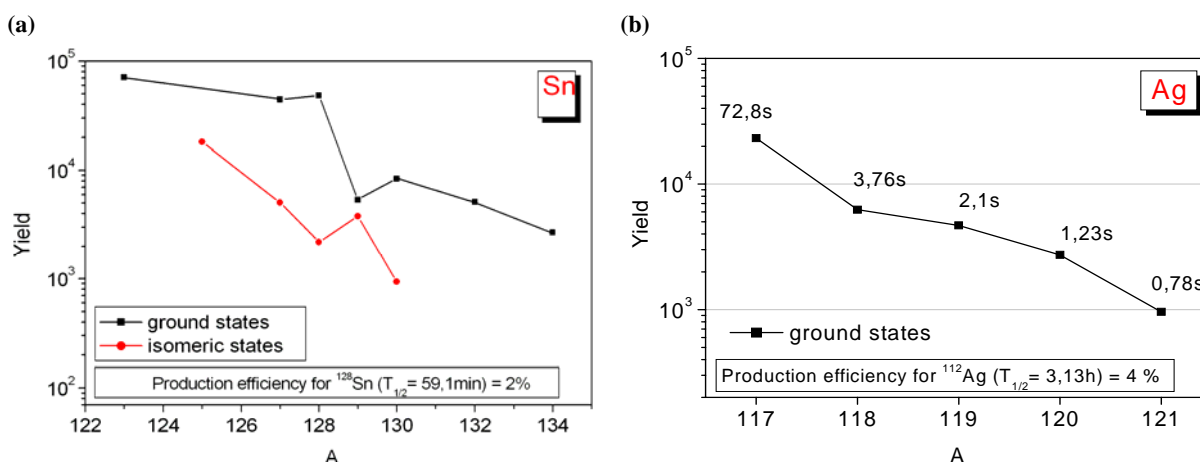


Fig. 8. Sn (a) and Ag (b) isotope yields from the electron beam IT

4. Conclusion

The yields of on-line mass-separated Cs, Rb and Fr isotopes have been studied at the IRIS. Properties of high density UC targets, in form of rod and powder, and a low density UC_x target prepared by the ISOLDE method similar to the PARRNe target are compared. According to the measured yield trends, the release efficiency of an ISOLDE like target for short-lived Cs isotopes is 1.5–2 times higher than that of a HDR (high density rod) uranium carbide target which was studied at the IRIS initially. It is rather encouraging result, as the grain size of the HDR UC target was ten times larger than the ISOLDE like target.

It should be pointed out that the on-line measured production efficiency and release properties of the ISOLDE like target specially prepared at the IRIS for that comparison tests coincide with the ISOLDE original target within the experimental errors ($\leq 40\%$).

To compare target materials having different densities but a similar dispersivity, a new developed, high density pill (HDP) UC target with the grain size of 20 μm have been on-line investigated. According to the measured Cs yield trends, the release efficiency of the new HDP target coincides with the ISOLDE like target within the limits of the measurement errors.

The comparison of the yields of short-lived Fr isotopes from the HDR and HDP targets with the yields from the ISOLDE graphite-cloth target exhibits a rather unexpected result: the normalized yields of extremely short-lived Fr isotopes from high density targets are equal or even higher than those from the graphite-cloth target.

Off- and on-line tests of ionizing targets have demonstrated that they can be used for the on-line production of a large set of nuclides using surface and resonance laser ionization. The ionization efficiency measured off-line for surface and laser ionized different species is comparable with those published in the literature. A low ionization efficiency value for Li can be explained by a low temperature of the ionizing target. To ensure a higher Li ionization efficiency, a target temperature should be at least 2200°C or even higher. The ionization efficiency for the tested elements can be increased in our construction almost by a factor of two by decreasing the diameter of the hole for the beam from 2 to 1 mm, as the laser beam diameter is about 0.5 mm.

As it is seen in Table 2, the target can be successfully used for the production of neutron-deficient isotopes of all rare-earth elements. The ionization efficiency may be higher about 3 times, if the ionizing target is used only in a surface ionization mode when the hole for the laser beam introduction is eliminated.

References

1. V.N. Panteleev *et al.*, Rev. Sci. Instr. **73**, 738 (2002).
2. V.N. Panteleev *et al.*, Nucl. Phys. A **701**, 470c (2002).
3. V.N. Panteleev *et al.*, Rev. Sci. Instr. **77**, 03A705(2006).
4. A. Andrighetto, A.E. Barzakh *et al.*, Eur. Phys. J. A **19**, 341(2004).
5. A. Andrighetto, A.E. Barzakh *et al.*, Eur. Phys. J. A **23**, 257 (2005).
6. V.N. Panteleev *et al.*, Eur. Phys. J. A **26**, 147 (2005).
7. A.E. Barzakh *et al.*, Phys. Rev. C **72**, 017301 (2005).
8. A.E. Barzakh *et al.*, Phys. Rev. C **61**, 034304 (2000).

INVESTIGATION OF BORONIZATION IN GLOBUS-M TOKAMAK AND GAS-FILLED DETECTORS USING THE ELECTROSTATIC ACCELERATOR BEAMS

V.M. Lebedev, A.G. Krivshich, V.A. Smolin, B.B. Tokarev, E.I. Terukov¹⁾, V.K. Gusev¹⁾

¹⁾ *Ioffe Physical-Technical Institute of RAS, St.-Petersburg*

At PNPI there is a Van de Graaf electrostatic accelerator with the energy of 1.5 MeV. The accelerator was used for a wide program of fundamental research (nuclear physics, physics of solids, films and surface semiconductors) as well as for technical and applied investigations (new materials, nuclear detectors, physical installations). At this accelerator the nuclear physics techniques of material research are used. They include a Rutherford backscattering spectrometry and a nuclear reaction analysis [1]. These techniques are nondestructive, high sensitive and precise.

The main results of investigations at this accelerator for past 5 years are presented in this article. They include:

- study of vacuum vessel boronization in Globus-M Tokamak,
- aging investigations (using nuclear microanalysis) of gas-filled particle detectors proposed for experiments at the Large Hadron Collider (LHC).

1. Study of vacuum vessel boronization in Globus-M Tokamak

1.1. Introduction

At Ioffe Physical-Technical Institute of RAS there is Globus-M Tokamak. Globus-M is a spherical small aspect ratio A tokamak (plasma major radius $R = 0.36$ m, minor radius $a = 0.24$ m, $A = R/a = 1.5$, toroidal magnetic field 0.1–0.6 T, plasma current up to 0.36 MA) presently operating in Ohmic heating regime [2, 3]. The first experiments were performed in the vacuum vessel with stainless steel limiters. Later on the vessel inner cylinder and partly the poloidal limiters were protected with graphite tiles.

The effective way to reduce the impurity contamination in tokamak plasma is the coating of the first wall with boron-carbon films. In the Globus-M experiment the boron-carbon film was deposited on the vacuum vessel inner surface in glow discharge (GD) in the mixture of helium and carboran $C_2B_{10}H_{12}$. The essential advantages of this method are the low cost and the simplicity of implementation. The carboran is the non-toxic and non-explosive substance. It is a powder at the room temperature, which is intensively evaporated at the temperature higher than 40°C.

The first boronization of the vacuum vessel was performed at a low percentage of carboran. The carboran vapor pressure was less than 10% of He pressure in glow discharge applied during 30 minutes. However, this procedure led to significant reduction of hydrogen recycling and to 20% increase of plasma current at the same loop voltage waveform. Then the Boron/Carbon films were deposited on the substrates from different materials in a high frequency glow discharge out of the Globus-M vacuum vessel and their properties were studied in details. The last boronization in the Globus-M was carried out at the essentially lower helium to carboran vapor pressure ratio in the range 3/1 – 5/1. After the boronization the analysis of the spatial distribution and the structure of the deposited film have been undertaken. For this purpose silicon probes (plates of approximately 1 cm² area) were placed in 16 points on the vessel inner surface and the graphite limiters.

1.2. Experiment

The Globus-M vacuum vessel is an all-welded stainless steel construction of ~ 1 m³ inner volume. The vessel plan view is shown in Fig. 1, the contour of the vertical cross-section is depicted in Fig. 2. Figures 1–2 show also the position of silicon plates located in four sections along the torus.

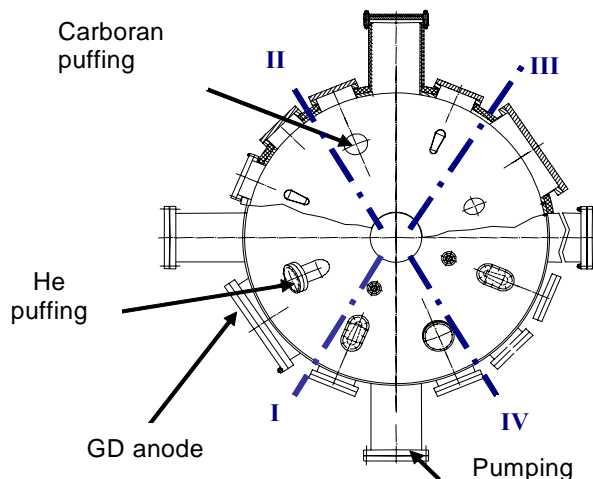


Fig. 1. Vacuum vessel plan view showing position of He and carboran puffing and CD electrode. I, II, III, IV – sections for silicon plates positioning

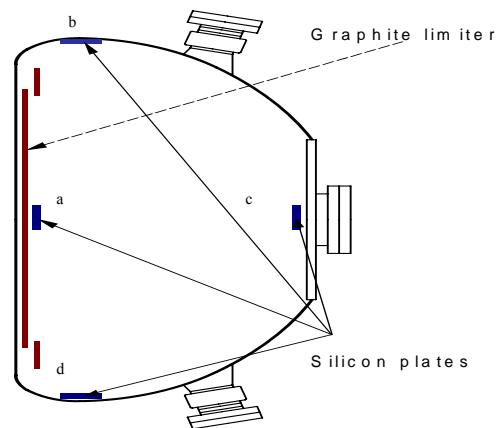


Fig. 2. Vacuum vessel cross-section showing the position of silicon plates and graphite limiter

The routine procedure of the vessel conditioning includes the bake-out at the temperature up to 200°C and the glow discharge cleaning in hydrogen and noble gases. The glow discharge voltage is applied between the single electrode (anode) and the earthed vessel. The electrode of 20 mm diameter is positioned in the tokamak middle plane (see Fig. 1). The parameters of the vessel and the glow discharge characteristics are shown in Table 1. The helium pressure was provided by the piezoelectric valve. The carboran was evaporated by heating the ampoule containing the carboran powder. The steady state temperature of 45°–48°C was sufficient to sustain the required pressure.

Table 1

The vessel parameters and glow discharge characteristics of the Globus-M Tokamak

Diameter of outer wall	1260 mm	Glow discharge voltage	300 V
Diameter of graphite limiter	252 mm	Current density	30 $\mu\text{A}/\text{cm}^2$
Vertical axis of torus	1.094 m	Gas pressure	0.2 Pa
Vessel volume	1.05 m ³	He to carboran pressure ratio	3/1 – 5/1
Inner surface area	5.7 m ²		

1.3. Results

First detailed study of carboran film properties was performed for the films deposited on the silicon, quartz and glass plates in 40 MHz He or Ar glow discharge in a small laboratory device (the distance between electrodes was 35 mm). The basic results can be summarized as follows.

The deposition rate decreased when the substrate temperature rose in the range of 20°–100°C. The films had the amorphous structure.

The Boron/Carbon ratio was determined from the nuclear reactions analysis (NRA) with deuterons. Figure 3 shows the energy spectra of protons and α -particles originated in the reactions of 1 MeV deuterons with nuclei of carbon and boron isotopes. The B/C ratio in the deposited films was determined by integrating the peaks of $^{10}\text{B}(d,\alpha)^8\text{Be}$ and $^{12}\text{C}(d,p)^{13}\text{C}$ reactions [2, 3] and appeared to be about 48/52 in percents.

The content of hydrogen (result of infra-red spectrum analysis) reached 40–50% at the room temperature and could be reduced by annealing at a higher temperature.

The characteristic values of the specific resistance is equal approximately to 10^6 Ohm·cm at the room temperature and $\sim 10^5$ Ohm·cm at the temperature of 100°C. The films are transparent in the visible range. After the vessel boronization with a small fraction of carboran vapor pressure (less than 10% of He pressure)

the subsequent analysis of silicon plates revealed a formation of thin films with a typical thickness of 100 Å. The film had an amorphous structure, but the content of boron did not exceed 4%. After 200 plasma shots with the plasma current of 150 kA accompanied by routine glow discharge cleaning in helium during 70 hours the amorphous structure transformed to the diamond-like one. It is remarkable that the hydrogen in the film was practically absent.

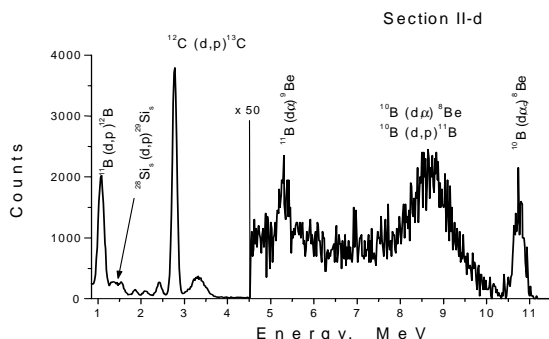


Fig. 3. Energy spectrum of protons and α -particles originated in the reactions of 1 MeV deuteron beam with carbon and boron isotopes in the deposited film. Angle of observation is 135° relatively to the beam

More detailed analysis was undertaken after the boronization with the ratio of helium to carboran pressure in the range 3/1 – 5/1 during 1.5 hour. The boronization was followed by a short experimental series from 80 plasma shots with plasma current of 200 kA and 12 hours of glow discharge cleaning in helium. The distribution of the film thickness deposited on silicon plates in different points of the vessel is shown in Table 2. The plates numbering is given according to Figs. 1–2.

The film composition in the cross-section II (Fig. 1) was studied by means of nuclear reaction analysis (NRA) and Rutherford backscattering spectrometry (RBS) at the PNPI electrostatic accelerator. The content of iron was obtained from the RBS spectrum of deuterons. These results are presented in Table 3.

Table 2

Film thickness on silicon plates in the Globus-M Tokamak				
Film thickness, μm				
Position	a	b	c	d
I	-	1	0.5	0.4
II	0.03	0.65	0.1	0.3
III	-	0.3	0.3	0.3
IV	-	0.3	1.2	0.4

Table 3

Film composition in cross-section II of the Globus-M Tokamak	
Substrate	Composition of film
II-a	$\text{B}_{0.32 \pm 0.02} \text{C}_{0.52} \text{Fe}_{0.16}$
II-b	$\text{B}_{0.01} \text{C}_{0.52 \pm 0.02} \text{Fe}_{0.43}$
II-c	$\text{B}_{0.27 \pm 0.02} \text{C}_{0.55} \text{Fe}_{0.18}$
II-d	$\text{B}_{0.43 \pm 0.02} \text{C}_{0.47} \text{Fe}_{0.10}$

1.4. Conclusion

The described procedure of Globus-M vessel boronization leads to a formation of the amorphous boron-carbon film with a typical B/C ratio of 3/4–3/5. The film thickness varies within a factor of 4 along the vessel surface. No obvious correlation between the film thickness and the position of the glow discharge electrode and the gas puffing ports was observed. The physical properties of the B-C coating deposited in DC glow discharge on the vessel surface are similar to properties of the films obtained in 40 MHz discharge. The appearance of iron in the film structure can be explained by a sputtering of the vessel material during boronization and the tokamak routine operation. Thinner films have a lower content of boron. The tokamak operation (plasma shots and routine glow discharge cleaning) leads to a significant reduction of hydrogen content in the boron-carbon films.

2. Aging investigations of gas-filled particle detectors by means of Nuclear Reaction Analysis

2.1. Introduction

Some time ago it was demonstrated that the method of Nuclear Reaction Analysis (NRA) is very effective for investigation of the aging effects in the gas-filled detectors [4–6] operated under high accumulated dose. This technique is particularly efficient in quantitative evaluation of the light elements (oxygen, carbon, nitrogen, fluorine, *etc.*) presence in the gold coating of the anode wire. The NRA method is also adequate for determining light element distribution with a depth measurement over a range of more than 1 μm .

Such data are especially important in studies of gas discharge avalanche plasmas because they are a starting point for most of the aging processes in the gas filled detectors. Wire aging is an extremely complex chemical process. To obtain a general picture of wire aging, it is necessary to identify the dominant processes occurring in gas avalanches, which result in the production of active chemical species (radicals, ions, *etc.*). The avalanche environment is plasma of ions and neutral radicals, and thus the wire aging process should be studied in the framework of plasma chemistry. The most important plasma-chemical reactions for the gas mixtures ($\text{Ar}/\text{CO}_2/\text{CF}_4$ and $\text{Xe}/\text{CO}_2/\text{CF}_4$) produce many different active species including oxygen and fluorine [4–7].

Application of the NRA method in our aging investigations gave us a reliable confirmation of the oxygen key role in the wire-swelling mechanism and demonstrated the kinetics of oxygen transport into the depth of the gold coating of the anode tungsten wire [5–7]. Active elements, including radicals, penetrate through the already opened cracks in the gold layer and react directly with the wire tungsten. Finally, this causes a swelling of the tungsten in the wire and, as a consequence, forces break of the gold coating produced within the wire.

But initial imperfections in the gold crystallite structure, which can increase and develop under the influence of sustained irradiation and etching of the gold, can provide favorable conditions for active oxygen with broken bounds, and even for more complicated chemical radicals, to penetrate into the tungsten. Etching strongly attacks defects in the gold coating and results in its extension. It should be noted that etching is a dangerous process which can open a direct path for the active oxygen to the tungsten surface of the wire. Special interest for our gas mixture are two chemical agents which determine possible gold etching: fluorine and xenon-fluorine XeF_n ($n = 2, 4, 6$) compounds. These agents are strong oxidizers and may interact with the gold causing etching. So, in order to understand the aging (including the wire swelling) mechanism in more detail, it was principally important to develop the NRA method for investigation of fluorine distribution in the anode wires. In case of success we would get the method allowing to perform the detection and quantitative evaluation of all light elements (oxygen, carbon, fluorine, nitrogen) which are coming from gas mixtures used in gaseous detectors and concentrated in electrodes.

2.2. NRA technique

For the detection and quantitative evaluation of the fluorine content as a function of depth in the gold, the nuclear reaction $^{19}\text{F}(p,\alpha)^{16}\text{O}$ has been applied [5, 8]. The reaction is exothermic and thus the exiting α -particles have higher energies ($E_\alpha = 7$ MeV) in compare with the incoming protons ($E_p = 1.25$ MeV) which are scattered on the target. This allows us to absorb completely the beam ions with a few microns of aluminum foil placed in front of the semiconductor detector, which is used for detection of the final state particles. Due to the Coulomb barrier the energy of the bombarding protons is not sufficient for nuclear interaction with higher atomic number elements (such as Al, Au, W). Hence, the α -particles produced in the interaction with fluorine atoms are detected practically without background.

The NRA was carried out at the PNPI electrostatic accelerator. The frame with investigated wire was fastened to the target apparatus of a vacuum chamber. A proton beam of 1.25 MeV was used. The diameter of the beam spot on the wire was about 4 mm. The beam current through the wire was about 3–5 nA. The heat consumption of the irradiated wire was 0.01–0.02 W/cm. The number of protons, which passed the wire, was evaluated with the current integrator. α -particles were detected by a surface-barrier Si(Au) detector positioned at an angle of $\theta = 135^\circ$ relatively to the beam axis.

To measure the distribution of fluorine along the wire the target was scanned with the beam. The method is based on the analysis of the energy spectra of emitted particles and makes it possible to determine a light element concentration profile. Schematics and nomenclature for the (p,α) nuclear reaction process in a sample-target and the reconstruction of the resulting energy spectrum are presented in Fig. 4. The energy spectrum of the α -particles produced by the (p,α) -reactions at a constant energy of protons was measured using a semiconductor detector. Back-scattered protons are filtered out using a thin (6 mg/cm^2) aluminum foil.

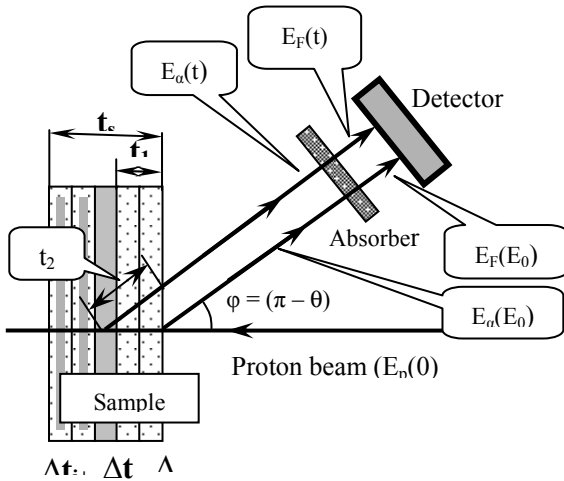


Fig. 4. Schematics and nomenclature for the (p,α) nuclear reaction process in sample

The energy of the detected α -particle resulting from the reactions at a depth t depends on the relation between the beam particle energy and the path traveled by the emitted particles. A reaction, which takes place near the surface of the specimen, will yield α -particles with higher energy than a reaction which occurs at a greater depth.

The *energy-depth* relation may be deduced from the fact that the measured energy of α -particle produced at the depth t depends on the energy loss of protons reaching the depth t and the energy loss of α -particle in the

traversing the sample before it reaches the detector. To calculate this relation, a sample is sliced on thin layers with the thickness of Δt_i (Fig. 4). The energy of protons $E_p(t)$ with incident energy $E_p(0)$ at the depth t_1 is given by the equation:

$$E_p(t) = E_p(0) - \int_0^{t_1} |S_p(t)| dt,$$

where $S_p(t)$ is a stopping power of substance for protons, t_1 is a path length of protons in the target.

The energy $E_\alpha(E_p)$ of α -particle resulting from a reaction (p,α) is given by the well-known expression:

$$E_\alpha(E_p(t)) = M_\alpha M_p E_p \{ 2\cos^2\theta + B + 2\cos\theta [\cos^2\theta + B]^{1/2} \} / (M + M_\alpha)^2,$$

where θ is the angle between the beam direction and the detector direction; M_p , M_α , M – the masses of incident particle, outgoing particle and final nucleus; $B = M(M + M_\alpha)(Q_R/E_p - M_p/M + 1)/(M_\alpha M_p)$.

The energy of α -particle in the detector $E_F(t)$ is given by the equation below:

$$E_F(t) = E_\alpha(E_p(t)) - \int_0^{t_2} |S_\alpha(t)| dt - \int_0^{t_{Al}} |S_\alpha(t_{Al})| dt,$$

where $S_\alpha(t)$ is the stopping power of substance for α -particles; $t_2 = t_1/\cos\theta$ is the path length of α -particles in the target; t_{Al} is the thickness of the aluminum foil-absorber.

Using tabulated stopping power data, the $E_F(t)$ dependence can be calculated from these equations. This approximation appears to be quite reasonable if we take into account that the energy loss of particles is relatively small compared with their initial energy and the stopping powers have a linear dependence on the energy and vary less than 15% over the relevant energy ranges: 1.0–1.25 MeV for protons, 4.0–7.0 MeV for α -particles [4, 8]. In this case the energy scale can be converted into a linear depth scale:

$$E_F(t) = E_F(E_0) - G_{NR} t,$$

where $G_{NR} = (\partial E_\alpha / \partial E_p) S_p + S_\alpha / \cos\theta$. G_{NR} is an effective energy loss related to single length. The G_{NR} depends on energy losses of α -particles and protons, reaction kinematics, geometry of experiment, and elemental composition of investigated sample. $G_{NR} = 380 \text{ keV/mg/cm}^2$ for an investigated wire.

As shown in Fig. 4, we sliced the investigated sample per thin layers to provide the calculation. The thickness Δt_i connects with energy interval ΔE_i of experimental spectrum by equation $\Delta t_i = \Delta E_i / G_{NR}$.

The energy spectrum $Y(E_F)$ of the detected α -particles is given by the equation:

$$Y(E_F(t)) dE_F = C(t) \cdot I \cdot \sigma(E_p(t)) \cdot \Delta\Omega \cdot dt,$$

where $C(t)$ is the concentration profile of fluorine, *i.e.* the number of element atoms per cm^3 at the depth t ; I is the number of incident particles; $\sigma(E_p(t))$ is the differential cross section for the angle θ ; $\Delta\Omega$ is the solid angle of a particle detection.

The sensitivity of NRA technique for the fluorine concentration measurements is about 1×10^{16} at/cm². An accuracy of the element concentration measurements is better than 5%. The thickness of the investigated layer depends on the range of particles in a sample (for protons and α -particles) and in the absorber (for α -particles). The available thickness of the gold or tungsten, which may be obtained from calculations, does not exceed 2–4 μm .

2.3. Results

The results obtained by the NRA analysis for different points along the wire are shown in Figs. 5-6. The fluorine concentration along the anode wire and their depth distributions have been measured for Ar(80%)+CO₂(10%)+CF₄(10%) gas mixture under the total accumulated charge up to 1.8 C/cm. Diameter of the gold plated wire is equal to 35 μm . The degradation test of the straw drift-tube (ATLAS TRT) was carried out using a 2 Ci ⁹⁰Sr β -source.

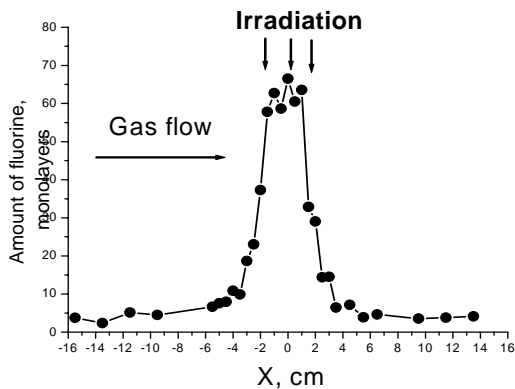


Fig. 5. The distribution of fluorine content along the irradiated wire. The element content of 1 monolayer is equal to 10^{15} at/cm²

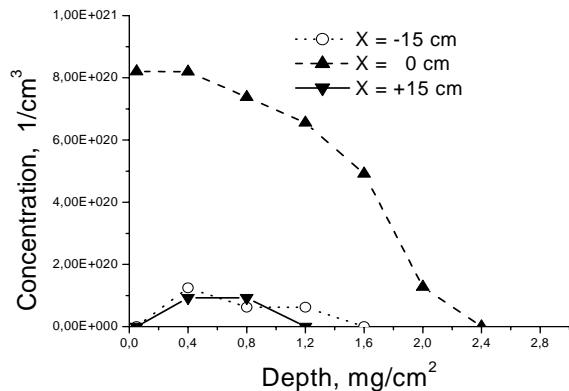


Fig. 6. The distribution of fluorine concentration as a function of depth into gold layer for different points along the irradiated wire

As one can see, after irradiation of the wires the amount of fluorine is noticeably increases. In the center of the irradiated zone the total amount of fluorine collected in gold has increased up to 15 times in comparison to the non-irradiated wire. Moreover, the maximum value of the fluorine peak concentration increased up to 10 times, reaching a value of 8×10^{20} at/cm³. In irradiated places of the wire the depth of the fluorine penetration is up to 2.5 mg/cm^2 . There is a direct correlation between the distribution of fluorine, oxygen and carbon concentrations along the wire and the beam irradiation profile (Fig. 7 and Table 4). It is shown that the fluorine concentration profile is correlated with changes of the wire diameter (increasing in the irradiation zone) and a gas gain (decreasing in the irradiation zone). For the detection and quantitative evaluation of the oxygen and carbon content as a function of depth in gold, the following nuclear reactions with deuterons in the energy range of 0.7–1.1 MeV have been applied: $^{12}\text{C}(d,p)^{13}\text{C}$ and $^{16}\text{O}(d,p)^{17}\text{O}$ [4].

Table 4

Dependence of element content, anode wire diameter and gas gain for different points along the wire.
Center of irradiated area corresponds to $X=0$ cm. Total accumulated charge is about 1.8 C/cm

Distance along the straw	Content of elements in monolayers			Gas gain, relative units	Wire diameter, μm
	Fluorine	Oxygen	Carbon		
-15 cm	4-5	50	25	1	35
0 cm	70	600	270	0.74	36.2
+15 cm	5-6	70	35	1	35

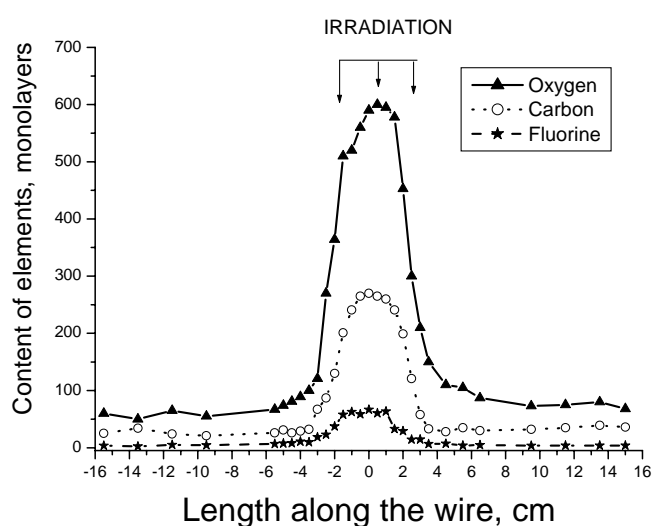


Fig. 7. The distribution of oxygen, carbon and fluorine content along the irradiated wire

2.4. Conclusion

The method of Nuclear Reaction Analysis (NRA) has been successfully developed at PNPI for investigation of the aging effects in the gas-filled detectors caused by fluorine and fluorine-containing compounds.

This method looks very promising and offers unique possibilities due to its high sensitivity, the fact that no etching is needed. The NRA method permits to investigate the lateral and depth distributions of the fluorine in samples.

Measurements of the oxygen, carbon and fluorine concentrations in the gold coating of the tungsten wire can provide an excellent method to compare the aging resistance of different wires which are intended to be used in the gas-filled detectors under high-accumulated dose.

References

1. V.M. Lebedev, V.A. Smolin and B.B. Tokarev, Preprint PNPI-2609, Gatchina, 2005. 24 p.
2. A.S. Ananiev, V.M. Lebedev, E.I. Terukov *et al.*, Semiconductors, **36**, 941 (2002).
3. N.V. Sakharov, V.K. Gusev, V.M. Lebedev, E.I. Terukov *et al.*, in *Proceedings of the 29th Conference on Plasma Physics and Controlled Fusion* (Montreux, Switzerland, 17 – 21 June 2002), p - 5.078 (2002).
4. G. Gavrilov, A. Krivshich and V. Lebedev, Nucl. Instr. Meth. A **515**, 108 (2003).
5. T. Ferguson, A. Krivshich, V. Lebedev *et al.*, Nucl. Instr. Meth., A **483**, 698 (2002).
6. T. Ferguson, A. Krivshich, V. Lebedev *et al.*, Nucl. Instr. Meth. A **515**, 266 (2003).
7. V.M. Lebedev, A.G. Krivshich and V.A. Smolin, Questions of Atomic Science and Technique, series: physics of nuclear reactors, **2**, 48 (2006).
8. V.M. Lebedev, A.G. Krivshich and A.N. Tatarinsev, Preprint PNPI-2616, Gatchina. 2005. 22 p.

COLLINEARITY LIMIT FOR THE MOVEMENT OF COMPLEMENTARY FRAGMENTS FROM THE SPONTANEOUS FISSION OF ^{252}Cf NUCLEI DETERMINED BY IMPLEMENTATION OF THE $(2E, 2V)$ -MEASUREMENT METHOD

M.N. Andronenko, B.L. Gorshkov, A.V. Kravtsov, I.A. Petrov, V.R. Reznik, G.E. Solyakin

1. Introduction

The $(2E, 2V)$ -measurement method was used for the study of mechanisms of nuclear disintegrations induced by relativistic projectiles. The account of this study is published in this issue [1]. The special attention was paid to collinear disintegrations induced in heavy and medium-heavy nuclei. The $(2E, 2V)$ -measurement method was realized at the proton beam of the PNPI synchrocyclotron in the form of an angle-velocity-energy correlation spectrometer (SAVEC) described in Ref. [1]. The time and energy calibrations of the SAVEC were performed with the use of a weightless source of ^{252}Cf . At the same time it was supposed that because of the two-body kinematics of the spontaneous decay of ^{252}Cf -nuclei complementary fission fragments should move on the straight line with the folding angle between the two fragments equal to 180° . Any deviation from 180° would have physical reasons. Our experimental practice showed that there is a necessity to check this assumption. Since two distinct experiments were carried out with fission fragments of the same ^{252}Cf -source one can compare collinearity for two different experimental conditions.

2. Different variants of mosaic constructions

Two massive complementary fission fragments were detected by the SAVEC which comprises a vacuum chamber with two time-of-flight tubes. In the end of each tube at the distance L a mosaic of N semiconductor silicon surface-barrier detectors (SSBSD) was located. Two mosaics of SSBSD in combination with the independent start signal device (SSD) made it possible to measure kinetic energies E_i and times of flight T_i for both ($i = 1, 2$) complementary fragments. So each of the registered events may be characterized by the collection of six measured parameters ($A_1, E_1, T_1; A_2, E_2, T_2$) related to the two detected fragments. Ordinal numbers of SSBSD in mosaics were denoted by A_1 and A_2 . When the kinetic energy E_i and time of flight T_i for each of the two complementary fragments are measured simultaneously, one can determine, unlike in $(2E)$ - or in $(2V)$ -measurement methods, fragment's absolute masses $M_i \sim E_i \cdot T_i^2$ and momenta $P_i \sim E_i \cdot T_i$. They may be used for the elimination of the distorted experimental events [1].

We want to describe two variants of the SAVEC construction which were implemented in experiments with fission fragments from the ^{252}Cf -source. They differ from each other by $L = 1060$ mm, $N = 33$ and $L = 688$ mm, $N = 8$. Both mosaic variants are shown in Figs. 1, 2. The first variant was used in experiments in which the maximum area of detecting elements was required. In this case among $33 \times 33 = 1089$ address combinations there were large variations for the folding angles between the two complementary fission fragments. For the second variant of the SAVEC construction, among $8 \times 8 = 64$ address combinations there were only 6 variations for the folding angles. This circumstance made angular measurements more effective. The binary code for the enumeration of detectors prevented the implementation of the variant with $9 \times 9 = 81$ address combinations which is shown in Fig. 3. For this case 6 variations for the folding angle detection are preserved. Figure 4 also shows a possible mosaic variant with $7 \times 7 = 49$ address combinations which have only 4 variations for the folding angle detection. Tables 1 and 2 contain all the information concerning values of difference $180 - \langle\theta\rangle$ in degrees for the $9 \times 9 = 81$ and $7 \times 7 = 49$ address combinations. In both cases $\langle\theta\rangle$ is an average folding angle for a certain address combination.

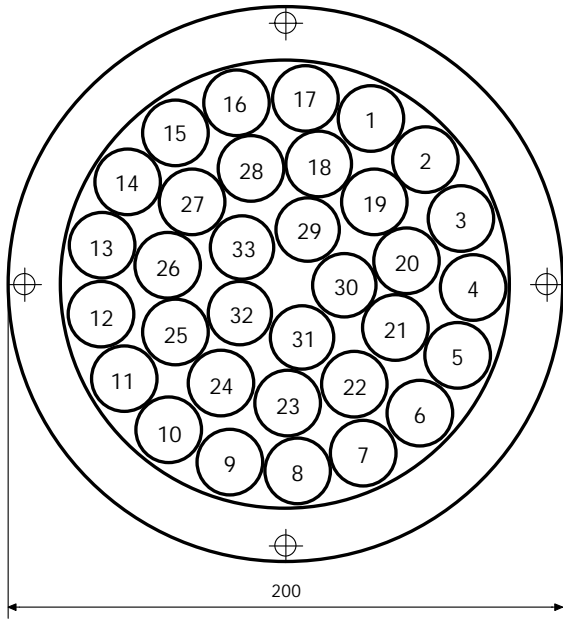


Fig. 1. Mosaic of the SAVEC construction with $N = 33$, $L = 1060$ mm

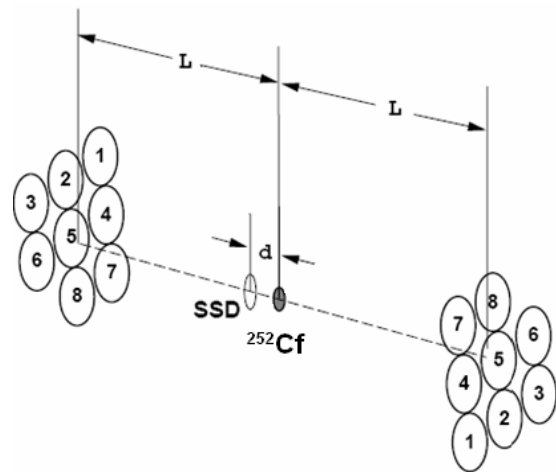


Fig. 2. Two mosaics of the SAVEC construction with $N = 8$, $L = 688$ mm. The distance between the ^{252}Cf -source and the start-signal device (SSD) $d = 37$ mm

Comparing mosaic constructions shown in Figs 2-4 one can conclude that they are almost equally effective for measurements of angular distributions. The chosen construction in Fig. 2 is nothing else but a truncated variant of $N = 9$ shown in Fig. 3.

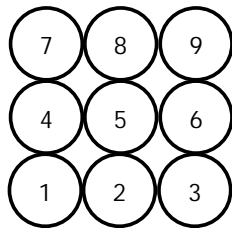


Fig. 3. Mosaic construction variant with $N = 9$

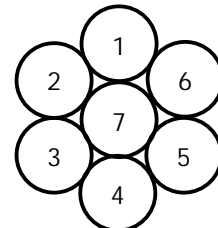


Fig. 4. Mosaic construction variant with $N = 7$

Table 1

	1	2	3	4	5	6	7	8	9
1	0	2.5	5.0	2.5	3.53	5.62	5.0	5.62	7.07
2	2.5	0	2.5	3.53	2.5	3.53	5.62	5.0	5.62
3	5.0	2.5	0	5.62	3.53	2.5	7.07	5.62	5.0
4	2.5	3.53	5.62	0	2.5	5.0	2.5	3.53	5.62
5	3.53	2.5	3.53	2.5	0	2.5	3.53	2.5	3.53
6	5.62	3.53	2.5	5.0	2.5	0	5.62	3.53	2.5
7	5.0	5.62	7.07	2.5	3.53	5.62	0	2.5	5.0
8	5.62	5.0	5.62	3.53	2.5	3.53	2.5	0	2.5
9	7.07	5.62	5.0	5.62	3.53	2.5	5.0	2.5	0

Table 2

	1	2	3	4	5	6	7
1	0	2.5	4.5	5.0	4.5	2.5	2.5
2	2.5	0	2.5	4.5	5.0	4.5	2.5
3	4.5	2.5	0	2.5	4.5	5.0	2.5
4	5.0	4.5	2.5	0	2.5	4.5	2.5
5	4.5	5.0	4.5	2.5	0	2.5	2.5
6	2.5	4.5	5.0	4.5	2.5	0	2.5
7	2.5	2.5	2.5	2.5	2.5	2.5	0

3. Experimental results

In the case of the SAVEC performance with $L = 1060$ mm, $N = 33$ and $33 \times 33 = 1089$ address combinations there were no detailed analysis on the angular distribution of the complementary fission fragments of ^{252}Cf nuclei. Since it was obtained at the level of 1.5% statistical accuracy, the value of the standard deviation of the total angular distribution from the collinearity $\sigma_\theta = 21$ mrad. Advantages of the $(2E, 2V)$ -measurement method were not utilized in this case for the further analysis. They were used in the second variant of the SAVEC performance with $L = 688$ mm, $N = 8$ and $8 \times 8 = 64$ address combinations. Owing to $(2E, 2V)$ -measurement method it was possible to obtain a bi-dimensional plot (P_1, P_2) for complementary fragments of spontaneous fission of ^{252}Cf nuclei. The plot shown in Fig. 5 contains all the events in which at least one of the momenta P_1 or P_2 was smaller than 4000 MeV/c, as well as a small part of the total statistics where both P_1 and P_2 were greater than 4000 MeV/c.

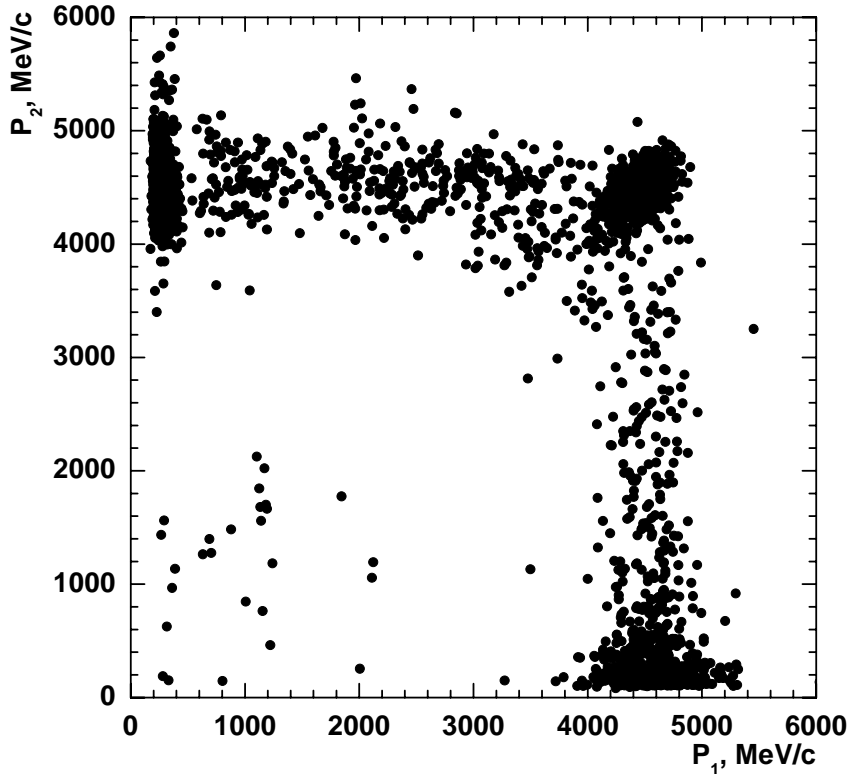


Fig. 5. Bi-dimensional plot P_2 versus P_1 for experimental events in which at least one of the momenta P_1 and P_2 is smaller than 4000 MeV/c as well as a small part ($\sim 0.5\%$) of the total statistics is used

Symmetric distribution of the events in Fig. 5 with respect to the diagonal $P_1 = P_2$ testifies the identity of both arms of the SAVEC. Events in which at least one of the momentum P_1 or P_2 was smaller than 4000 MeV/c comprised 1.3% of the total statistics. The events with clearly unbalanced momenta look like an evidence for the third body influence upon the two-body kinematics of the separating fragments. They can be considered as distorted events with respect to the normal fission events. One more advantage of the $(2E, 2V)$ -technique compared with other experimental methods is an opportunity to measure a missing mass

$$\Delta M = M_0 - (M_1 + M_2), \quad (1)$$

where M_0 is the mass of the target nucleus and $M_{1,2}$ are the masses of the detected fragments. Using the information measured by the SAVEC one can determine the masses M_1 and M_2 for each distorted event. It turned out that one of the masses M_1 or M_2 was normal, *i.e.* belonged to the light or heavy group of the fragments, the other one being much smaller, imitating a large missing mass. The normal mass had the

normal fragment momentum (*i. e.* it was larger than 4000 MeV/c), the smaller mass having much smaller momentum (less than 4000 MeV/c). The detailed analysis showed that among the distorted events, composed 0.4% of the total statistics, only 0.12% belonged to the fragments of the light mass group and 0.28% to the heavy mass group. This observation testifies that a considerable part of the distorted events represents the Rutherford scattering. Since in the calibration experiment with the ^{252}Cf -source the amplitude thresholds were very low, it was rather difficult to separate the effect of the Rutherford scattering from random coincidences for small momenta in both arms of the SAVEC. In Ref. [2] the presence – among the detected fragments – of the masses in the range from 55 to 65 u, characteristic for the natural mixture of nickel isotopes, was demonstrated. The distorted events differ from normal ones also by address combinations (A_1 , A_2) of the detectors hit by fragments. The number of non-collinear fragments is much larger for distorted events [3]. Thus the calibration experiment with registration of fragments of the spontaneous fission of ^{252}Cf nuclei by $(2E, 2V)$ -technique showed how to reject the distorted events. Figure 5 helps to eliminate all the distorted events. For this purpose elimination thresholds for $P_1 > 4000$ MeV/c and $P_2 > 4000$ MeV/c were chosen. The corresponding bi-dimensional plot (P_1, P_2) is shown in Fig. 6. The angular distribution for experimental events from Fig. 6 is demonstrated in Fig. 7.

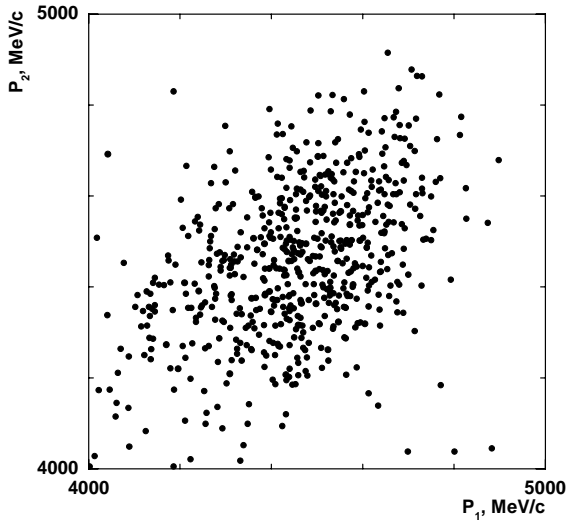


Fig. 6. Bi-dimensional plot (P_1, P_2) for events with momentum ranges 4000–5000 MeV/c

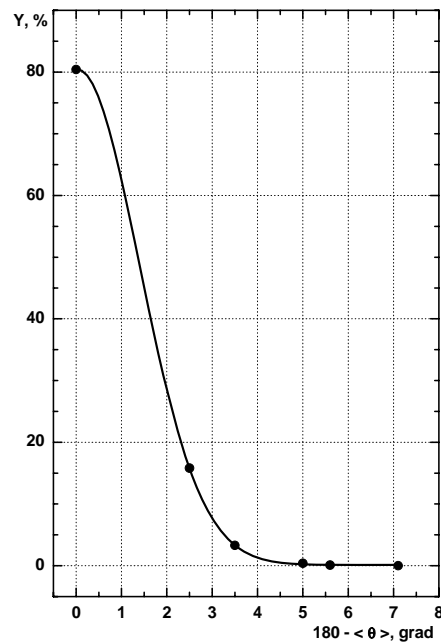


Fig. 7. Folding angle distribution for experimental events shown in Fig. 6

At the level of 4% statistical accuracy the spectrum shown in Fig. 7 satisfies to the standard deviation of the total angular distribution $\sigma_\theta = 19.2$ mrad. Later on two attempts were undertaken. At first the momentum thresholds for P_1 and P_2 were decreased to 3800 MeV/c and after that they were increased to 4200 MeV/c. In both cases values of the standard deviation for these angular distributions became larger than 19.2 mrad. Thus the value of $\sigma_\theta = 19.2$ mrad can be considered as a minimal possible standard deviation for angular distribution of complementary fragments from the ^{252}Cf -source measured with the help of the $(2E, 2V)$ -measurement method.

Returning to the experimental practice at the proton beam of the PNPI synchrocyclotron we can justify the division of experimental nuclear disintegration events in two groups according to the collinearity. The first group of events denoted by stars belongs to the folding angle interval of $(180^\circ - 177.5^\circ)$, the second group with events denoted by points belongs to the interval of $(176.5^\circ - 172.9^\circ)$. Fig. 8 shows two momentum distributions one of which is nothing else as a repetition of Fig. 6 for complementary fission fragments from the ^{252}Cf -source. The second distribution refers to the complementary fragments from disintegrations induced in tungsten nuclei by 1 GeV protons.

Experimental events for tungsten disintegrations were taken from Fig. 3 of Ref. [1]. All experimental events were denoted by stars and points in accordance with the value of the folding angle between complementary fragments.

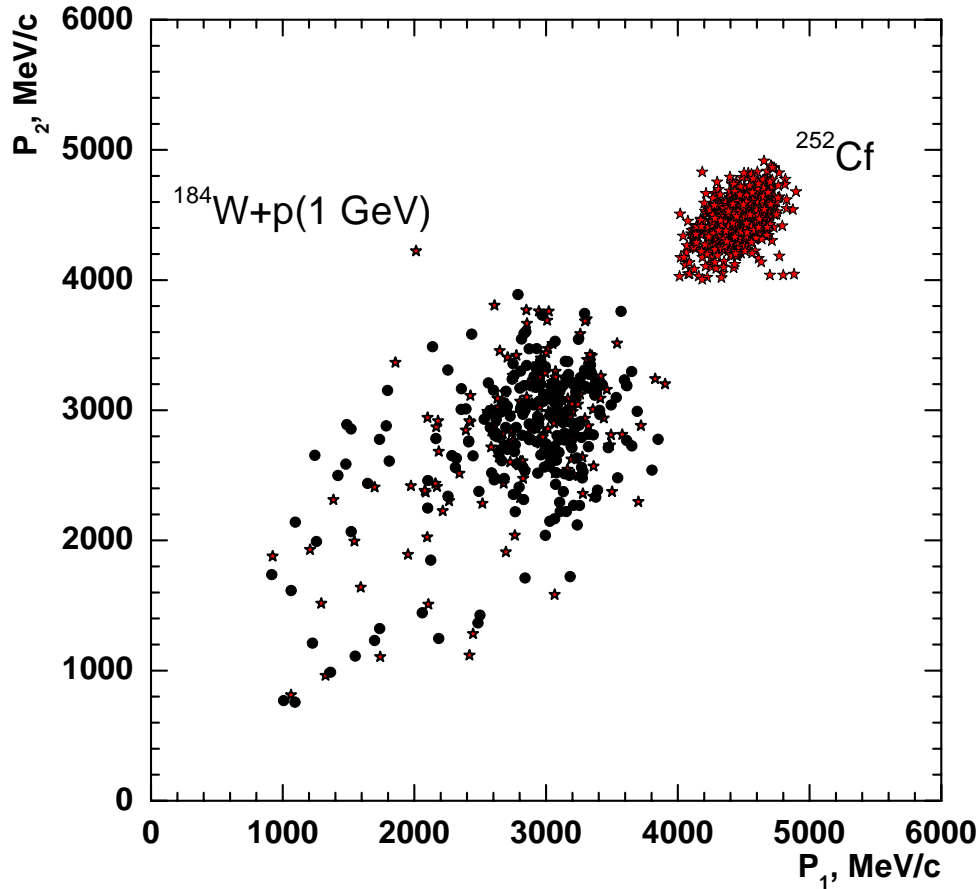


Fig. 8. Correlated momentum distributions (P_1, P_2) for complementary fragments from disintegrations induced in tungsten nuclei by 1 GeV protons and from the ^{252}Cf -source taken from Fig. 6. Stars and points are explained in the text

4. Conclusion

The value of $\sigma_\theta = 19.2$ mrad was obtained with detectors having angular acceptance $\delta\theta = 43.6$ mrad. It means that there is a possibility to get a better value for the measured standard deviation if one chooses detectors with a smaller angular acceptance. This limiting standard deviation can be evaluated according to the formula

$$\sigma_\theta^{\text{lim}} = \left[(\sigma_\theta)^2 - \frac{(\delta\theta)^2}{12} \right]^{1/2}. \quad (2)$$

Thus the final possible limiting standard deviation may be as low as $\sigma_\theta^{\text{lim}} = 14.5$ mrad.

References

1. B.L. Gorshkov, A.V. Kravtsov, V.R. Reznik and G.E. Solyakin, this issue, page 200.
2. A.V. Kravtsov and G.E. Solyakin, Phys. Rev. C **60**, 017601 (1999).
3. A.V. Kravtsov and G.E. Solyakin, in *Proceedings of the 1st International Workshop on Physics of Isomers* (St.-Petersburg, 18 – 21 June 2000), Sarov, VNIIF, 2001. p. 74.

RADIATION HARD PHOTODETECTORS BASED ON FINE-MESH PHOTOTUBES FOR CALORIMETRY IN VERY FORWARD RAPIDITY REGION

Yu.I. Gusev, V.N. Lukianov¹⁾, G.A. Mamaeva¹⁾, D.M. Seliverstov, L.P. Shusterman¹⁾

¹⁾ Central Research Institute Electron, St.-Petersburg

1. Introduction

In experiments using electromagnetic and hadron calorimeters, which are planned for the LHC in the very forward rapidity range (up to $\eta = 6$), the radiation fields are very high. Ionizing radiation levels reach hundreds of kGy and neutron fluences go up to 10^{16} n/cm². In addition the photo-readout systems have to operate in the magnetic fields of LHC Detectors (ATLAS, CMS), which in the region of interest are at the level of 20–40 mT, and in the presence of helium gas which exceeds the normal helium concentration in the atmosphere by a factor of 100 to 1000.

Low gain fine-mesh photomultiplier tubes (VPT, or vacuum phototriodes) have been used in the end-cap electromagnetic calorimeter of CMS and have been shown to be able to withstand gamma radiation doses up to 50 kGy. The VPT anode response decreased by 10% in good agreement with what would be expected due to a change of UV faceplate light transmittance [1, 2]. High gain photodetectors proposed to be used in the experiment CASTOR at LHC for the detection of Cherenkov radiation must provide stable operation for higher gamma radiation doses – up to hundreds of kGy and simultaneously for neutron fluences up to 10^{16} n/cm². A suitable detector for such applications can be a multi-stage fine-mesh photomultiplier tube (PMT) FEU-187 with highly radiation hard faceplate made of UV glass.

2. Measurements of PMT radiation hardness

For studies of faceplate radiation hardness, the best type of glass produced in Russia (US-49A) was chosen. This type of glass has a light transmittance loss $\Delta T/T_0 = 7\%$ at a wavelength of 425 nm for a radiation dose $D = 50$ kGy. This value corresponds to the average wavelength of the HLMP-DB25 LED used for PMT illumination. The irradiation of the faceplates was performed at the PNPI nuclear reactor with neutrons of average energy $E_n = 0.95$ MeV up to a total fluence of 10^{16} n/cm² known to an accuracy of 10%. The accompanied gamma radiation dose was estimated to be 1600 ± 250 kGy. The glass transmittance spectra measurements were done one month after the irradiation. We did not take into account the gamma radiation dose caused by the activation radiation of the glass, so the value 1600 kGy is a lower limit on the gamma radiation dose. The results of the reactor irradiation test are shown in Fig. 1.

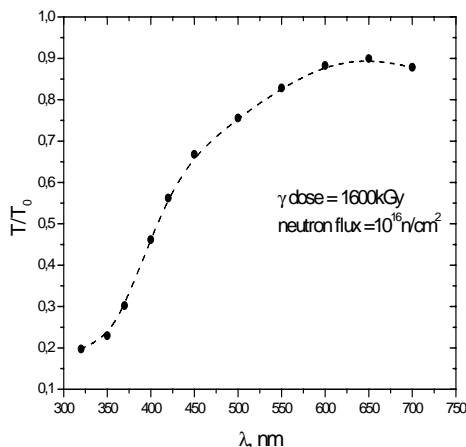


Fig. 1. US-49 relative glass transmittance after irradiation in nuclear reactor

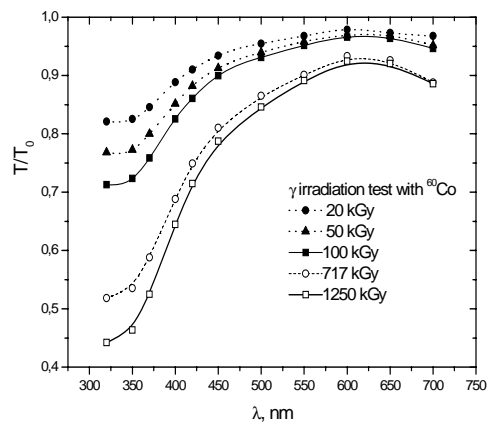


Fig. 2. US-49 relative glass transmittance for different of gamma radiation doses at ⁶⁰Co gamma facility

The total glass transmittance loss $\Delta T/T_0 = 1 - T/T_0$ can be estimated as a sum of terms due to gamma and neutron irradiation. For the wavelength of 450 nm $\Delta T/T_0 = 33\%$. In order to separate contributions of gamma and neutron irradiation to the value of T/T_0 we performed measurements of the light transmittance spectra for similar glass samples under the ^{60}Co γ -rays up to 1250 kGy at the PNPI gamma facility. Results are shown in Fig. 2. On the basis of the glass transmittance measurements with gamma radiation doses of 471, 717 and 1250 kGy we made a linear extrapolation to a dose of 1600 kGy. This allowed us to define at $\lambda = 450$ nm separate losses of $\Delta T/T_0 = 39\%$ for gamma irradiation and $\Delta T/T_0 = 15\%$ for neutron irradiation. This procedure can be done for a set of wavelengths in the range 325–600 nm. An example of the extrapolation for $\lambda = 450$ nm is shown in Fig. 3.

Using the extrapolation method discussed above, one can obtain the transmittance loss caused by a neutron fluence of 10^{16} n/cm² at any gamma radiation dose. The US-49A faceplate transmission after 10^{16} n/cm² and 50 kGy gamma irradiation is shown in Fig. 4. For comparison, the glass transmittance after only gamma irradiation up to 50 kGy is also shown. The accuracy of this method to separate the neutron and gamma damages in the PMT faceplate is estimated not to be better than 3%. The dependence of the faceplate light transmission change at different neutron fluences (F) can be obtained by performing measurements for varying F and gamma radiation doses. Such studies were not a goal of our experiment. We present only studies of the behavior of PMT windows in extremely hard neutron and gamma irradiation conditions.

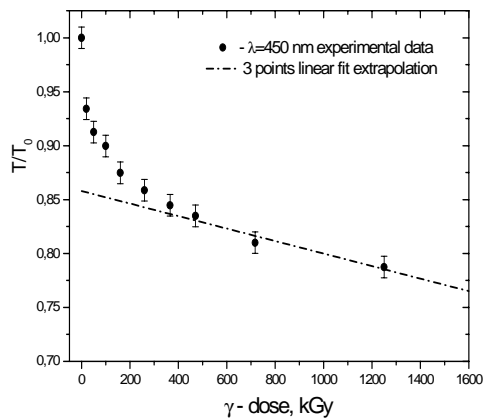


Fig. 3. The linear extrapolation of T/T_0 data at the different doses of ^{60}Co γ -irradiation

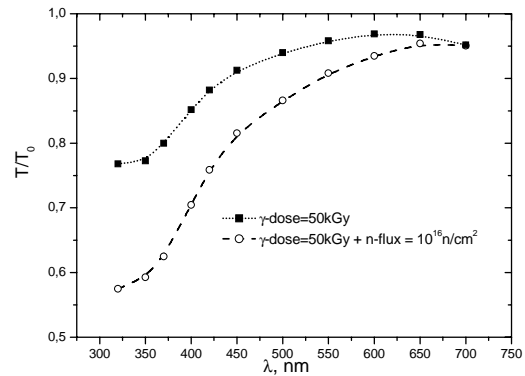


Fig. 4. Relative transmittance T/T_0 for a γ -dose of 50 kGy and neutron irradiation with fluence of 10^{16} n/cm²

As it was mentioned above, the VPT anode response is following the rather small glass transmittance change under gamma irradiation up to 50 kGy. The same insensitivity of the VPT anode response to 14 MeV neutrons with fluences up to 2.8×10^{14} n/cm² was shown in Ref. [2]. With a knowledge of the US-49A transmittance change under gamma irradiation, we measured the anode response of FEU-187 photomultiplier tube before and after irradiation at 20 kGy and 50 kGy using a blue LED Lamp HLMP-DB25 with a wavelength peaking at $\lambda = 426$ nm with the method described in Ref. [3].

Examples of spectra obtained before and after gamma irradiation (50 kGy) of the PMT FEU-187 are shown in Fig. 5. The numeral “2” marks the PMT pulse spectrum. Similarly, “3” indicates the reference PMT pulse spectrum, and “1” – the ^{137}Cs γ -spectrum from the reference PMT with the same gain as for the measurements (a) and (b). Stability of the electronics and PMT gain was at the level of 1%. Overall statistical and systematic errors are estimated as not more than 3%. The results obtained during gamma irradiation at 50 kGy show good agreement of the anode signal change with the faceplate transmittance loss within experimental errors of $\pm 2\%$. A burn-in test of the PMT was in a similar way to the irradiation test, with the PMT illuminated by a light emitting diode producing an anode current of 200 nA for 50 hours. Measurements of the anode signal before and after the illumination did not show any change of the amplitude with an accuracy of $\pm 2\%$, which demonstrates the stability of this PMT under these conditions.

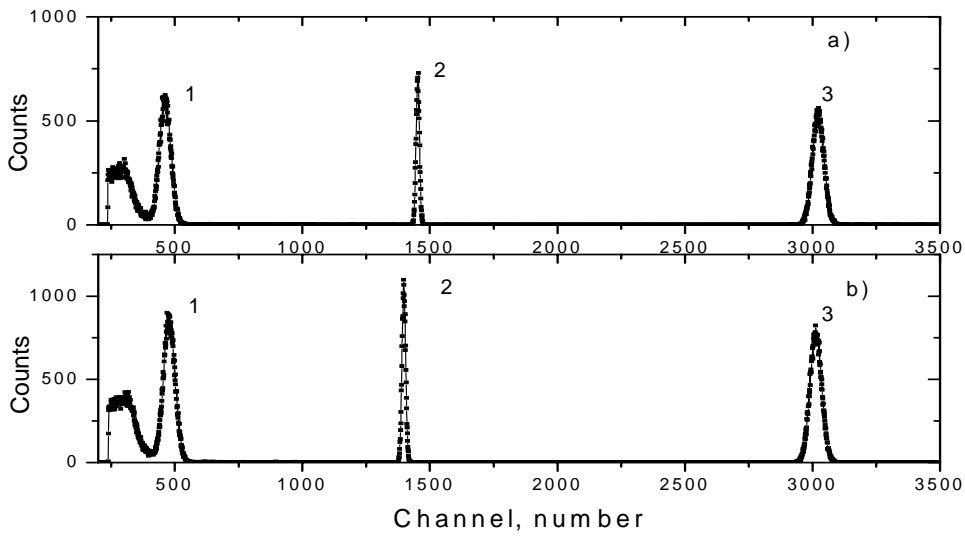


Fig. 5. Spectra from PMT FEU-187 before (a) and after (b) gamma irradiation up to 50 kGy

3. PMT immunity to the gaseous He

It is well known that helium gas can penetrate into PMT and degrade its performance increasing the dark count rate. Helium can also cause an ion pulse following a normal one. The presence of the gaseous He in the atmosphere of LHC Collision Hall and in the experimental pits is estimated to be between 100 and 1000 ppm. Immunity to the gaseous He is an important characteristic of photomultiplier tubes proposed for readouts in LHC environment. The helium immunity of the FEU-187 was measured using the experimental setup shown in Fig. 6. The PMT to be studied was placed into a vacuum-tight chamber. Dark current count rate and gain of PMT were measured in a constantly refreshed atmosphere of pure nitrogen during first 8 days. Later pure nitrogen was changed to a mixture of (N₂+He) where He admixture was 1600 ppm. The pressure in the chamber was equal to one atmosphere.

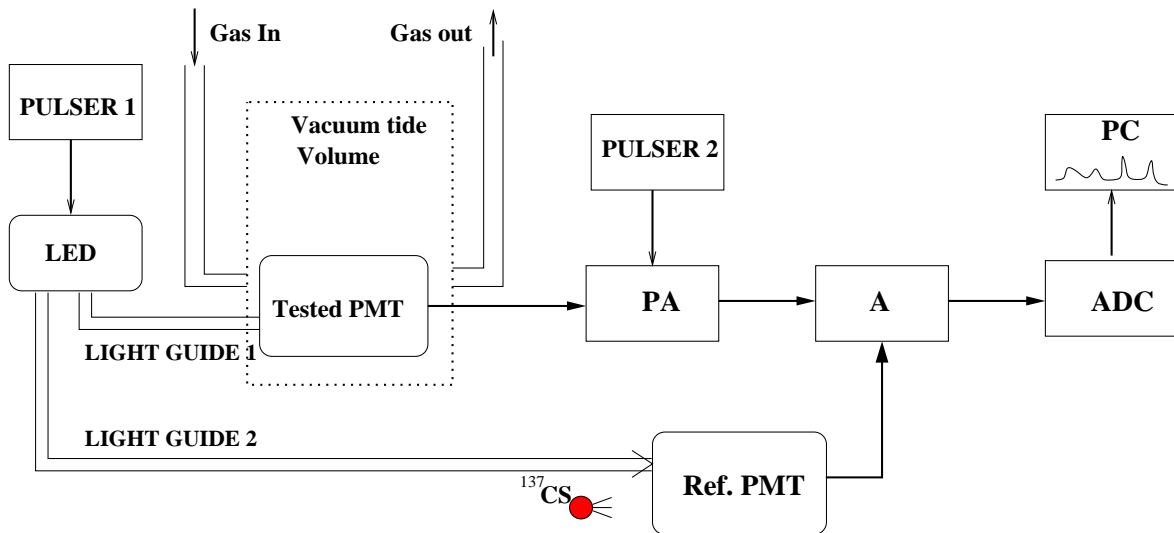


Fig. 6. Experimental setup for the He immunity test of PMT FEU-187

The PNT dark current without illumination was not more than 1 nA. The results of these measurements are shown in Fig. 7. The gain of the PMT was monitored during this test. Light pulses from the LED, driven by Pulser 1, were directed simultaneously by two fibers to the PMT under test and to a standard reference PMT placed outside of the He volume. The gain stability of the reference PMT coupled with NaI(Tl) crystal was tested by the detection of ^{137}Cs γ -rays during test measurements. The stability of electronics was tested by means of the precision amplitude signal generator (Pulser 2). All signals were digitized by an ADC and recorded with a PC. The dark noise count rate and the gain of PMT FEU-187 did not show any change during 4 weeks operation in an atmosphere of (N_2 +1600 ppm He).

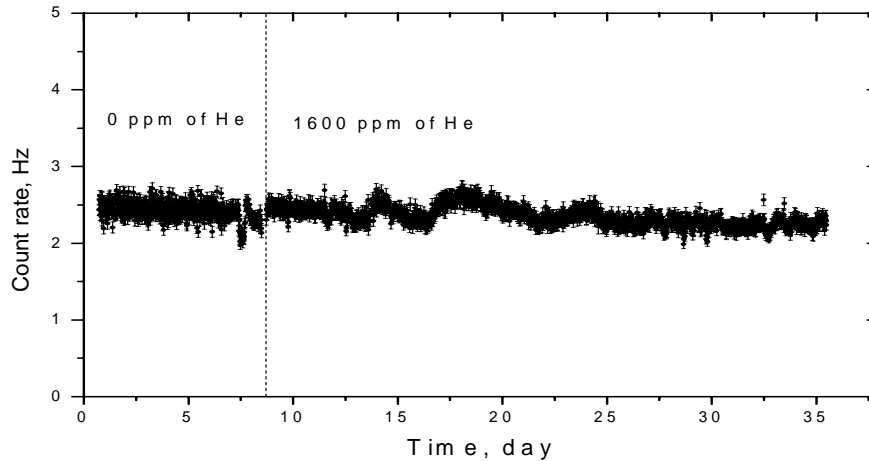


Fig. 7. Dark noise count rate in N_2 atmosphere with 1600 ppm of He admixture

4. Magnetic hardness and time resolution

Resistance to magnetic fields is an important issue for PMTs proposed to be used in the LHC environment. The gain dependence of the fine-mesh PMT FEU-187 on a magnetic field B was measured for two angles θ between the PMT axis and the magnetic field direction. The gain behavior over the large range of θ for $B = 40.6$ mT was also measured. Results of these measurements are shown in Fig. 8.

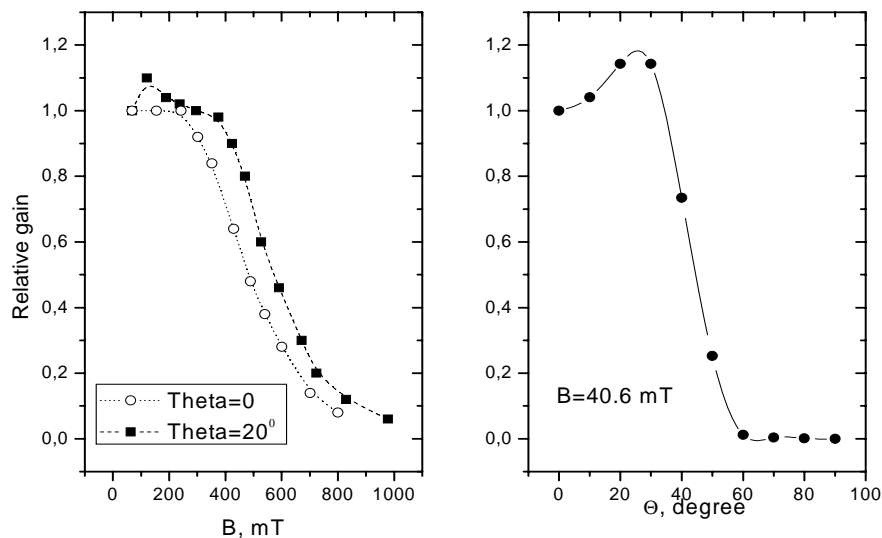


Fig. 8. Magnetic properties of fine-mesh FEU-187

Two different methods were used to evaluate time resolution of fine-mesh FEU-187.

1. Measurement of time of flight for different particles such as π , K and p with a momentum of $p = 1.8$ GeV/c, using two plastic scintillators (BS-420 with 2 cm thickness separated by 4 m). A time resolution of $\sigma = 58$ ps per photodetector was obtained.
2. Measurement with a pulsed light source with the pulse duration (FWHM) of 35 ps and the wavelength of 635 nm: with a threshold of about 0.2 photoelectrons, the measured time resolution was $\sigma = 270$ ps for a single photoelectron pulse (see Fig. 9).

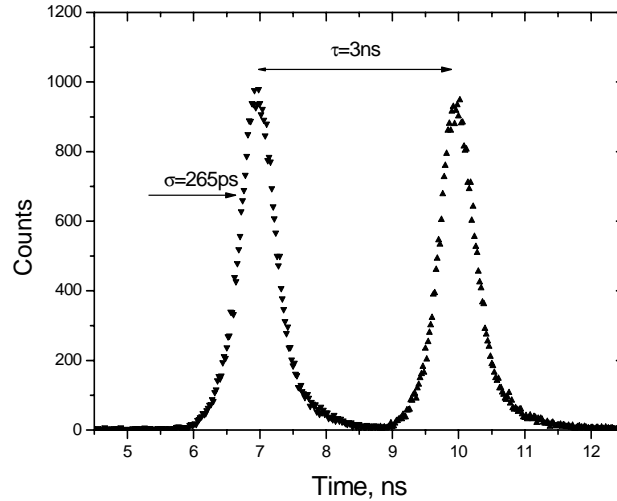


Fig. 9. Time resolution of FEU-187 measured in single photoelectron mode

5. Conclusion

In this paper we present the results of study of a very radiation hard photodetector – a high gain fine-mesh PMT (FEU-187) with a highly radiation hard faceplate from UV-transparent glass (type US-49A). Radiation resistance of PMT to γ -rays and neutrons was investigated at the PNPI gamma facility and nuclear reactor. A number of UV-transparent glasses were irradiated near active zone of reactor up to a fluence of 10^{16} n/cm² with an average neutron energy of $E = 0.95$ MeV and with gamma radiation doses of 1600 ± 250 kGy. In order to separate the light transmittance losses in the glass caused by neutron and gamma irradiation, the measurements of the glass transmittance spectra at different doses up to 1250 kGy were performed at the ⁶⁰Co gamma facility. In this way we were able to define the glass transmittance loss caused by the reactor radiation for the wavelength range $\lambda = 350$ – 650 nm separately for γ -rays and neutrons. For the wavelength $\lambda = 400$ nm, the light transmittance losses are equal to 43% and 11% due to gamma and neutron irradiation, respectively. In experiments with gamma irradiation to 100 kGy and neutron fluence of 10^{16} n/cm² the light transmittance at $\lambda = 400$ nm is reduced to 72% of its initial value. These results are an evidence of the high radiation hardness of the PMT faceplates that were studied. The irradiation of a PMT with US-49A faceplate by gamma radiation doses of 20–50 kGy has shown a change of the PMT anode response expected from the UV glass transmittance loss. Results of measurements of insensitivity to magnetic fields and immunity of the PMT against helium in the LHC environment are also presented.

At levels expected in the LHC environment, FEU-187 is radiation hard, resistant to magnetic fields and unaffected by the presence of helium. The PMT FEU-187 has an excellent time resolution of 58 ps measured by time-of-flight techniques with 1.8 GeV/c beams of pions, kaons and protons at CERN, and a time resolution of 270 ps measured with an ultrafast laser diode in a single photoelectron mode.

References

1. Yu. Blinnikov *et al.*, Nucl. Instr. Meth. A **504**, 228 (2003).
2. Yu. Gusev *et al.*, Nucl. Instr. Meth. A **535**, 511 (2004).
3. Yu. Gusev *et al.*, Preprint PNPI-2597, Gatchina, 2005. 16 p.

SYSTEM FOR DEEP PURIFICATION OF HYDROGEN IN MuCap EXPERIMENT

V.A. Ganzha, P.A. Kravtsov, V.A. Trofimov, G.N. Shapkin, A.A. Vasilyev, M.E. Vznuzdaev

1. Introduction

The MuCap experiment at PSI is a precision measurement of the rate Λ_S for the basic electroweak process of muon capture, $\mu^- + p \rightarrow n + \nu$. A measurement of 1% accuracy determines the last well-known of the nucleon charged current form factors, the induced pseudoscalar g_P , to 7%. The experiment is carried out at the $\pi E3$ muon beam of the 580 MeV proton accelerator at the Paul Scherrer Institute (PSI), Switzerland.

The capture rate is determined from a measurement of the disappearance rate $\lambda_- \approx \lambda_+ + \Lambda_S$ of negative muons in hydrogen and the world average of the free μ^+ decay rate λ_+ . Muons are stopped in a time projection chamber (TPC) with sensitive volume $15 \times 12 \times 30 \text{ cm}^3$ filled with ultrapure hydrogen at 10 bar. Electrons ionized by muons or other projectiles drift vertically in a homogeneous electrical field to the bottom of the TPC, where they are amplified with a multiwire proportional chamber (MWPC) and read out in two dimensions.

The experiment imposes strict and critical requirements on the hydrogen gas system supporting the active target – TPC detector. As the hydrogen gas density of the experiment of ten times higher than at standard temperature and pressure, the rates for muon transfer from μp to typical chemical impurities (N_2 , H_2O , O_2) are 3 orders of magnitudes larger than the muon decay rate. Once a muon has been transferred to a μZ atom, nuclear muon capture proceeds more than 100 times faster than on a μp atom. Thus, gas impurities distort the observed lifetime spectrum, and transfer must be suppressed by keeping the gas contaminations below a level of typically 10 ppb. Isotopic purity is required as well, since muon transfers to deuterium lead to a difficult diffusion problem. A dedicated isotope separation device [1] was constructed to produce protium with a deuterium contamination of less than 70 ppb; this work will be published separately.

As the gas amplification in the MWPC of the TPC sensitively depends on the hydrogen pressure, the pressure inside the TPC must be stabilized on the level of 10 bar with 0.1% accuracy. This is required to keep the MWPC gas gain constant within 1%. There is also concern that large flow variation in the TPC might induce dust accumulation and breakdown of the chamber high voltage. Thus the flow has to be stabilized as well. Finally, the whole detection system operated with high voltage in a pure hydrogen environment, thus reliability and hydrogen safety were of utmost importance.

The “Circulating Hydrogen Ultrahigh Purification System” (CHUPS) was designed and built to provide continuous protium purification and achieved all design criteria over several experimental runs with typically 2 months of continuous operation per year.

2. Circulating system (CHUPS) design

2.1. CHUPS operation scheme

During the experiment the TPC can directly monitor the capture reactions on impurities, the yield roughly proportional to the impurity concentration. This technique was used in 2003 before CHUPS was installed, showing the yield increasing during several days after filling the TPC. The chamber was filled through the palladium filter and exposed to the muon beam. The experiment revealed accumulation rate of some tens ppb per day which is unacceptable for the experimental requirements. This is the main reason for development of CHUPS designed for continuous gas cleaning and circulation through the operating TPC.

Initially a circulation system consisting of a mechanical pump and a Pd filter was considered. Pumps with high vacuum rating operating at 10 bar pressure are not commercially available and Pd filters supporting the required flux of 3 slpm (standard litres per minute) are expensive. Instead the alternative CHUPS scheme was realized, which is based on an adsorption cryopump to maintain the hydrogen flow and a cryogenic adsorption filter for removing the impurities. The adsorption cryopump has essential advantages, such as intrinsic high purity and reliability due to the absence of moving parts. The circulating system was designed, mounted and tested at PNPI in Gatchina, Russia, and installed at PSI during the preparation period

of the MuCap experiment in 2004 [2]. It was upgraded in 2005 on the basis of the operating experience. A simplified diagram of the system is shown in Fig. 1. CHUPS consists of two main units which are mounted separately on a common frame: compressor and purifier.

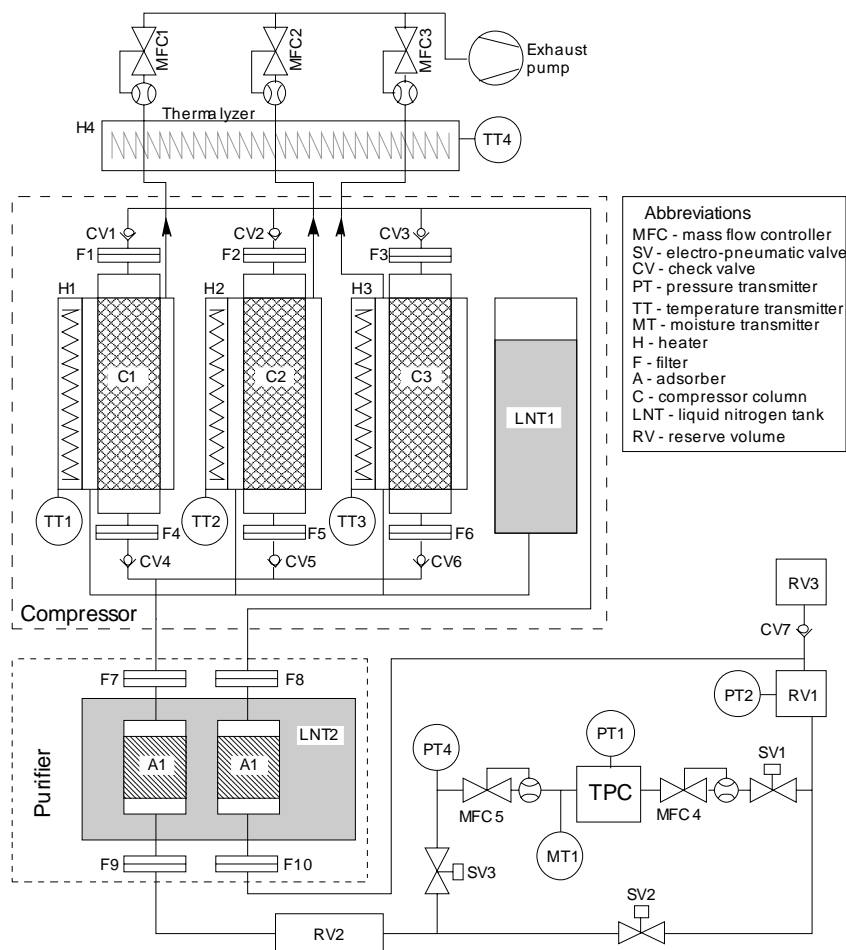


Fig. 1. Simplified CHUPS diagram

2.2. Compressor

The compressor is a triplex adsorption cryopump. It has three identical cartridges (columns) filled with activated carbon¹ and connected in parallel. The cartridges are made from thick-walled stainless steel tube and designed to keep high pressure. The volume of each column is about 1 liter and contains with respect to packed density of the carbon up to 0.6 kg of the adsorbent. Each column (C1, C2, C3 in Fig. 1) has a heat exchanger made of copper tube. It is coiled around the column and soldered to its outer surface by silver hard alloy. The heat exchanger is used to cool down the compressor column using liquid nitrogen flowing from the 40-litre supply vessel (LNT1). Liquid nitrogen flow is provided by an exhaust pump connected to the heat exchangers manifold. After cooling the columns nitrogen flows through the thermalizer (H4), which heats the gas up to the room temperature. Mass-flow controllers² MFC1, MFC2, MFC3 control the flow rate of the gaseous nitrogen and consequently regulate the liquid nitrogen flow rate and the cooling rate of the column. An electric heater is coiled around the column between the heat exchanger turns to provide the column heating. Each column has two check valves with the actuation pressure of 50 mbar that are installed in the inlet and outlet pipelines (CV1–CV6). Inlet and outlet lines of the columns are combined to the inlet and the outlet manifolds, respectively.

¹ Norit Nederland B.V. Nijverheidsweg Noord 72, 3800 AC AMERSFOORT, The Netherlands.

² Aalborg (<http://www.aalborg.com/>) stainless steel GFC series mass-flow controllers.

At the cooling stage the adsorbent inside the column adsorbs hydrogen, and the internal pressure drops below the pressure in the inlet line of the compressor. Consequently, the inlet check valve opens and passes hydrogen into the column. During the heating stage the adsorbent desorbs hydrogen, and the column internal pressure rises above the outlet line pressure. The outlet check valve opens and passes hydrogen into the outlet line. Thus, the combination of the check valves provides a pulsating flux of hydrogen in one direction. Cooling and heating rates are regulated by the balance of liquid nitrogen flow (controlled by MFC1, MFC2, MFC3) and heating power (managed by pulse-width modulation of the power supplies).

The temperature phases of the columns are shifted with respect to each other. Upper and lower temperatures and cycle frequency are regulated in accordance with the required average flow rate. A single compressor column pumps approximately 32 standard liters of hydrogen in one cycle employing a temperature range of 80–150 K. The maximum hydrogen flow of 3 slpm through the compressor is defined by the maximum cooling rate and the thermalization time of the activated carbon.

2.3. Purifier

The purifier contains two cartridges filled with NaX-type zeolite³ (indicated as adsorbers A1 and A2 in Fig. 1). The adsorbers are immersed into liquid nitrogen vessel (LNT2) and permanently kept under temperature of 77 K during the whole experimental run. Low temperature is essential to increase the adsorption ability of zeolite for high-boiling contaminants (oxygen, nitrogen) against the main gas (hydrogen). Two adsorbers contain about 40 g of the sorbent in total, enough to accumulate up to 1 g of adsorbed water. The total amount of water supplied by the flow of 3 slpm during the two-month experimental run was about 2×10^{-2} g (allowing for 100 ppb constant humidity), which is 2% of the adsorber capacity. The adsorption capacity for other contaminants is comparable. Thus, the adsorbers guarantee full impurity removal in the hydrogen flow during the long term experiment. The adsorbent has to be exchanged or can be regenerated by heating up to 400°C and pumping before each experimental run.

The liquid nitrogen vessel is contained in the vacuum case and protected from external thermal radiation by a copper shield mounted on the secondary liquid nitrogen vessel which is also used to cool down the incoming hydrogen. This technique decreases liquid nitrogen consumption and prevents heating the zeolite adsorbers. The two adsorbers of the purifier (A1 and A2) are mounted on the hydrogen lines upstream and downstream of the TPC, respectively, providing two stage purification of the gas. The inlet zeolite adsorber takes out most of the impurities, which helps to avoid any decrease of the compressor capacity due to the accumulation of impurities in the activated carbon.

The system is equipped with mechanical 2 μ m filters installed before and after the compressor and in the detector pipelines that prevent carbon or zeolite dust penetration to the clean part of the system. The final purification is provided by a special gas purifier⁴ of limited capacity installed at the TPC inlet.

2.4. Control system

A special stand-alone microcontroller block provides all necessary regulation algorithms. The control block is connected to a PC *via* RS-232 or RS-485 serial interface. Due to implementation of all control algorithms in the independent control block, the system remains operational in the case of computer failure. Computer software is used for adjusting the parameters of the regulation algorithms, collecting and visualizing the process variables and keeping them in the database. All system events (including software messages and alarms) are also saved in the database. Special software was developed to access the parameters history and event log in the database.

The control block measures and controls all system devices like pressure sensors, valves, mass-flow controllers, *etc.* It provides the following regulation procedures:

- temperature stabilization of the three compressor columns and the thermalizer by regulating the heating and cooling provided by the heaters and the nitrogen mass-flow controllers, respectively;

³ CECA company, <http://www.adsorbents.com/sites/ceca/en/home.page>.

⁴ SAES Pure Gas - MicroTorr Ambient Temperature Gas Purifiers.
<http://www.puregastechologies.com/microt.htm>.

- cyclic operation of the compressor columns with phase shift;
- TPC internal pressure stabilization using mass-flow controllers;
- temperature stabilization of the humidity sensor.

Alarm and interlock functions are also implemented in the control block firmware (see Table). It protects the detector from underpressure and overpressure and controls differential pressure between the TPC and reserve volume RV1 to avoid hydrogen flux variations. Also, the software tracks liquid nitrogen level in the compressor tank (LNT1) and compressed air pressure that is used for the electro-pneumatic valves (SV1–SV3) actuation. All alarm events are attended with light and sound signal.

Table

Alarm events and interlock actions

Alarm description	Condition	Action
TPC pressure high	PT1>PT1max	Cut-off TPC and open bypass
TPC pressure low	PT1<PT1min	Cut-off TPC and open bypass
Differential pressure high	(PT2-PT1)>DPmax	Cut-off TPC and open bypass
Differential pressure low	(PT2-PT1)<DPmin	Cut-off TPC and open bypass
Compressed air pressure low	PT3<PT3min	Alarm signaling
Liquid nitrogen level low in LNT1	N2Level<N2Levelmin	Alarm signaling

2,5, TPC pressure and flow control

The three columns of the compressor induce the hydrogen flow to exchange the gas in the TPC. This flow is pulsating because of the periodical mode of the column operation. The pressure inside the TPC must be stabilized with 0.1% accuracy. In order to smooth the pressure variations caused by compressor, the CHUPS system is equipped with two reserve volumes of 15 liters content each (RV1 and RV2), pressure sensors (PT1, PT2, PT4) and mass-flow controllers (MFC4 and MFC5).

The reserve volumes are installed in the inlet and outlet lines of the TPC. They are used as buffering volumes. The RV1 also provides a hydrogen reserve to support the pressure stabilization algorithm. Each volume is equipped with a pressure sensor (PT2 and PT4, same model as PT1). Two mass-flow controllers with a maximal flow of 20 slpm are mounted at the inlet (MFC4) and outlet (MFC5) lines of the TPC.

The internal pressure of the detector (measured by PT1) is stabilized using PID (Proportional-Integral-Derivative) regulation. The mass-flow controller at the detector outlet (MFC5) is set to a constant flow rate. The TPC inlet mass-flow controller (MFC4) is operated by PID algorithm in the control software. The MFC5 set point defines the average flow rate through the TPC vessel. The pressure distribution histogram (Fig. 2) for the long term operation during 50 days shows excellent pressure stability on the level of 0.024% at a mean hydrogen flow of 3 slpm. The histogram bars correspond to the ADC discretization in the control system (1.2 mbar). Thus the pressure is kept within ± 2 least significant bits of the ADC. The second reserve

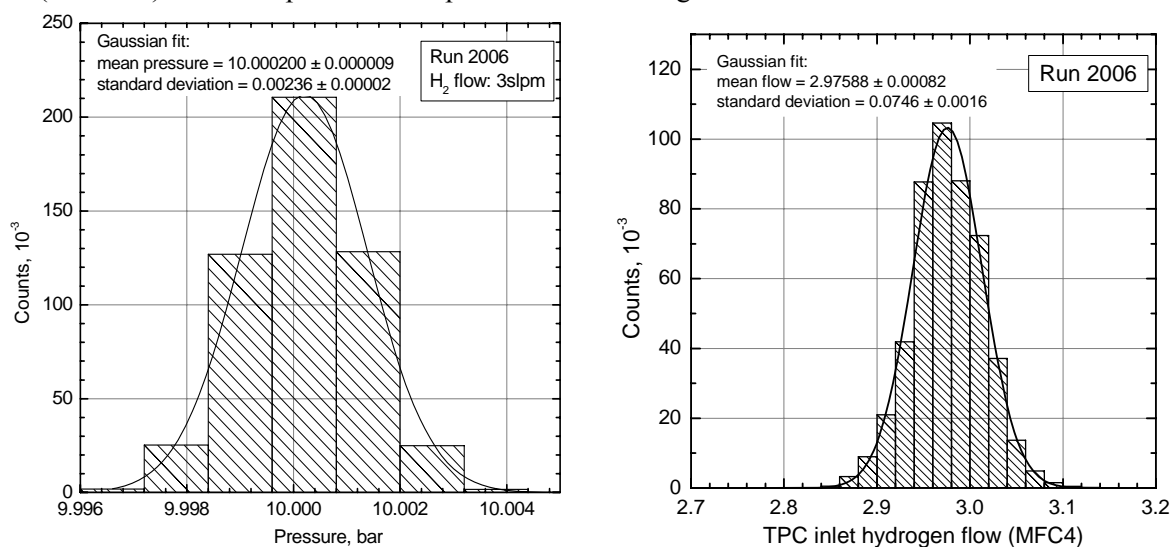


Fig. 2. TPC pressure and inlet flow distribution histograms. The gaussian fits gives a full width of 2.4 mbar and 0.075 slpm that correspond to 0.024% and 2.5% stability, respectively

volume (RV2) and the mass flow controller (MFC5) at the compressor inlet were installed to prevent pressure drops caused by the fast opening of the check valve. This results in a flow stability of 2.5% at the mean flow level of 3 slpm during 50 days of CHUPS operation (Fig. 2).

3. Monitoring impurities

The initial purity of the evacuated TPC system was provided by continuous pumping and baking of the TPC vessel. The residual gas contents were controlled by a quadrupole mass-spectrometer in the mass range from 2 to 100 atomic mass units (a.m.u.). During the protium runs atmospheric gases (oxygen and nitrogen) were analyzed by off-line gas sample chromatography, and the moisture of the gas was directly monitored with an on-line humidity sensor. The total amount of impurities was continuously monitored by direct measurements of the yield of muon capture on impurities as observed in the TPC.

3.1. Chromatographic analysis of nitrogen and oxygen

The oxygen and nitrogen content is measured by gas chromatography with a thermal conductivity sensor. After being filtered and purified in a cryogenic adsorption purifier, helium carrier gas is distributed in two directions with equally adjusted flow rates. The first flow passes through the reference chromatographic column. The second flow can be either routed to the working chromatographic column directly or through the accumulating column using the volume batcher which injects the fixed volume into specified direction. Both chromatographic columns are filled with a specially treated adsorbent (zeolite). The adsorbent in the working column separates the admixtures, while the one in the reference column provides a hydraulic resistance equal to the working column.

Preparatory enrichment is required for the very low concentrations of impurities in the hydrogen gas samples. Hydrogen from the sample bottle is directed to the accumulating column by the batcher. This column is filled with zeolite and immersed into a liquid nitrogen vessel at 77 K temperature. The amount of gas passed through the accumulating column is measured by a rotary drum gas meter. Impurities from the gas stream are adsorbed by the zeolite and remain in the accumulating column. After the desired amount of sample gas has passed through the adsorber, the accumulating column is removed from the cryogenic vessel and heated. Then the batcher directs the helium carrier gas flow through the accumulating column which washes the impurities out of the adsorbent.

In the next step, the carrier gas enriched by contaminants flows through the working column, where contaminants are separated on the adsorbent. Both reference and working flows pass through the detector in parallel, that measures their differential heat conductivity. The differential output signal is proportional to the admixture concentration. Signal peaks are registered by a PC and processed by special software. The enrichment coefficient (the sample volume passed through the accumulating column) and parameters of the measuring scheme are adjusted with respect to the admixture concentration. The final calculation of the concentration is based on a calibration measurement. A serial dilution method was used to obtain the set of calibrating samples with decreasing concentration of nitrogen and oxygen. With this method a sample of the air was serially attenuated by the hydrogen. The total calibration error, including non-linearity, is 10%. The traces of the main air components were monitored by gas samples of 8–10 normal liters from the TPC using the chromatographic method. A sensitivity of 5 ± 1 ppb for oxygen and 7 ± 1 ppb for nitrogen was obtained.

3.2. Humidity analysis

During the MuCap experiment 2004 we observed a capture yield corresponding to about 60 ppb impurities, significantly higher than the oxygen and nitrogen concentration derived from the gas chromatography

In 2005 an online humidity sensor⁵ was installed to investigate whether the additional observed yield can

⁵ Pura PUR-TX-120 Gas Dew-point Transmitter. Michell Instruments.
<http://www.michell.co.uk/cat/view/pura.html>

be explained by residual water vapor in the hydrogen gas. The sensor has sensitivity of 0.02 ppb with error of +30–50% in the 2–100 ppb range. It was mounted in a temperature-stabilized box in order to reduce any influence of the ambient temperature to the sensor reading. Sensor and inlet pipeline were kept at 21°C with 0.2°C stability. As shown in Fig. 1, the humidity sensor (MT1) was installed in the gas circuit such that it could measure either the humidity in the outlet TPC flow or in the isolated CHUPS system (while hydrogen is circulating through the chamber bypass). Continuous bypass circulation gave 3 ppb humidity. During the production run the humidity sensor clearly demonstrated that humidity was the main additional impurity. To calibrate the effect of H₂O impurities on the experiment, a water permeation tube⁶ was used for generation of the known water concentration in the hydrogen flow. The tube was placed in the temperature stabilized vessel. Stable hydrogen flow was passed through the volume with the tube.

3.3. Impurity capture rates

The specifics of the MuCap experiment allow unique in-situ measurements of impurity concentrations during the experimental runs. While the vast majority of negative muons remain in muonic hydrogen atomic (μp) and molecular ($p\mu p$) states during their lifetime, a small fraction can be captured on impurities in the following steps: $\mu p + N_Z \rightarrow \mu N_Z + p$; $\mu N_Z \rightarrow N_{Z-1} + \nu$. Here N_Z is a nucleus of an impurity atom, like N or O. The first transfer reaction proceeds with a rate proportional to the impurity concentration c_Z . The second capture reaction occurs with a probability $\Lambda_Z/(\Lambda_Z + \lambda_+)$, which is the result of the competing processes of capture with rate Λ_Z and free muon decay with rate λ_+ . The charged recoil nuclei N_{Z-1} are detected in the TPC. The observed yield of capture recoils per muon is $Y_Z = c_Z k_Z$, where k_Z are coefficients which depend on Λ_Z and the detection efficiency for recoil N_{Z-1} . They are determined in dedicated calibration runs where hydrogen is doped with a single impurity N_Z of well measured concentration c_Z , typically 100–1000 times higher than in the clean run conditions. Typical values are $k_N = 70$ and $k_O = 400$ for both Y_Z and c_Z in ppm (the detection efficiencies slightly differ from run to run). In summary, the capture yield measurement allows a continuous and precise measurement of the overall observed capture yield from impurities, but it does not distinguish between their elemental composition.

4. Operating experience

4.1. Clean fills for production data

Before the 2004 experiment the TPC was baked for several weeks. The performance of the gas system over the whole run period is documented in Fig. 3. The chromatographic analysis allows monitoring the change of oxygen and nitrogen concentrations during the MuCap experimental run. Fig. 3 shows the behavior of nitrogen concentration for the MuCap experimental run after starting the CHUPS. The final chromatographic measurements resulted in nitrogen concentrations less than the method sensitivity (7 ppb). Oxygen traces dropped below the method sensitivity of 5 ppb within two days after starting the circulation.

The most reliable drying experience was obtained during the spring 2006 experimental run. Before the run, the TPC had been exposed to continuous (about 2 months) vacuum pumping with a simultaneous baking at ~120°C. This procedure led to an initial humidity level at the moment of CHUPS connection of 60 ppb (Fig. 4, left). During 400 hours of continuous cleaning with a mean hydrogen flux rate of 3 l/min the humidity exponentially decreased to ~18 ppb and remained at this level till the end of the main μ^- data run, providing a stable operation over more than 1000 hours. The minor fluctuations of the humidity are explained by temperature fluctuations in the experimental hall. The change of hall temperature affects the adsorption-desorption equilibrium in the chamber and, consequently, its outgassing rate. Then CHUPS was disconnected from the TPC and run through bypass line. The humidity decreased exponentially and reached the 10 ppb level in 20 hours (Fig. 4, right). The final CHUPS stand-alone humidity result is 3 ppb.

⁶ Permeation tube providing 500 ppb \pm 10% at 0.5 slpm flow. Valco Instruments Company Inc. P.O. Box 55603, Houston, TX 77255, USA.

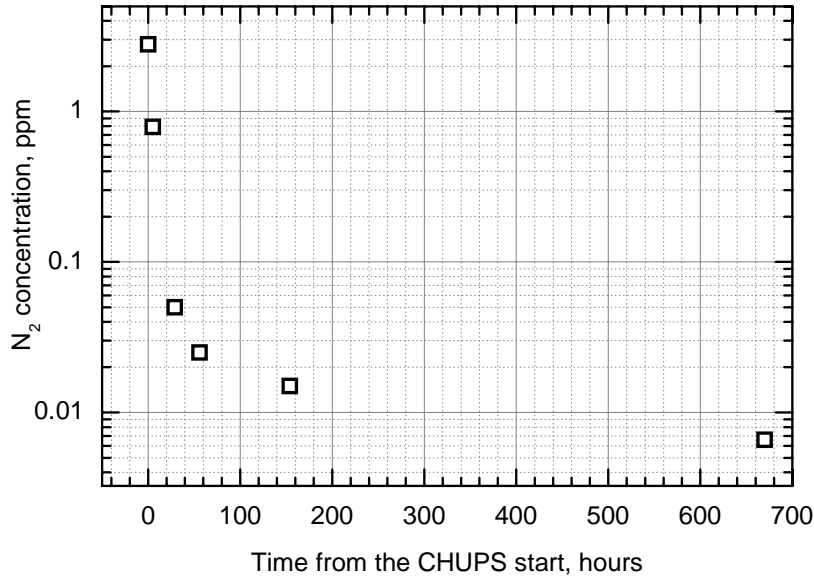


Fig. 3. Nitrogen concentration change during MuCap run 2004. Average hydrogen flow is 1.6 l/min

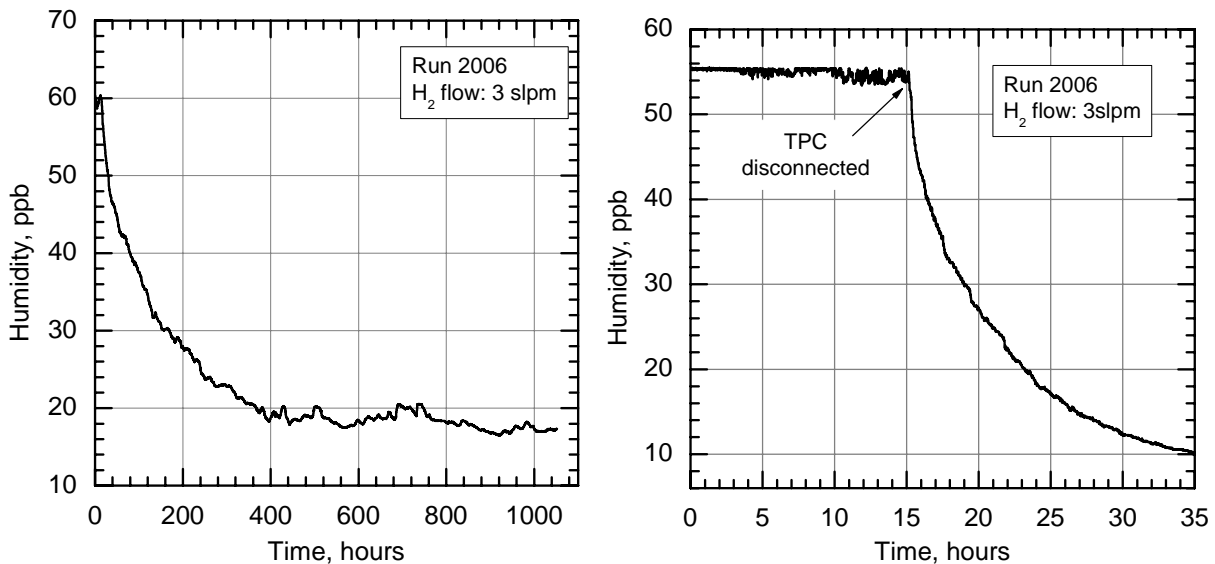


Fig. 4. Humidity decrease in the TPC after CHUPS connection (left) and after bypassing the TPC (right)

4.2. Impurity doped fills for calibration data

The cleaning power of CHUPS was greatly confirmed during systematic calibration studies of the TPC detector which were carried out during the last weeks of the MuCap experimental run in spring 2006. Several experiments were carried out for the TPC calibration and the determination of the major impurities. The high cleaning power of the CHUPS system makes it possible to return the detector to the normal clean operation in a short time.

The first experiment was a “water doped run”. During this test the humidity inside the TPC was increased up to 2000 ppb approximately by a specially prepared humidity generator. Then CHUPS was connected and the gas was cleaned down to 400 ppb in one day (Fig. 5). The slower cleaning speed can be explained by wetting of the inner surfaces of the chamber.

The efficiency of CHUPS cleaning a large contamination of nitrogen in the detector hydrogen was tested by adding a “high” 22 ± 1 ppm nitrogen admixture from a known amount of nitrogen previously diluted

in a vessel with high purity protium. This “nitrogen doped” condition was intended as a detection efficiency calibration of nitrogen impurity capture events in the TPC. After measuring with the large nitrogen contamination (flat region) the CHUPS circulation through the TPC vessel was re-established and the nitrogen was removed. The cleaning progress observed on-line *via* capture events in the TPC is shown in Fig. 6. The cleaning started with a yield of more than 1000 ppb and proceeded until leveling off around ~30 ppb, a value established before the doping. The purification process took about 17 hours.

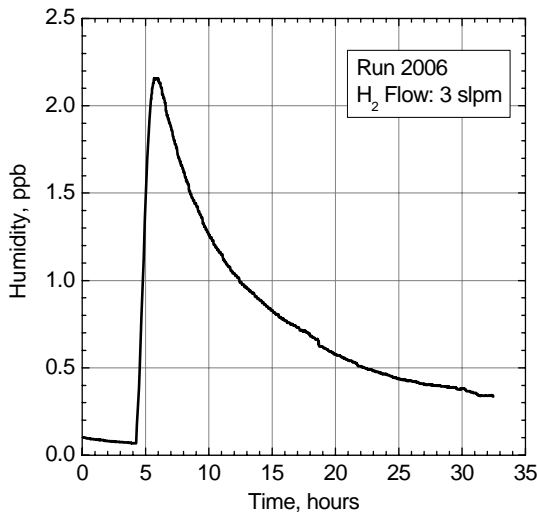


Fig. 5. Drying of TPC after the water doped run

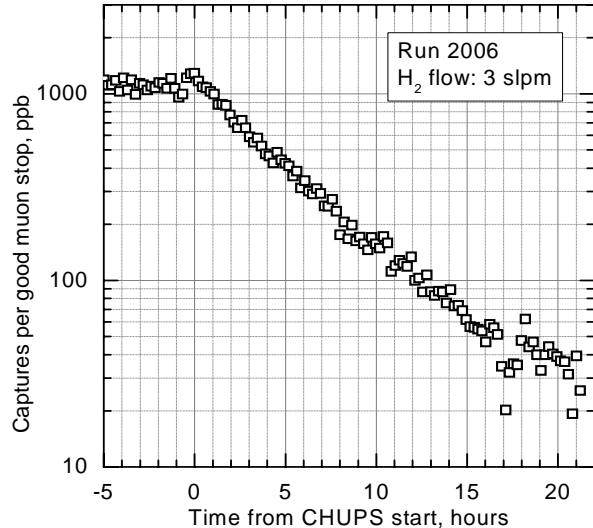


Fig. 6. Impurity captures per good muon stop during the nitrogen cleaning

4. Results

The CHUPS system was installed in the MuCap experiment at PSI and first connected to the TPC detector in 2004. The system proved to be very reliable and flexible during three experimental runs in 2004–2006.

The experience obtained during development and use of the CHUPS justifies the initial design decisions. The main result was a stable clean working gas of the TPC during the experimental runs. A smooth hydrogen flow of 3 l/min was kept during the whole TPC operation time (more than 1000 hours in one experimental run). The best purity reached was 18 ppb for moisture content and 8–10 ppb for nitrogen concentration. This result is sufficient to reach the main goal of the MuCap experiment and allows precise corrections of the proton capture rate for these impurities. In addition to regular cleaning, the CHUPS provided fast cleaning of the working gas after calibrations with contaminants doping. This feature was very useful for the nitrogen and water calibration experiments intended for systematic studies of the TPC detector. Also, variations of the CHUPS flow and correspondingly the equilibrium humidity in the chamber gave important additional calibration points for the systematic investigations.

With regards to the stable pressure requirement the CHUPS also yielded a good result. The pressure inside the TPC was kept at the appropriate level of 10 bar with 0.024% stability during all the operation modes. Pulsations of the hydrogen flow through the TPC chamber were also minimized to the level of 2.5% at the mean flow of 3 l/min.

References

1. I. Alekseev *et al.*, Preprint PNPI-2702, Gatchina, 2006. 26 p.
2. B. Bezmyannykh *et al.*, Preprint PNPI-2611, Gatchina, 2004. 17 p.

HYDROGEN DISTILLATION AT THE DEUTERIUM REMOVAL UNIT OF MuCap EXPERIMENT

I.A. Alekseev, E.A. Arkhipov, S.D. Bondarenko, O.A. Fedorchenko, V.A. Ganzha, P.A. Kravtsov, V.A. Trofimov, A.A. Vasilyev, T.V. Vasyanina, M.E. Vznuzdaev

1. Introduction

The MuCap (Muon Capture on the Proton) experiment has been carried out during 1998–2006 at the Paul Sherrer Institute (PSI), Switzerland. The goal of this experiment is to measure the rate of the basic electroweak process of muon capture with hitherto unachievable high precision (1%). This measurement will provide an estimation of the nucleon charged form factor g_P with all-time high accuracy $\sim 7\%$.

The method needs a very precise measurement of the muon lifetime in the μ^-p system in comparison with the lifetime of the free μ^+ . To achieve this precision, ultra pure and deuterium depleted hydrogen gas (so-called protium) must be used. It is necessary to avoid transfers of μ^- to impurities or deuterium nuclei. These transfers lead to spoiled time spectra. A new experimental technique based on high pressure time projection chamber (TPC) filled with protium was used for the measurements. The experiment imposes strict and critical requirements on the hydrogen gas system supporting the detector. Desirable overall part of contaminants is about 10^{-8} for chemical impurities and 1×10^{-7} for deuterium. Circulating Hydrogen Ultrahigh Purification System (CHUPS) was built to provide the permanent purification of protium from the chemical contaminants during an entire statistics run (up to 2 months of continuous operation) [1]. This system was recently equipped with the Deuterium Removal Unit (DRU) – device for manufacturing of ultra pure protium from hydrogen [2]. A principle of hydrogen cryogenic distillation was used as a basis for the unit design.

The rectification method uses the difference in saturation vapor pressure of separating species above the surface of the mixture. This facility can be either a set of perforated plates or particular packing. The packing is more suitable for a column with a relatively small inner diameter. On the top of the column a condenser is placed which condenses vapor and returns it into the column in the form of liquid (reflux). The vapor from the top of the column can be partially taken away from the column as a product of the process. The reflux drains down along the column moistening the packing. An amount of the liquid suspended on the packing is a column holdup. Lower end of the column is equipped with reboiler. A separated mixture boils in the reboiler forming the vapor. The vapor rises upward along the column and interacts with the counterflow of draining reflux: the liquid is saturated by the high-boiling component, and the gas – by the low-boiling one.

In our case of hydrogen-deuterium separation a separating mixture is the mixture of regular hydrogen (H_2) and “deuterohydrogen” (HD). D_2 molecules are extremely rare and should not be considered. Besides, there is a division of the H_2 molecules into two groups, one of which has its protons aligned in the same direction (referred to as orthohydrogen) and the other in opposite directions (parahydrogen). Ordinarily, transition between ortho and para forms are relatively rare, so H_2 can be considered as a mixture of two distinct components. The ratio between the ortho and para forms is about 3:1 at standard temperature and pressure, but the para form dominates at low temperatures.

Separation factor α defines an elementary separation effect achieved at one contact of liquid and vapor hydrogen. Ideal separation factor is a ratio of saturation vapor pressures above pure components, it depends on temperature: the higher temperature the lower separation factor. But the separation factor for deuterium-protium is much larger than for ortho-para hydrogen at the same temperature. Throughout the contacting tower, liquid and vapor are brought into repeated contacts that multiply elementary separation effect. Thus the flowing down liquid hydrogen becomes steadily enriched in deuterium and orthohydrogen while the rising vapor becomes steadily depleted. According to the concept of Equilibrium Theoretical Plate, Height Equivalent to a Theoretical Plate (HETP) is the main performance characteristic of a separation column. HETP is the height of a part of a column left by liquid and gas flows which are in equilibrium to each other, (*i.e.*, for example, deuterium concentration in the liquid is α times higher than in the gas). The lower HETP value the higher column's separation power.

The column was designed to be operated so as to separate the initial mixture injected into the column through a feed port withdrawing pure H₂ (with deuterium content at least 30 times lower than in feeding gas) as distillate product and discarding the HD component in the reboiler stream. For the safety reasons and to select the most suitable operating mode, a number of studies and verifications were carried out. They include checks of the mechanical design and integrity and investigations of the pressure drop, the liquid holdup and column performance at different modes. Also, these investigations are very important to evaluate the accuracy of the measurements. The results of these studies are reported here.

Inefficiency of low deuterium content analysis in protium and the fact that possible residual deuterium content of the depleted product can be lower than the detection limit complicate the verification of separating power. It has made us find another approach. The use of gas chromatography method for ortho-para hydrogen analysis was found as a relatively fast and simple way of column performance evaluation. Also, low deuterium probes were measured on the small accelerator built specially for isotope analyses with special ion source giving extremely low backgrounds of hydrogen ions.

2. The mechanical design of the deuterium removal unit

The simplified layout of the DRU is presented in Fig. 1. Separation column of 2.2 cm inner diameter and 155 cm overall packing height is the main part of the unit. It consists of two sections connected with ISO CF40 flange coupling and is cased in a vacuum jacket. The 2.5 m vacuum jacket fixed on tripod is a basis for the setup. All working parts of the device are placed inside the jacket and its upper and lower attachments (so-called adaptors). The jacket and the adaptors comprise a common vacuum volume.

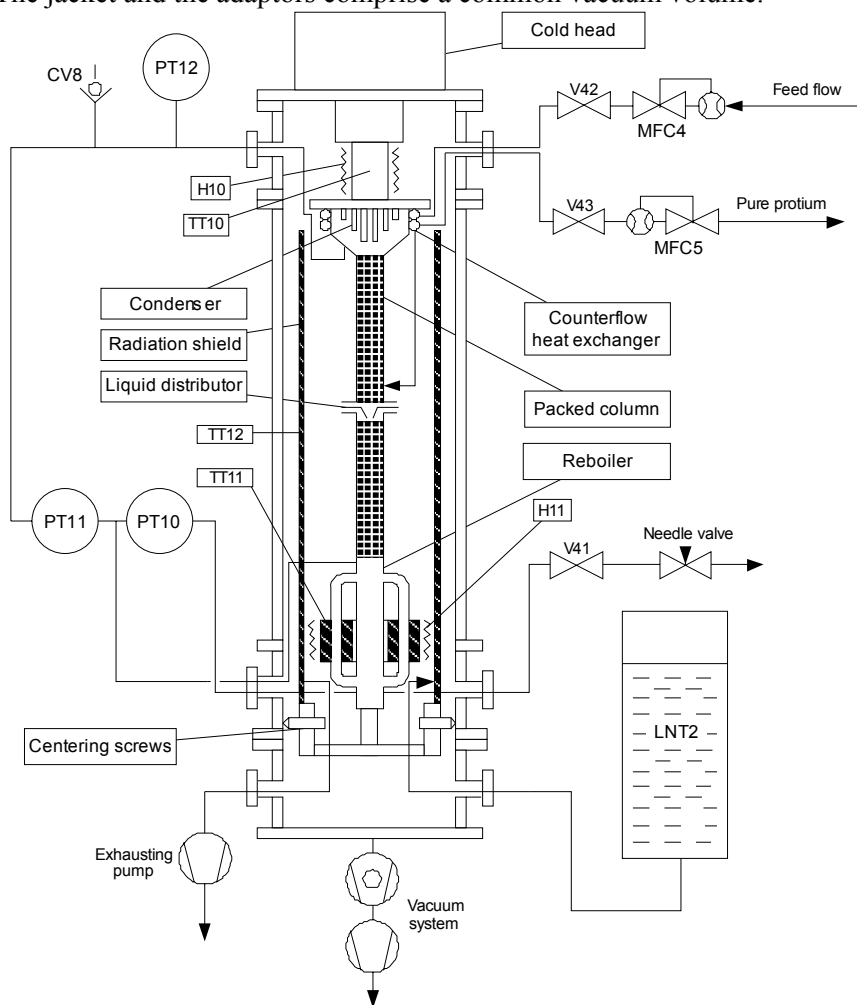


Fig. 1. DRU simplified diagram

The column has a condenser and a reboiler connected with its upper and lower parts. A COOLPOWER 140T (Leybold vacuum GmbH) cryogenerator was used for the cold operations, with the maximal cooling power of 20 W at 20 K.

A conical liquid distributor is fixed between the upper and lower sections of the column. Both sections of the column are filled with random packing. The liquid feed stream (see comments below) is introduced into the bottom of the upper section of the column. The distributor is intended to collect the liquid trickling down from the upper section and guide it to the center of the lower section. It is essential to prevent the effect of “adhesion” of the liquid to the column’s wall.

The control system provides the algorithms necessary for column’s operation in all modes. It operates two mass-flow controllers (MFC4 and MFC5) and two heaters (H10 and H11) and measures temperature and pressure sensors.

2.1. Condenser

The condenser is a closed conical bimetallic volume (Fig. 2, left). Its flat upper part is made of 10 mm copper plate. Inner part of this plate is processed in a form of a row of lamellas to develop the heat transfer surface area. Vertical orientation of the lamellas provides easy sliding of hydrogen condensed drops downward. The conical part has a flange for connecting to the column and welded to the copper plate by electron-beam. The condenser has two connections (tubes with 1 mm internal diameter) for conducting product hydrogen and its pressure to an upper point of the differential manometer PT11.

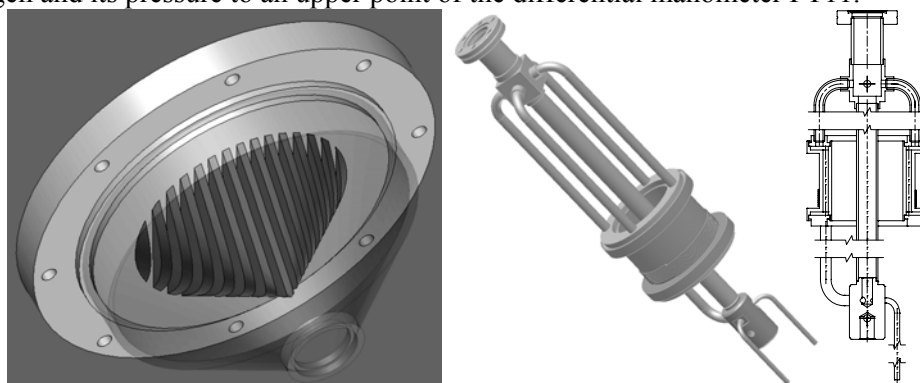


Fig. 2. The condenser (left) and the reboiler (right)

The cold head tightly contacts with outer surface of the copper plate through an indium foil. The cooled part of the condenser is mounted in the upper adaptor and that way in the common vacuum insulation of the column. A counterflow heat exchanger is mounted around the condenser and fixed on its upper flange. It cools down the feeding flux flow (inlet flow) by the deuterium depleted product flux (outlet flow).

2.2. Reboiler

The reboiler (Fig. 2, right) is essential to supply evaporation of the separating mixture. It has rather complicated arrangement to provide steady controllable boiling. This unit consists of central pipe, copper muff, upper and lower collectors and several connecting tubes. The central pipe keeps the most of liquid hydrogen collected in the bottom of the column. Both of collectors are welded to the pipe. The lower collector is also connected to the boiler by the short connecting tube. The massive copper muff has a large central hole. Several longitudinal apertures are drilled in the muff around the big hole. Their outlets are opened into common upper and lower grooves which are closed by stainless steel covers. The covers are welded to the boiler’s body. Bimetallic structure allows the boiler to have very good heat conductivity owing to the copper body and therewith solid connection with other steel parts through the steel covers. The boiler is equipped with electric heater coiled around its body and PT100 thermometer to control its temperature. Liquid hydrogen boils in the longitude apertures and its vapor moves upward through four long connecting tubes. The short connecting tube provides a circulation between the lower collector and the boiler.

The advantage of the considered assembling is the separation of main amount of liquid hydrogen from the boiling section. Because of this separation, we obtain a steady level of liquid hydrogen inside the central pipe, which is measured by a differential manometer PT10. The low pressure point of this manometer is

connected to lower part of the column and the high pressure point – directly to the lower collector. ISO CF16 and CF40 connections are used for coupling of column parts. This type of connection is characterized by excellent vacuum tightness and good temperature cycling reliability.

2.3 Packing

The column is filled with specially designed spiral prismatic random packing made from 0.2 mm stainless steel wire. The packing is intended to provide a maximal surface of phases contact. At the size of the prismatic springs of 2 mm × 2 mm and total volume of packing in the column 560 ml it gives surface of 1.95 m². The choice of stainless steel as a material is caused by purity conditions of hydrogen. The packing surface was pickled by nitric acid to develop its roughness and improve wettability by liquid hydrogen.

It was the first test of the packing in a cryogenic distillation column. This type of packing (but bigger size – 3 mm × 3 mm) was earlier tested in PNPI's water distillation columns of 80 mm inner diameter and showed good separation characteristic (HETP = 2.5–3 cm) [3]. The similar packing made from stainless steel tested in cryogenic distillation column of small diameter gives HETP value about 5–6 cm. That is why the value of HETP equal to 5 cm was put in the design according to conservative approach.

3. Experiments and results

In April–May 2006 the DRU was tested during a few long (up to 7 days) periods of operation. The total amount of pure protium produced by the column in this run was 1300 litres. Almost all tests of columns performance were carried out at so-called “total reflux mode”, with zero feed flow and correspondingly withdrawal flows from the column top and bottom.

3.1. Analysis

The analysis of low deuterium content in hydrogen is not prompt and besides the residual deuterium content of the depleted product can be lower than the detection limit. Nevertheless, a method for fast estimation of column performance was strongly needed. A chromatographic analysis of ortho- and para-isomers of hydrogen was proposed as a method of indirect estimation of the column separation power.

For the analysis the same chromatographic device was used as for analysis of nitrogen traces. However there are some changes introduced into the device for this specific method of analysis. The first distinction was the use of Al₂O₃-filled chromatographic column immersed into liquid nitrogen. The liquid nitrogen temperature is essential to provide the separation of the isomers that have temperate difference in adsorption affinity. The other essential difference is the direct injection of the sample into the carrier gas without the preliminary accumulation of impurities. The accumulation is unnecessary because of relatively high concentration of the separated components. The third serious property of this method was the use of neon as the carrier gas. It was used to provide more difference in thermal conductivity between the separated species and carrier gas in comparison with conventionally used helium.

Measurement of the concentration of ortho- and para- isomers in the top and bottom parts of the column allows to estimate its separation performance and recalculate the concentration profile for deuterium. A sample of chromatogram for samples taken from the top and bottom part of the column is shown in Fig. 3.

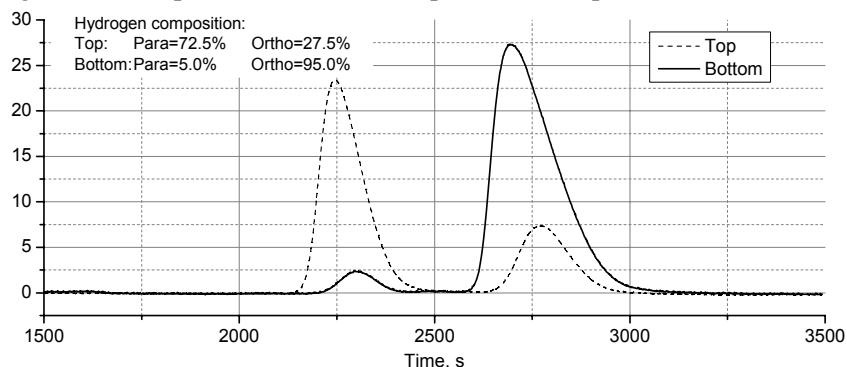


Fig. 3. Chromatogram of separated ortho- and parahydrogen (column pressure = 1.2 bar; reboiler power = 10 W; operation mode: total reflux)

Separation ratio is the ratio of relative concentration of a component of interest at the bottom to the top of the column: $SR = \frac{X_{Bottom}/(1-X_{Bottom})}{X_{Top}/(1-X_{Top})}$. If separation factors are known for the total reflux operating mode the

recalculation of ortho-para hydrogen separation ratio (SR) into deuterium-protium separation ratio can be done easily with the help of Fenske equation: $SR = \alpha^N$, where N – the number of theoretical plates. A separation factor α is the value of elementary separation effect. It can be presented as a ratio between saturation vapor pressures for pure components. For ortho-para separation it can be shown as:

$\alpha_{o-p} = \frac{P_{sat.Para}}{P_{sat.Ortho}}$, where α_{o-p} – ideal separation factor for ortho-para hydrogen system, $P_{sat.Para}$ and $P_{sat.Ortho}$ – saturation vapor pressures above pure para- and orthohydrogen, respectively. Thus, for the deuterium-

protium case: $\alpha_{D-H} = \frac{P_{sat.H_2}}{P_{sat.HD}}$, where α_{D-H} – ideal separation factor for system of protium and

deuterohydrogen, $P_{sat.H_2}$ and $P_{sat.HD}$ – saturation vapor pressures for pure normal H₂ and pure HD, respectively.

Dependencies of separation factors for HD–H₂ and ortho-para hydrogen system on temperature are shown in Fig. 4. The significant difference between the separation factors according to Fenske equation results in much larger difference between the separation ratios for a large number of theoretical plates in the column (or height of the column: $N = H/HETP$). Height Equivalent to a Theoretical Plate (HETP) is the main characteristic of column's performance. The higher separation power corresponds to greater number of theoretical plates (N) and less HETP value.

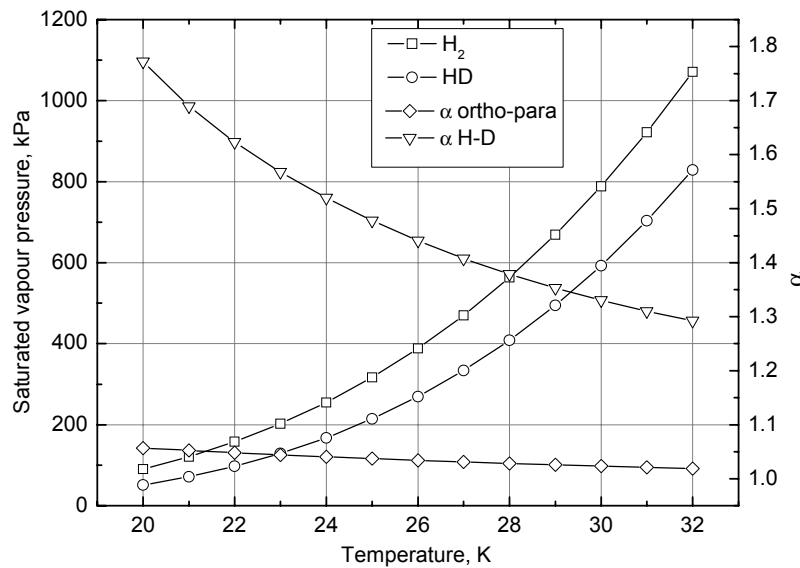


Fig. 4. Temperature dependencies of saturated vapor pressures and separation factors for H₂–HD and ortho- parahydrogen systems

3.2. Results of natural gas separation at total reflux mode

First DRU run was carried out with the natural hydrogen with 126.7 ppm of Deuterium. The column was filled by liquid hydrogen in large excess, and after 1 hour operation excess gas (84 litres) was withdrawn from the column bottom. This explains low final deuterium concentration in the bottom (Table 1). Withdrawn gas was sufficiently enriched to change largely the average concentration in the column. Initial gas volume was 181.6 litres. Negative deuterium concentration in the column top (~1.9 ppm) indicates the accuracy of the measurement. The method consists in extrapolation of sample measurement from deuterium concentration in natural hydrogen and gives low accuracy nearby zero concentration.

Table 1

Natural hydrogen run results

Probe location	Deuterium, ppm	Ortho, %
Original gas	126.7	75
Column top	-1.9	14.6
Middle	-	32.2
Column bottom	56.2	85
Average concentration calculated from the mass balance	7.7	53.5

The experimental data for the ortho-para separation was fitted by the Fenske equation. The average HETP calculated on the basis of tests with various vapor flow rates was 2.2 cm (Fig. 5), which is comparable with the best results in the world.

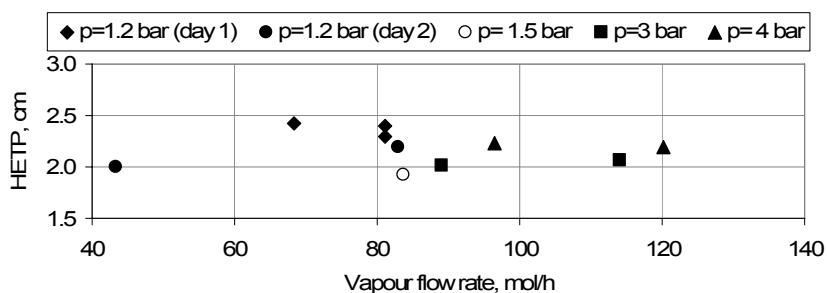


Fig. 5. HETP dependence on vapor flow rate

3.3. Studies on the pressure drop and the liquid holdup

Figure 6 (left) shows the relation between pressure drop across the column and vapor flow rate for the tested mass exchange packing. Unfortunately we did not reach flooding due to relatively large inner column diameter. Original design value was 16 mm, but according to the number of circumstances the inner diameter of 22 mm was chosen, this means that packing was working at relatively low load. We had some anxieties in this respect but fortunately they were relieved due to the excellent packing performance. Packing holdup presented in Fig. 6 (right) had an expected high value. In spite of this the time of reaching a steady state by the column is short – about 1 hour.

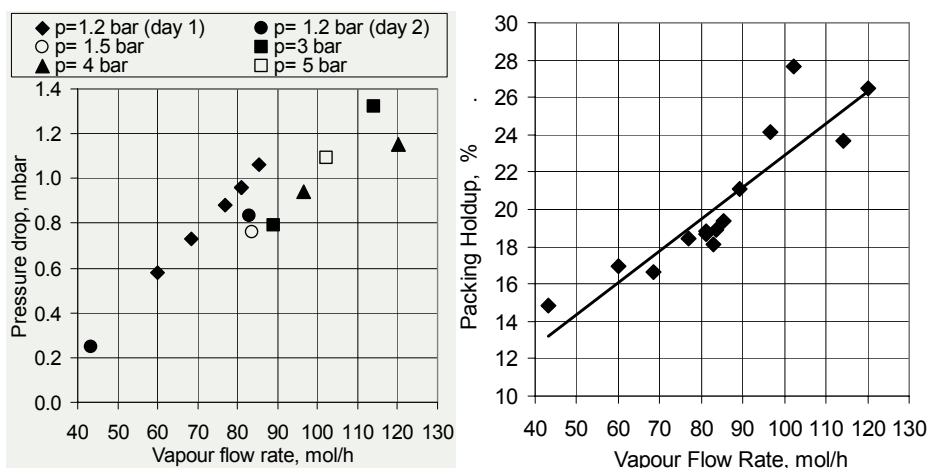


Fig. 6. Pressure drop across the column and packing holdup

3.4. Production of Deuterium Depleted Protium

There are several possible DRU operation modes for the deuterium depleted protium production. Four modes were tested during experiments: “feed through” with purging, “feed through” without purging, continuous circulation through CHUPS and so-called Rayleigh depletion. During the Rayleigh depletion the column was totally flooded by liquefied hydrogen. After the flooding, the hydrogen was discharged through the product line. Natural hydrogen was used only for preliminary tests. The accumulating of required product was carried out from pre-depleted protium. Mass-flow controllers of CHUPS system were used to operate the feed (MFC5) and for the product flow (MFC4). The rate of the purging flow was adjusted by manual needle valve with the help of bubble flow meter. The results of the cleaning runs are shown in the Table 2.

Table 2

Results of the cleaning

Mode	"Feed through" no purging	"Feed through" with purging	Rayleigh's depletion	CHUPS Circulation	
Reboiler power, W	20.5	19.0	12.0	20.0	
Pressure, bar	1.5	1.5	1.5	2.0	
Feed flow, l/min	0.81	0.81	1.25	0.55	
Ortho, %	Top	67.8	69.4	-	64.8
	Middle	69.2	74.6	94.2	69.3
	Bottom	96.4	98.5	-	98.2
HD initial, ppm	3	3	10	<3	
HD expected, ppm	Top	< 0.01	< 0.01	0.09	< 0.01
	Bottom	123	~ 200	370	-
HD probe	№ 50	№ 57	№ 61	№ 67	
Amount of gas, SL	572	630	390	420	
Bottom probe HD measured, ppm	57.5 ± 1.2	76.9 ± 1.6	probe lost	16.2 ± 0.5	

In addition, a number of deuterium depleted probes were collected (so-called zero protium samples). Expected HD concentrations were calculated using the special program “CD-2004” on the basis of the column’s model with known HETP and total height. The measurements of the probes were performed on the new 200 kV Tandem accelerator built for isotope analysis in Zurich. A special ion source was constructed giving extremely low backgrounds of hydrogen ions from walls, *etc.* The walls are continuously sputtered to keep the background low allowing measurements during 2 hours. The existence of the zero samples from the DRU system turned out to be crucial, since the accelerator gives a different background if the ion source is not fed with hydrogen gas. First zero sample measurement gave zero deuterium concentration at 0.14 ppm sensitivity. Thus, it contains less than 0.14 ppm of deuterium. The difference in expected HD concentration and measurement for probes 50 and 57 is most likely caused by wrong assumption about initial HD concentration, which was measured with extrapolation method and has large error. According to probe 50 measurement, the initial HD concentration should be 1.40 ± 0.03 ppm that corresponds to the initial hydrogen measurement on the accelerator (1.44 ± 0.13 ppm).

Deuterium concentration profile in the column, calculated on the base of the ortho- and para-hydrogen separation, gives very low concentration in the top of the column (Fig. 7). Such a low concentration could not be proved by direct measurement because of relatively low sensitivity of the mass spectroscopy.

The additional direct analysis of zero samples using accelerator mass spectrometry in Zurich gave a better result for depleted hydrogen from the top of the column: less than 60 ppb at 60 ppb sensitivity. This is ten times better than technical requirements of MuCap experiment.

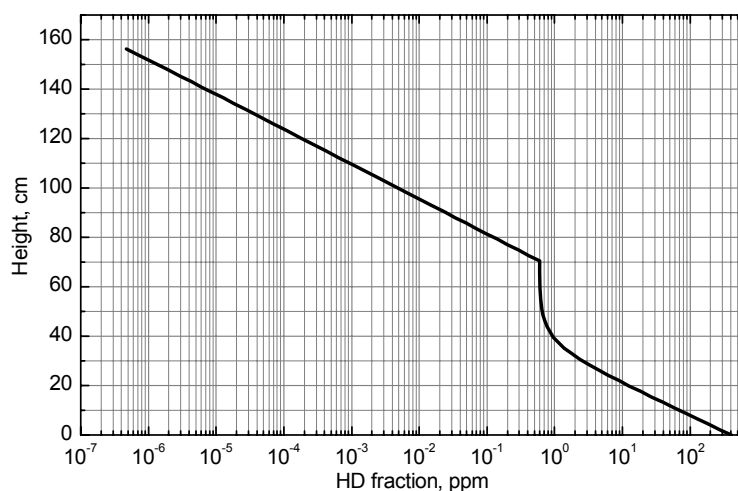


Fig. 7. Expected HD concentration profile. Feed flow = 1 L/min; pressure = 1.5 bar; purging flow = 0.015 L/min; HETP = 2.2 cm; initial deuterium atomic fraction = 3 ppm

4. Conclusion

The Deuterium Removal Unit was designed and manufactured in PNPI during the fall and winter of 2005–2006. The final installation, tests and protium manufacturing were carried out in spring 2006 at the PSI. The separation characteristics of the column were studied in details. Due to the absence of direct prompt method of deuterium measurements, the indirect method of chromatographic analysis for ortho- and para-isomers of hydrogen was used to estimate the column's separation efficiency. Some interesting data were obtained.

The height equivalent to a theoretical plate (HETP) for the column is 2.2 cm. It is one of the best ever obtained results for columns of low and medium cryogenic power. For the present column, HETP value is almost constant in a wide range of vapor flow rate.

The column has the separation power in excess for the goal to be sought. Output deuterium concentration lower than 0.1 ppm almost does not depend on the initial concentration (natural hydrogen can be used!).

The pure orthohydrogen useful for some experimental physics applications can be produced by the setup as well as protium.

After the selection of column's operating parameters and the development of its operating algorithm the protium production run was performed. Several modes of isotope purification were used. As a result about 1.3 m³ of deuterium depleted hydrogen was obtained. The CHUPS system was put into the mode of continuous hydrogen circulation through the column to remove deuterium.

The productivity of the system in the "feed through" mode is 500 L/day. In the mode of circulation through the CHUPS system it comes to 150 L/day. The mode of Rayleigh depletion is considered to be inefficient because of small initial amount of hydrogen in the column.

The method of measurement of low deuterium content in hydrogen (1 ppm and less) is suggested. It is based on deuterium enrichment by a factor of 40 (and even more) in the reboiler.

This work is also of great importance for Detritiation Plant of PIK reactor as in accordance with a new developing design of the plant the cryogenic column with close parameters is needed. A good packing was developed and tested, successful experience was gained.

References

1. A. Vasilyev, B. Bezymyannykh, V. Ganzha, P. Kravtsov, G. Shapkin, V. Trofimov and M. Vznuzdaev, talk at *the National Hydrogen Association Annual Hydrogen Conference 2005*, Washington, USA.
2. I.A. Alekseev *et al.*, Preprint PNPI-2702, Gatchina, 2006. 26 p.
3. I.A. Alekseev, I.A. Baranov, S.D. Bondarenko, S.N. Chernoby, O.A. Fedorchenko, G.A. Sukhorukova, V.D. Trenin and V.V. Uborski, *Fusion Technology* **28**, 1579 (1995).

ARCHITECTURE OF SMALL COMPUTING CLUSTERS IN HIGH ENERGY PHYSICS

A.N. Lodkin, A.A. Oreshkin, A.Y. Shevel, T.S. Serebrova

1. Introduction

In last years we see that large **High Energy Physics (HEP)** collaborations use high performance computing clusters. Most of the clusters are integrated into World Grid infrastructure. At the same time, we observe that small clusters do continue to play their own role in the computing life. We mean *small* for the cluster up to about 50 machines or so. It is quite obvious that such small cluster is supposed to serve relatively small physics group, may be about 10 physicists. A good time is now to discuss a realistic scenario how physics data might be processed and analyzed and what computing architecture might be used by small physicist's teams.

Contemporary architecture of small computing clusters in **HEP** for physics analysis is based on the commodity hardware. In most of cases it is a Personal Computer (**PC**) based on Intel compliant microprocessors. Scientific Linux is the main operating system. It is better when the computing cluster is a member of a Grid Virtual Organization(s). Here we plan to discuss several aspects of computing cluster design and implementation and how small clusters are related to large computing installations.

2. Large clusters

Several important clusters of Tier 1 & Tier 2 are mentioned in Table 1 (N/A means that the information is *Not Available*). Each cluster of level Tier 1 has tens of **FTEs** in the staff. Most of such clusters have 10 Gbit or more external connectivity. Most of Tier 2 clusters have external channels in between 1 Gbit and 10 Gbit. There are expectations that in 2010 many Tier 1 clusters will have 1 Tbit channels. Each cluster uses a batch system – usually one or two from the range: **LSF, Condor, Torque/PBS, SGE**.

Table

Number of hosts and data volumes on several computing clusters in HEP (info from HEPiX October 2006)

Laboratory	Facility type	Number of hosts in clusters	Data volume on disks	Data volume in Mass Storage
BNL	Tier 1	~2.0 K	~400 TB	~4.0 PB
Canadian GridX	Tier 1	~1.2 K	~100 TB	~0.4 PB
FNAL Grid Computing Center	Tier 1	~3.0 K	~700 TB	~4.0 PB
GridPP/RAL	Tier 1	~2.9 K	~168 TB	N/A
NIKHEF	Tier 1	~0.3 K	~ 70 TB	N/A
SLAC	Tier 2	~1.7 K	~755 TB	N/A
GRIF(France)	Tier 2	~1.2 K	~700 TB	N/A
INFN	Tier 1	~1.3 K	~600 TB	N/A

Of course clusters are included into one or several Grid Virtual Organizations (**VO**). One of the consequences is that the bulk data moving over World Area Network (**WAN**) must be planned and performed with Grid tools. Each VO has its own rules on the data moving. There is special person (manager) responsible for data moving process. At the same time if the bulk data moving is started it is difficult to predict when the operation would be accomplished. Due to this fact in many large clusters the user jobs are planned to be cancelled if the data requested by jobs are not available in local disk space.

Apparently clusters Tier 1 (or even Tier 2) are main source of physics data and main repository for the software of almost any kind. Often it is required to create new data with special selection algorithm from other data before start an analysis. Because resulted data are peculiar or even private the small physicist's team needs to keep the data in own disk space which could be obtained on large cluster for relatively short period of time. In many cases a small computing cluster is best place to keep own data for long time.

When small physicist's team plans to use existing large cluster it important to know not only power of the cluster but the administrative conditions on the cluster [1,2]. For example if any non privileged user can keep just 40 jobs in the run stage (permitted to use 40 CPUs), it does not matter for him that the cluster consists of 10K machines. Of course in Grid architecture someone can easily send jobs to another cluster where the data are, i.e. it possible to use more than one computing cluster. However in most of real situations some data moving and other additional operations are required. Real advantage to use more than one cluster can be gained if specific conditions are taken place [3]. In this discussion it is assumed that clusters are really stable. The stability in general and difficulty to predict future status of the Grid clusters is a hot topic for now. Anyway, there is an expected advantage with using of two computing clusters instead of one.

3. Estimates for accelerating of computing with two clusters

Let us imagine two clusters where we can do some data analysis or data simulation. For example one cluster is in one research institute and another cluster is in another institute or university, the clusters have independent administration. For simplicity we will use terms *local cluster* and *remote cluster*. We consider the *computation* as bunch of simulation (data generation) jobs or data analysis jobs which could be performed on any of two clusters. Usually the bunch of jobs is performing many hours or many days. All jobs are considered as accomplished when the computing itself is ended and the data are moved to final (target) place, for instance to small computing cluster.

Let us introduce several variables:

T – the time for computing task with using one (local) cluster;

τ – the time for computing with two clusters;

t_l – average time for processing of one portion of the data on one (local) cluster;

t_r – average time for processing of one portion of the data on one (remote) cluster;

t_o – the average overhead time which is required to process one portion of the data on remote cluster; we can include in this time anything we need to make computation possible in remote cluster, for example, time to transfer the data to (from) remote cluster;

D – total number of the data portions which have to be processed;

S – the number of data portions which are processed per time unit;

α – acceleration of the computing due to use of additional cluster.

Now we can write for only (local) cluster $S = \frac{1}{t_l}$ and total time for data processing is

$$T = \frac{D}{S} = D \cdot t_l.$$

For two clusters (local and remote) we can write $S = \frac{1}{t_l} + \frac{1}{t_o + t_r}$ and total time for the computing is

$$\tau = \frac{D}{\left(\frac{1}{t_l} + \frac{1}{t_o + t_r} \right)}.$$

It is assumed that the jobs will be sent to remote cluster only when local cluster is fully loaded with our jobs. Now accelerating is

$$\alpha = \frac{T}{\tau} = t_l \cdot \left(\frac{1}{t_l} + \frac{1}{t_o + t_r} \right) = 1 + \frac{t_l}{t_o + t_r}.$$

Above might be rewritten as

$$\alpha = \frac{(t_o/t_r + 1 + t_l/t_r)}{(t_o/t_r + 1)}.$$

From above formula we see that the accelerating is quite sensitive to the overhead time t_o (please see in Fig. 1) Even in case when remote cluster has huge throughput, when value t_r can be considered close to 0, we have the acceleration is limited by t_o .

It is possible to conclude:

- the expected acceleration for the computing with two clusters can be relatively easy estimated;
- the use of two computing clusters instead one cluster does not mean guaranteed decreasing the computation time in all cases, concrete overheads are very important;
- in long term plan (many days or weeks) the probability that the remote cluster is up and running properly is important.

If we plan to keep the data on small cluster apparently it is more effective to analyze the data on the same cluster.

All above reasons do lead to understanding that in a range of cases the use of small computing cluster is very helpful. Let us consider the architecture of such clusters.

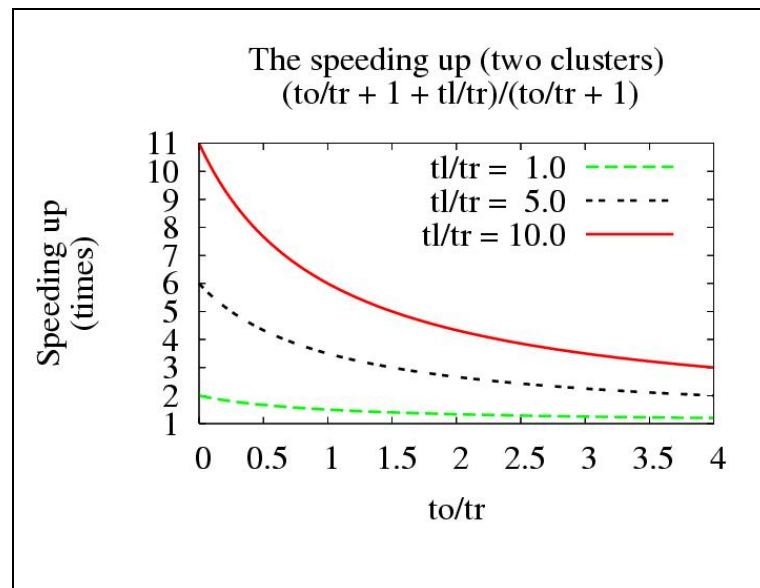


Fig. 1. Computing acceleration with two clusters with different conditions

4. Cluster architecture considerations

Last years CPU (microprocessor) performance is increasing at the rate around 60% per year. At the same time disk read/write speed is increasing about 10% per year. Also disk volume per spindle is increasing at the rate around 60% per year. It means that access to disk space (especially in HEP, due to extremely large volume of the data) is more and more often becomes a bottleneck. There are many reasons to think that such the relations in between mentioned values will be kept at least for several years in the future.

In the light of such facts and facing the need to analyze tremendous volume of the data the methods how to make read/write operations in parallel are most hot topic. One of the methods is to use advanced RAID controllers and advanced cluster file system, for example, Lustre, PVFS, GFS, GPFS, Panasas, StorNext, and the like.

Another very simple method was suggested in the presentation [4]. The approach assumes two opposite configurations and many in between. First is to use one central machine in the cluster where connected all RAIDs. Opposite configuration is to use the disk space on each machine in the cluster as shown in Fig. 2. Here all file systems are mounted by NFS over separate network channel for each file system. More specialized systems like xrootd are addressing the same target: to make I/O operation in parallel. Another important point in small cluster is architectural features which permit to reduce the requirements of local maintenance to the minimum.

5. Remote maintenance for small computing cluster

When new cluster design is under consideration we need to take into account the trends with less available manpower in future years. In other words we have to plan as much as minimum local maintenance activity. To permit remote experts to do their job the cluster must be equipped with appropriate components.

Vital and stable solution may be implemented with using the special hardware. We mean type of devices so called **KVM** switch. **KVM** switch (or just **KVM**) is device which connects all control lines (keyboard, mouse, monitor) from each cluster node. **KVM** has connectors to connect real keyboard, monitor, and mouse. Also **KVM** has ability to connect (logically) real keyboard, mice, monitor to any desired server in the cluster.

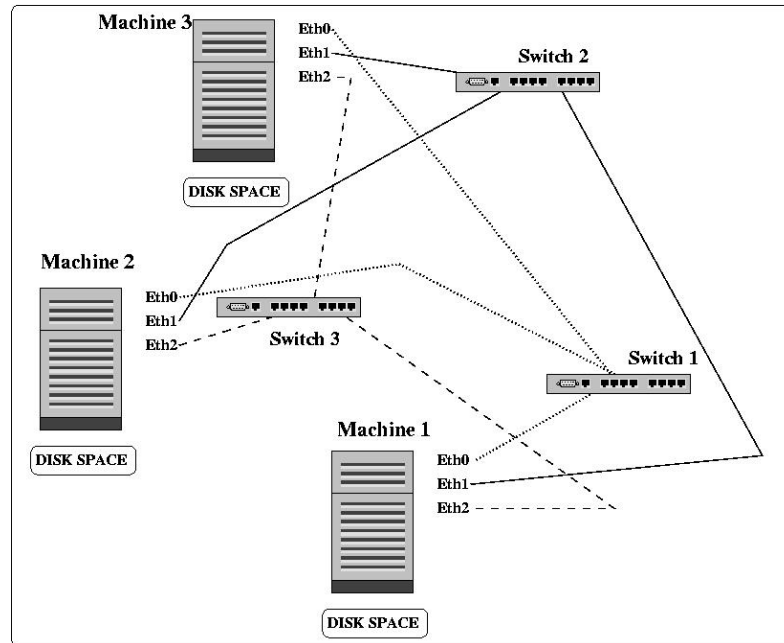


Fig. 2. Cluster scheme where each machine has own disk space

Another device entitled *remote IP console (RIPC)* is used as interface in between **KVM** and Internet. An expert on remote computer can use Web browser (with enabled Java functionality) to make connection to the device **RIPC** with protocol **https** and see the screen on **Java** applet. **Java** applet displays redirected console screen, keyboard, and mouse of the cluster where **RIPC** is attached. In other words the expert is able to use local for him keyboard, mouse as they would be attached to the cluster.

Among other mandatory components of the cluster we can mention **UPS** – to make electricity power more stable – and **PDU** - to have ability to switch electrical power **on** and **off** for specified machine in the cluster. An air conditioning is also in range of requirements.

The basic requirements were enumerated. Now other details concerning the software have to be discussed.

6. Technological cluster software and middleware

A range of technological services are seemed very important in contest of easier maintenance procedures. Usually it is very important to have reserve copy of critical data - backup service. Much better is to have reserve copy on the tape cartridges. The tape drive might be used for reserve copy for the physics data as well. Personal subsets of physics data copied on the tape cartridge are often great advantage for physicist.

All cluster users must be in cluster user mailing list. This list is to be used for the information about the changes on the cluster. Such the mailing list may be implemented in several places. One of the useful ways to keep mailing list for small physics team is site <http://groups.google.com/>.

Cluster administrative system is aimed to deploy, configure and support cluster (to keep all system parameters in consistent state) and is in active use on many clusters. Good examples of such the systems are **OSCAR**, **ROCKS**, and the like.

Batch processing on the cluster is usually performed with one of several batch systems: **Torque/PBS**, **Condor**, **Sun Grid Engine**, **LSF**. Fortunately batch systems in use on large clusters are pretty same as for small clusters. One of the specialized batch tools is **PROOF**. It is the system for users who does like to be all the time inside **ROOT** environment. Part of physicists do use **PROOF** for data analysis.

Monitoring systems are almost same as for large clusters, for instance **Ganglia** and **Nagios**.

Grid middleware is another large software component which is required if the cluster is included into one or more Grid Virtual Organizations. The part of middleware components are the same for all VOs (basic **Globus** toolkit and the like.). A good fraction of middleware is developed by concrete VO and it is not supposed to be used outside the VO.

7. Application software and related databases

Application software dedicated for concrete physics is large fraction of all software tools on the computing cluster. This software has as a rule many versions (may be several tens). Usually people keep all versions on the cluster. Such the software is kept on leading clusters (Tier 1) in **AFS** tree. In general it is possible to use it over **AFS**, however real experience shows that much better to keep local copy of the software. It is performed with one or another set of mirroring mechanisms for example once a week or so. It is quite safe for small physics team especially if some problems are appeared on leading clusters (**AFS** server is down, application software tree becomes unusable). Almost the same we can repeat about such databases as geometry/calibrations database, *etc.*

8. Small cluster support over years

The cluster is running, data analysis is in progress but time is going on and new versions of software (application, system, middleware) are appeared. Quite often you have to do upgrade the software to guarantee that you have same common software packages as your colleagues do. That means somebody has to be careful about consistency of the software.

Furthermore with the time (one, two, three years) you might (very probable) discover that some machines in the cluster are broken or out of date and do not meet newest requirements. Common rule is to remove from the cluster any machine which gives any kind of problems. In average if we like to keep the computing cluster abilities on top – we have to plan to change about 1/3 machines in the cluster every year. It means to remove old machine from cluster and add new machine instead. The machines retired from the cluster might be used as personal machines for students, physicists, *etc.* The reach source of useful information about computing clusters is available at the site <http://hepd.pnpi.spb.ru/ClusterGate.RU>.

9. Conclusion

Obviously it is not possible to use small computing clusters *instead of* large clusters of Tier 1 or 2. It is very useful as a complement to large computing installations; also they make use of large computing facility more optimal. Taking into account that prices for disks and CPUs are going down, it is clear that about 20–50 machines with 50–100 TB of disk space are foreseeable for small physicist's team for most of analysis needs.

References

1. B. Jacak, R. Lacey, S. Mioduszewski, D. Morrison, A. Shevel and I. Sourikova, talk presented at *the Conference on Computing in High Energy Physics CHEP2003* (La Jolla, USA, 24 – 28 March 2003), presentation TUCT009 in <http://www.slac.stanford.edu/econf/C0303241/proceedings.html>
2. A. Shevel, B. Jacak, R. Lacey *et al.*, in *the Proceedings of the Conference on Computing in High Energy Physics CHEP2004* (Interlaken, Switzerland, 24 September – 1 October 2004), Geneva, 2005. p. 974.
3. A. Shevel and R. Lacey, talk presented at *the Globus World Conference* (Boston, USA, 7 – 11 February 2005).
4. A. Shevel and R. Lacey, poster presentation at *the Conference on Computing in High Energy Physics CHEP2006* (Mumbai, India, 13 – 17 February 2006).

THIRD GENERATION COORDINATE READOUT SYSTEM – CROS-3

N.F. Bondar, V.L. Golovtsov, A.G. Golyash, E.A. Lobachev, L.N. Uvarov, S.L. Uvarov, V.I. Yatsura

The design and development of the fast and cost effective readout electronics for the tracking detectors is the scope of interest of the modern experiments such as LAND (performed at GSI, Darmstadt), FAMILON, *etc.* The setup of the experiments includes fine pitch MultiWire Proportional Chambers (MWPC) and wire Drift Chambers (DC) with hexagonal cell structure. Variety of modern integrated circuits together with advanced PCB technology allowed to develop the best quality CROS-3 devices and meet the requirements of the experiments.

Block diagram of the CROS-3 system in Fig. 1 includes:

- 96-channel MWPC Digitizers (CDR96);
- 16-channel DC Digitizers (AD16);
- 16-channel Concentrators (CCB16);
- System Buffer (CSB).

Analog part of the CDR96 is based on a CMP_G ASIC performing wire signal amplification and shaping as well as pulse discrimination with peaking time of 30 ns, minimum threshold of 7 fC, double pulse resolution of 80 ns, and power dissipation about 35 mW/channel.

Analog part of the 16-channel DC Digitizer is based on a ASD-Q ASIC [1] with similar functionality and the following characteristics: peaking time of 7 ns, operational threshold at 2–3 fC, double pulse resolution of 20 ns, and power dissipation about 35 mW/channel.

Digital part of either Digitizer is implemented in a Xilinx Spartan-3 FPGA that performs both digitization and readout tasks. Input signals are digitized and delayed to compensate for the trigger latency. Upon receiving a trigger signal, a temporary buffer stores programmable number of time bins. Then the encoder looks for the signal leading edge and encodes both its wire number and its relative time slice number. The delay range compensates trigger latency of up to 2.5 μ s in 10 ns steps. The finest time bin resolution is 2.5 ns for the AD16 and 10 ns for the CDR96 cards. Maximim number of time slices is 255 for AD16 and 64 for CDR96. Readout is performed over a STP CAT5 cable at a 100 Mb/sec bit rate.

The CCB16 collects data from up to 16 Digitizers into temporary buffers, which are read out to the CSB via an optical fibre at a 2.0 Gb/sec bit rate.

The CSB is implemented as a universal PCI card.

Figure 2 shows system components mounted directly on the chamber.

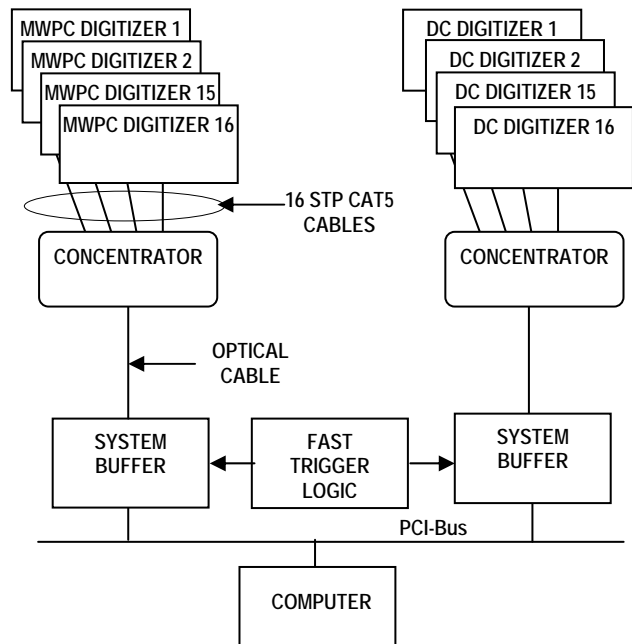


Fig. 1. CROS-3 block diagram



Fig. 2. CROS-3 Digitizers and Concentrator are on-chamber mounted system components

References

1. W. Bokhari *et al.*, CDF/DOC/TRACKING/CDFR/4515 December 1999.

MULTI-CHANNEL HIGH VOLTAGE DISTRIBUTION AND MONITORING SYSTEM FOR LHCb MUON CHAMBERS

S.V. Bondarev, N.B. Isaev, V.I. Lazarev, A.V. Mylnikova, L.O. Sergeev, S.S. Volkov

A multi-channel High Voltage Distribution and Monitoring System (HVDM) was designed and constructed for muon chambers produced at PNPI for the LHCb Muon detector. Two options of the system are developed to be used for the chambers. The first one (HVDM_16) allows linear regulation in each distributed channel in a range of 0-3000 V. The second (HVDM_LHCb) one, being radiation hard, allows linear regulation in each distributed channel only within 1000 V.

HVDM block diagram in Fig.1 includes:

1. 36-channel radiation hard Remote Distributors, performing high voltage fan-out from 1 input to 36 outputs, output voltage regulation within 1000 V in 1 V steps, output voltage measurement with 1 V resolution, and output current measurement with 10 nA resolution in $I < 1 \mu\text{A}$, and 100 nA resolution in $I > 1 \mu\text{A}$ range (100 μA max current) for each output. The radiation hardness value is up to 4 krad at 2×10^{12} neutron/cm².

2. 8-channel Master Distributor, performing high voltage fan-out from 1 input to 8 outputs, voltage regulation from 0 to 3000 V in 1 V steps, output voltage measurement with 1 V resolution, and output current measurement with better than 100 nA resolution (1.5 mA max output current) for each output.

3. 16-channel Distributors, performing high voltage fan-out from 1 input to 16 outputs, output voltage regulation from 0 to 3000 V in 1 V steps, output voltage measurement with 1 V resolution, and output current measurement with 10 nA resolution in $I < 1 \mu\text{A}$ and 100 nA resolution in $I > 1 \mu\text{A}$ range (100 μA max current) for each output.

4. Primary High Voltage Power Supply, which can be any industrial rack mounted unit, like Matsusada High Voltage Power Supply, model AV-3*50, whose output regulates in a range from 0 to 3000 V.

5. System Interface/Buffer, providing control and monitoring of the Master and Distributors via the Control/Readout Line. It is implemented as a universal PCI card, compliant to PCI 2.2 specification. Card's buffer memory keeps both voltage setting and actual voltage and current values for each channel.

The HVDM module dimensions comply with the Eurocard (IEC 297 and IEEE 1101) form factor and are 240 mm × 6U for Master and Distributor, and 540 mm × 6U for Remote Distributor. The HVDM design follows that of the high voltage system developed for the CMS EMU CSC in cooperation with the University of Florida (USA).

Figure 2 illustrates design of 36-channel Remote Distributor with each channel served by a plug-in card.

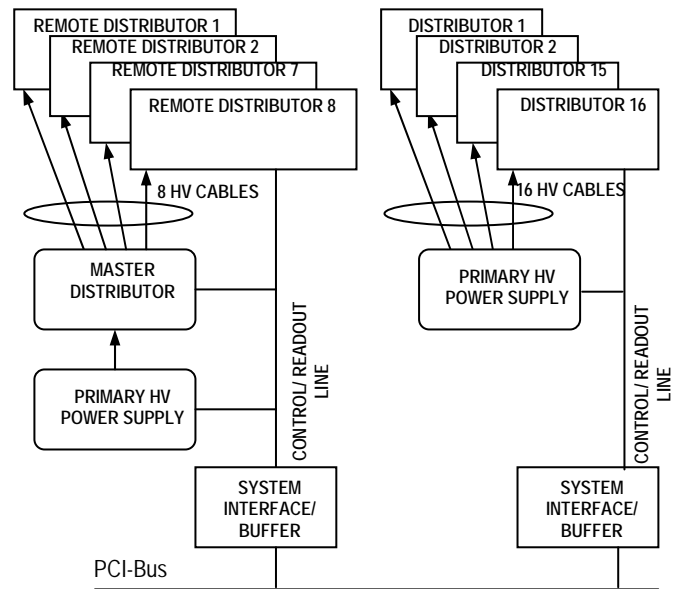


Fig. 1. Block diagram of the HVDM system

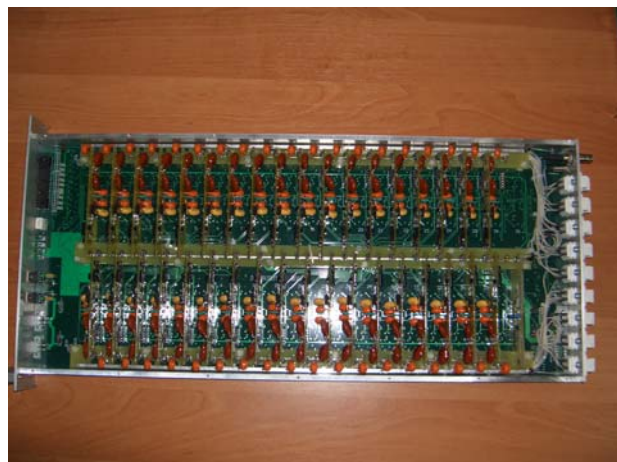


Fig. 2. 36-channel Remote Distributor

TRACK FINDING PROCESSOR FOR THE CMS ENDCAP LEVEL 1 MUON TRIGGER

V.L. Golovtsov, L.N. Uvarov, D. Acosta¹⁾, D. Holmes¹⁾, K. Kotov¹⁾, A. Madorsky¹⁾, S.M. Wang¹⁾

¹⁾ *University of Florida, USA*

A fast three-dimensional Track-Finding Processor was designed for the Level-1 trigger of the CMS endcap muon system. The Track-Finding Processor is implemented as 12 Sector Processors (SP), each of which identifies up to three best muons in a 60-degree azimuthal sector [1]. The purpose of the Track-Finding Processor is to link trigger primitives (track segments) from individual muon stations (four endcap stations ME1-4 and two barrel overlap regions MB1-2) into complete tracks, measure the transverse momentum P_t from the sagitta induced by the magnetic bending, and report the number and quality of tracks to the Level-1 Muon Trigger. The maximum number of track segments collected by one SP is 15 per 25 ns bunch crossing.

Block diagram of the SP logic in Fig. 1 includes:

1. Sector Receiver (SR), which receives local charge track information for 15 muons via optical links. This information is then synchronized and reformatted within the SR (*via* look-up tables) into angular variables for the muons: azimuthal angle φ , local bent angle in φ (φ_b) and pseudo-rapidity η .

2. Five Extrapolation Units (EU), where all possible pairwise combinations of track segments are tested for consistency with a single track. Each EU takes spatial information from two track segments in different stations and tests if those two segments are compatible with a muon originating from the nominal collision vertex with a curvature consistent with magnetic bending in that region.

3. Three Track Assembly Units (TAU) to examine all outputs of the EUs and determine if any two track segment pairs belong to the same muon. If so, those segment pairs are combined and rank is assigned based on the muon stations involved. For this SP design, stations ME2 and ME3 are the key stations. A valid trigger in the end-cup region must have a hit in one of these two stations. The output of the EUs can be separated into three streams: two for patterns keying off ME2 and ME3 in the end-cup region, and one for pattern keying off ME2 in the end-cup or/and barrel overlap region. Up to three tracks may be found per data stream, nine tracks in total for all three streams.

4. Final Selection Unit, which selects the best three muon candidates. It also features cancellation logic for redundant tracks.

5. Assignment Unit, which measures the track parameters of the best three selected muon candidates.

Finally, the best three muon candidates are sent to the Muon Sorter that in turn selects the best four candidates within all tracks of the 12 Sector Processors and sends them to the Global L1 Muon Trigger.

Figure 2 shows a fully assembled Track-Finding Crate with 12 Sector Processors and Muon Sorter.

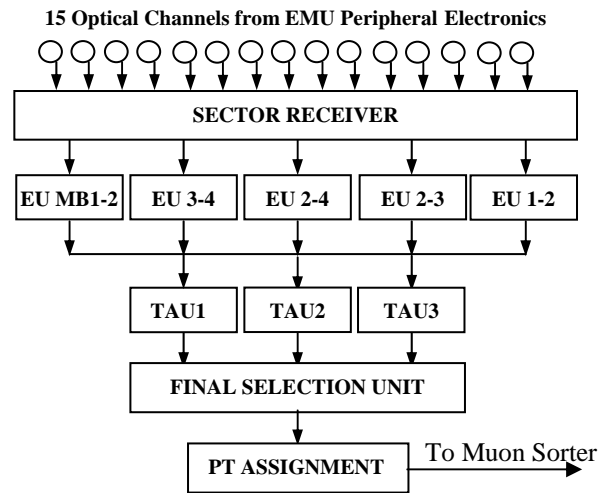


Fig. 1. Sector Processor block diagram

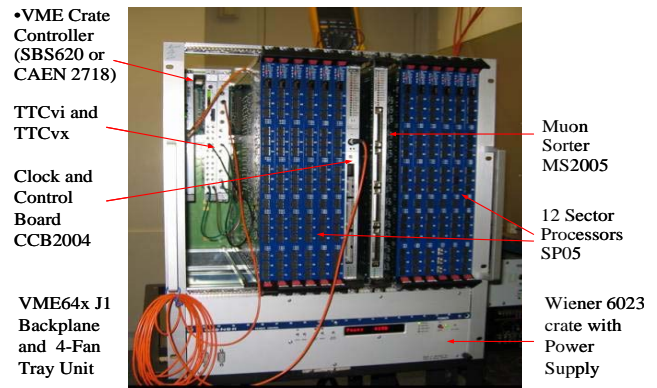


Fig. 2. Track-Finding Crate

References

1. D. Acosta *et al.*, Nucl. Instr. Meth. A **496**, 64 (2003).

CONTENTS

PREFACE	3
STATUS OF ACCELERATOR FACILITIES AT PNPI	
PNPI SYNCHROCYCLOTRON IN 2002–2006 N.K. Abrossimov, G.F. Mikheev, G.A. Riabov, and accelerator staff	6
DESIGN AND CONSTRUCTION OF 80 MeV H ⁻ -ION ISOCHRONOUS CYCLOTRON WITH BEAM CURRENT OF 100 μ A N.K. Abrossimov, S.A. Artamonov, V.P. Gres, V.A. Eliseev, E.M. Ivanov, Yu.T. Mironov, G.F. Mikheev, A.S. Pokrovsky, G.A. Riabov, V.A. Smolin, I.A. Petrov, B.B. Tokarev	15
STATUS OF LHC EXPERIMENTS	
PNPI PARTICIPATION IN LHC EXPERIMENTS	24
CMS EXPERIMENT	
A.A. Vorobyov, D.M. Seliverstov, Yu.M. Ivanov, V.L. Golovtsov, V.S. Kozlov, N.F. Bondar, A.S. Denisov, A.G. Golyash, Yu.I. Gusev, V.I. Lazarev, V.D. Lebedev, P.M. Levchenko, G.V. Makarenkov, E.M. Orischin, A.A. Petrunin, A.I. Shchetkovsky, L.A. Schipunov, V.A. Sknar, V.V. Sulimov, V.I. Tarakanov, <u>I.I. Tkatch</u> , L.N. Uvarov, S.A. Vavilov, G.N. Velitchko, S.S. Volkov, An.A. Vorobyov, V.I. Yatsura, G.F. Zhmakin	26
TRANSITION RADIATION TRACKER FOR ATLAS PROJECT	
O.L. Fedin, E.G. Danilevich A.G. Khristachev, L.G. Kudin, S.N. Kovalenko, V.P. Maleev, A.V. Nadtochy, S.K. Patrichev, Yu.F. Ryabov, D.M. Seliverstov, V.A. Schegelsky, E.M. Spiridenkov, A.Yu. Zalite	35
LHCb EXPERIMENT	
A.A. Vorobyov, B.V. Bochyn, N.F. Bondar, O.E. Fedorov, V.L. Golovtsov, G.A. Gorodnitsky, S.A. Guets, A.P. Kaschuk, V.S. Kozlov, Z.G. Kudryashova, V.I. Lazarev, V.D. Lebedev, O.E. Maev, G.V. Makarenkov, P.V. Neustroev, N.R. Sagidova, E.M. Spiridenkov, N.M. Stepanova, V.I. Tarakanov, A.Yu. Tsaregorodtsev, S.S. Volkov, An.A. Vorobyov, A.A. Zhdanov	42
PNPI IN ALICE	
V.M. Samsonov, V.A. Evseev, V.V. Ivanov, A.V. Khanzadeev, E.L. Kryshen, N.M. Miftakhov, V.N. Nikulin, V.V. Polyakov, E.V. Roschin, <u>V.I. Ryazanov</u> , O.P. Tarasenkova, M.B. Zhalov	50
STUDY OF CHANNELING AND VOLUME REFLECTION EFFECTS IN BENT CRYSTALS	
Yu.M. Ivanov, N.F. Bondar, Yu.A. Gavrikov, A.S. Denisov, A.V. Zhelamkov, V.G. Ivochkin, S.V. Kosyanenko, L.P. Lapina, A.A. Petrunin, V.V. Skorobogatov, V.M. Suvorov, A.I. Shchetkovsky ...	58
ELEMENTARY PARTICLES PHYSICS	
PRECISION MEASUREMENT OF THE RATE OF MUON CAPTURE IN HYDROGEN GAS AND DETERMINATION OF THE PROTON'S PSEUDOSCALAR COUPLING g_P	
V.A. Andreev, V.A. Ganzha, P.A. Kravtsov, A.G. Krivshich, E.M. Maev, O.E. Maev, G.E. Petrov, G.N. Schapkin, G.G. Semenchuk, M.A. Soroka, A.A. Vasilyev, A.A. Vorobyov, M.E. Vznuzdaev	68
NEW RESULTS FROM SELEX	
G.D. Alkhazov, V.L. Golovtsov, V.T. Kim, A.G. Krivshich, P.V. Neustroev, L.N. Uvarov, A.A. Vorobyov	76

RECENT PHYSICS RESULTS FROM THE D0 EXPERIMENT G.D. Alkhazov, V.T. Kim, A.A. Lobodenko, P.V. Neustroev, G.Z. Obrant, Yu.A. Scheglov, L.N. Uvarov, S.L. Uvarov	84
STUDY OF LIGHT VECTOR MESONS AT RHIC BY PHENIX V.V. Baublis, D.A. Ivanischev, A.V. Khanzadeev, B.G. Komkov, V.G. Ryabov, Yu.G. Ryabov, V.M. Samsonov, E.M. Vznuzdaev, M.B. Zhalov	91
HERMES EXPERIMENT AT DESY: SELECTED ANALYSIS RESULTS S.L. Belostotski, G.E. Gavrilov, A.A. Izotov, AA. Jgoun, A.Yu. Kisselev, P.V. Kravchenko, S.I. Manaenkov, O.V. Miklukho, Yu.G. Naryshkin, D.O. Veretennikov, V.V. Vikhrov.....	97
RESULTS OF ELECTROWEEK INTERACTION FROM LEP-II EXPERIMENT AT CERN V.A. Schegelsky	107
QUARCONIUM PHOTOPRODUCTION IN ULTRAPERIPHERAL ION COLLISIONS WITH THE ALICE DETECTOR AT LHC V.N. Nikulin, V.M. Samsonov, M.B. Zhalov	113
EXPERIMENTS OF CRYSTAL BALL COLLABORATION AT BNL V.V. Abaev, V.S. Bekrenev, N.G. Kozlenko, S.P. Kruglov, A.A. Kulbardis, I.V. Lopatin, A.B. Starostin.....	118
STUDY OF PHOTOPRODUCTION OF NEUTRAL MESONS USING THE CRYSTAL BARREL AT ELSA D.E. Bayadilov, Yu.A. Beloglazov, A.B. Gridnev, I.V. Lopatin, D.V. Novinsky, A.K. Radkov, V.V. Sumachev	125
STUDY OF BINARY π^-p REACTIONS WITH NEUTRAL PARTICLES IN THE FINAL STATE AT THE PION CHANNEL OF THE PNPI SYNCHROCYCLOTRON D.E. Bayadilov, Yu.A. Beloglazov, N.G. Kozlenko, S.P. Kruglov, I.V. Lopatin, D.V. Novinsky, A.K. Radkov, V.V. Sumachev	133
MEASUREMENT OF THE SPIN ROTATION PARAMETERS A AND R IN πp ELASTIC SCATTERING AT THE PION CHANNEL OF THE ITEP ACCELERATOR A.I. Kovalev, S.P. Kruglov, D.V. Novinsky, V.A. Shchedrov, V.V. Sumachev, V.Yu. Trautman	141
TWO-PION PRODUCTION IN ωp SCATTERING AT 1 GeV/NUCLEON IN THE ENERGY REGION OF THE $P_{11}(1440)$ RESONANCE EXCITATION G.D. Alkhazov, <u>A.V. Kravtsov</u> , A.N. Prokofiev	147
STRANGENESS PRODUCTION IN HADRON-INDUCED REACTIONS S.G. Barsov, A.A. Dzyuba, V.P. Koptev, S.M. Mikirtychyants, M.E. Nekipelov, Yu.V. Valdau	156
INVESTIGATION OF THE $pp \rightarrow pp\pi^0$ REACTION AT TWO ENERGIES NEAR 1 GeV V.V. Sarantsev, K.N. Ermakov, V.I. Medvedev, O.V. Rogachevsky, S.G. Sherman	162
EXTRACTION OF THE $\pi^-n \rightarrow \pi^- \pi^- p$ CROSS SECTION FROM THE MEASUREMENT OF THE $\pi^- d \rightarrow \pi^- \pi^- pp$ REACTION AT ENERGY 430 MeV S.G. Sherman, K.N. Ermakov, V.I. Medvedev, O.V. Rogachevsky, V.V. Sarantsev	169

NUCLEAR AND ATOMIC PHYSICS

EXPERIMENTAL STUDY OF THE NUCLEAR SPATIAL STRUCTURE OF NEUTRON-RICH He AND Li ISOTOPES G.D. Alkhazov, A.V. Dobrovolsky, A.V. Khanzadeev, G.A. Korolev, A.A. Lobodenko, D.M. Seliverstov, A.A. Vorobyov	176
INVESTIGATION OF NUCLEAR MEDIUM EFFECT ON CHARACTERISTICS OF PROTON-PROTON SCATTERING AT 1 GeV O.V. Miklukho, S.L. Belostotski, K. Hatanaka, A.Yu. Kisselev, T. Noro, H. Sakaguchi	184
STUDY OF ENERGY DEPENDENCE OF PROTON-INDUCED FISSION CROSS SECTIONS FOR HEAVY NUCLEI IN THE ENERGY RANGE 200–1000 MeV L.A. Vaishnene, V.G. Vovchenko, Yu.A. Gavrikov, <u>A.A. Kotov</u> , V.V. Polyakov, M.G. Tverskoy, O.Ya. Fedorov, Yu.A. Chestnov.....	192
MECHANISMS OF NUCLEAR DISINTEGRATIONS INDUCED BY RELATIVISTIC PROJECTILES B.L. Gorshkov, <u>A.V. Kravtsov</u> , V.R. Reznik, G.E. Solyakin	200
MASS DEPENDENCE OF NUCLEAR ISOTOPE TEMPERATURE IN LOW ENERGY FISSION M.N. Andronenko, L.N. Andronenko, W. Neubert	208
LASER SPECTROSCOPIC STUDIES OF NEUTRON-DEFICIENT EUROPIUM AND GADOLINIUM ISOTOPES A.E. Barzakh, D.V. Fedorov, A.M. Ionan, V.S. Ivanov, F.V. Moroz, K.A. Mezilev, S.Yu. Orlov, V.N. Panteleev, Yu.M. Volkov	216
NUCLIDES OF ASTROPHYSICS INTEREST WITH MASS NUMBERS CLOSE TO $A \sim 80$ L.Kh. Batist, S.A. Eliseev, Yu.N. Novikov, A.V. Popov, D.M. Seliverstov, G.K. Vorobjev	222
EXPERIMENTAL ESTIMATION OF THE ^8Be YIELD IN THE FRAGMENTATION OF ^{10}B NUCLEI IN PHOTOEMULSION F.G. Lepekhin	230
μSR -INVESTIGATIONS AT PNPI S.G. Barsov, S.I. Vorobyev, V.P. Koptev, E.N. Komarov, S.A. Kotov, S.M. Mikirtychyants, G.V. Shcherbakov	233
NEW PROJECTS	
PNPI PARTICIPATION IN FAIR PROJECTS	242
PROJECT OF NEW UNIVERSAL LASER COMPLEX OF IRIS FACILITY FOR ATOMIC AND NUCLEAR INVESTIGATIONS V.N. Panteleev, A.E. Barzakh, D.V. Fedorov, V.S. Ivanov	257
PROJECT “EPECUR”: SEARCH FOR EXOTIC BARYONS IN REACTIONS $\pi^- p \rightarrow \pi^- p$ AND $\pi^- p \rightarrow K\Lambda$ AT THE MESON CHANNEL OF THE ITEP ACCELERATOR A.I. Kovalev, N.G. Kozlenko, V.S. Kozlov, A.G. Krivshich, D.V. Novinsky, V.V. Sumachev, V.Yu. Trautman, E.A. Filimonov	264
EXPERIMENT “FAMILON”: SEARCH FOR MUON NEUTRINOLESS DECAY V.A. Gordeev, V.S. Demidov, V.N. Duginov, Yu.V. Elkin	272

METODICAL AND APPLIED RESEARCHES

STEREOTAXIC 1000 MeV PROTON THERAPY AT PNPI SYNCHROCYCLOTRON N.K. Abrossimov, Yu.A. Gavrikov, V.Ya. Gersenstein, E.M. Ivanov, N.N. Jalinitch, D.L. Karlin, V.I. Lasarev, V.V. Lysenko, Yu.A. Malov, T.V. Pushkareva, G.A. Riabov, D.M. Seliverstov, R.A. Shalek, V.M. Vinogradov, A.A. Vorobyev, O.M. Zhidkova, M.V. Zhidkov	280
DEVELOPMENT AND ON-LINE TESTS OF DIFFERENT TARGET-ION SOURCE UNITS FOR PRODUCTION OF NUCLIDES FAR FROM STABILITY V.N. Panteleev, A.E. Barzakh, D.V. Fedorov, A.M. Ionan, V.S. Ivanov, K.A. Mezilev, P.L. Molkanov, F.V. Moroz, S.Yu. Orlov, Yu.M. Volkov	288
INVESTIGATION OF BORONIZATION IN GLOBUS-M TOKAMAK AND GAS-FILLED DETECTORS USING THE ELECTROSTATIC ACCELERATOR BEAMS V.M. Lebedev, A.G. Krivshich, V.A. Smolin, B.B. Tokarev, E.I. Terukov, V.K. Gusev	296
COLLINEARITY LIMIT FOR THE MOVEMENT OF COMPLEMENTARY FRAGMENTS FROM THE SPONTANEOUS FISSION OF ^{252}Cf NUCLEI DETERMINED BY IMPLEMENTATION OF THE $(2E, 2V)$ -MEASUREMENT METHOD M.N. Andronenko, B.L. Gorshkov, <u>A.V. Kravtsov</u> , I.A. Petrov, V.R. Reznik, G.E. Solyakin	303
RADIATION HARD PHOTODETECTORS BASED ON FINE-MESH PHOTOTUBES FOR CALORIMETRY IN VERY FORWARD RAPIDITY REGION Yu.I. Gusev, V.N. Lukianov, G.A. Mamaeva, D.M. Seliverstov, L.P. Shusterman	308
SYSTEM FOR DEEP PURIFICATION OF HYDROGEN IN MuCap EXPERIMENT V.A. Ganzha, P.A. Kravtsov, V.A. Trofimov, G.N. Shapkin, A.A. Vasilyev, M.E. Vznuzdaev	313
HYDROGEN DISTILLATION AT THE DEUTERIUM REMOVAL UNIT OF MuCap EXPERIMENT I.A. Alekseev, E.A. Arkhipov, S.D. Bondarenko, O.A. Fedorchenko, V.A. Ganzha, P.A. Kravtsov, V.A. Trofimov, A.A. Vasilyev, T.V. Vasyanina, M.E. Vznuzdaev	321
ARCHITECTURE OF SMALL COMPUTING CLUSTERS IN HIGH ENERGY PHYSICS A.N. Lodkin, A.A. Oreshkin, A.Y. Shevel, T.S. Serebrova	329
THIRD GENERATION COORDINATE READOUT SYSTEM – CROS-3 N.F. Bondar, V.L. Golovtsov, A.G. Golyash, E.A. Lobachev, L.N. Uvarov, S.L. Uvarov, V.I. Yatsura	334
MULTI-CHANNEL HIGH VOLTAGE DISTRIBUTION AND MONITORING SYSTEM FOR LHCb MUON CHAMBERS S.V. Bondarev, N.B. Isaev, V.I. Lazarev, A.V. Mylnikova, L.O. Sergeev, S.S. Volkov	335
TRACK FINDING PROCESSOR FOR THE CMS ENDCAP LEVEL 1 MUON TRIGGER V.L. Golovtsov, L.N. Uvarov, D. Acosta, D. Holmes, K. Kotov, A. Madorsky, S.M. Wang	336
CONTENTS	337